



# Università degli Studi di Salerno

DIPARTIMENTO DI FISICA "E. R. CAIANIELLO"  
DOCTOR OF PHILOSOPHY IN PHYSICS

XIV CICLO, II SERIE (2013-2015)

Superconductivity in S/F hybrids:  
a Scanning Probe Microscopy study of orbital interaction

**Cinzia Di Giorgio**

Tutors

Prof. Fabrizio Bobba

*Università degli Studi di Salerno*

Prof. Maria Iavarone

*Temple University*

Coordinator

Prof. Canio Noce

*Università degli Studi di Salerno*

# Contents

<b>Introduction</b>	<b>1</b>
<b>Bibliography</b>	<b>4</b>
<b>1 S/F hybrids</b>	<b>7</b>
1.1 Introduction . . . . .	7
1.2 Superconductor/Ferromagnet hybrids . . . . .	9
1.3 Orbital Coupling . . . . .	10
1.3.1 Magnetostatic Interaction . . . . .	12
1.3.2 Planar S/F hybrids with ferromagnetic stripe domains . . . . .	13
1.4 Exchange Coupling . . . . .	15
1.4.1 Proximity effect in S/F hybrids . . . . .	18
<b>Bibliography</b>	<b>20</b>
<b>2 Scanning Probe Microscopy</b>	<b>29</b>
2.1 Introduction . . . . .	29
2.2 Scanning Probe Microscopy . . . . .	30
2.2.1 Magnetic Force Microscopy . . . . .	32
2.2.2 Scanning Tunneling Microscopy and Spectroscopy . . . . .	36
2.3 Cryogenic Scanning Microscopes . . . . .	39
2.3.1 Cryogenic SFM - Omicron . . . . .	40
2.3.2 Cryogenic STM/STS - Unisoku . . . . .	44
<b>Bibliography</b>	<b>47</b>

<b>3</b>	<b>Vortex nucleation and dynamics in Nb/Py hybrids</b>	<b>51</b>
3.1	Introduction . . . . .	51
3.2	Sample Fabrication and Preliminary Characterizations . . . . .	53
3.3	Superconducting Vortex Nucleation . . . . .	57
3.4	Superconducting Vortex Dynamics . . . . .	61
3.5	Magnetization Measurements . . . . .	62
3.6	Conclusions . . . . .	64
	<b>Bibliography</b>	<b>67</b>
<b>4</b>	<b>Vortex confinement in S/F hybrids</b>	<b>69</b>
4.1	Introduction . . . . .	69
4.2	Sample Fabrication and Preliminary Characterization . . . . .	70
4.3	MFM study of vortex confinement in Nb/Py . . . . .	75
4.4	STM/STS study of vortex confinement in Pb/[Co/Pd] . . . . .	79
4.5	Conclusions . . . . .	83
	<b>Bibliography</b>	<b>85</b>
<b>5</b>	<b>Quantitative MFM</b>	<b>89</b>
5.1	Introduction . . . . .	89
5.2	Tip Characterization . . . . .	93
5.3	Measure of $1\mu\text{m}$ Py out-of-plane magnetization . . . . .	96
5.4	Conclusions . . . . .	97
	<b>Bibliography</b>	<b>99</b>
	<b>Conclusions</b>	<b>101</b>
	<b>Publications</b>	<b>103</b>
	<b>Acknowledgments</b>	<b>105</b>

# Introduction

In the framework of the Ginzburg-Landau (G-L) theory [1], conventional superconductors are classified in *type I* and *type II*, based on the value the G-L parameter  $k = \frac{\xi}{\lambda}$ ,  $k > \frac{1}{\sqrt{2}}$  and  $k < \frac{1}{\sqrt{2}}$  respectively. The *coherence length*  $\xi$  defines the length scale on which the local density of the superconducting Cooper pairs varies whereas the *penetration depth*  $\lambda$  is the distance at which the external magnetic field is exponentially screened from the interior of the superconducting sample (*Meissner effect*). In type II superconductors the nucleation of quantized magnetic flux tubes, *Abrikosov vortices* [2], in a field range  $H_{c1} < H < H_{c2}$ , where  $H_{c1}$  and  $H_{c2}$  are the *lower* and *upper critical field* respectively, enables the persistence of the superconducting state in high applied magnetic fields, enhancing their technological relevance. However, all the technological applications are still dealing with the capability to control and prevent vortex motion, which causes energy dissipation, eventually introducing artificial pinning sites. In such a scenario, the nanoscale investigation of the superconducting vortex dynamics holds the potential of understanding macroscopic behaviors in terms of microscopic mechanism. Among all the techniques able to perform experiments at the nanoscale, *Magnetic Force Microscopy* (MFM) and *Scanning Tunneling Microscopy and Spectroscopy* (STM/STS) allow the investigation of the superconducting vortex arrangement with individual vortex resolution, keeping track of the magnetic polarity and in high applied magnetic field respectively.

Planar Superconductor/Ferromagnet (S/F) heterostructures, magnetically coupled, i.e. having an insulating thin layer between the S and F films to suppress the proximity effect [3], have been proposed to increase the vortex pinning, due to the interaction between superconducting vortices and magnetic template. However, being the vortex physics highly sensitive to the nano-variation in size and geometry of the constituting materials, the investigation of such systems requires preliminary efforts in:

1. modeling the magnetostatic interaction between the S layer in the mixed state and the F film;
2. identifying the proper superconductor, insulator and ferromagnet;
3. rescaling S and F thickness in order to make thin film based heterostructures.

In the past, a lot of effort has been spent to experimentally probe and theoretically model many of the exciting effects that can occur in magnetically coupled S/F hybrids having artificial, lithographically defined, magnetic nanotextures as well as on planar S/F bilayers. Such works focused primarily on the effects of the underlying magnetic template on vortex nucleation, vortex dynamics, and on the nucleation of localized superconductivity above domains and domain walls [4]-[22]. This remarkable and solid background, very briefly reviewed in Chapter 1, guided the experiments discussed in this dissertation and helped in the interpretation of the data.

The focus of the presented thesis is on the study of vortex nucleation, pinning and dynamics in planar S/F hybrids, made by thin films of Nb/Py and Pb/[Co/Pd]<sub>multilayers</sub>. The fabrication of the constituting superconductors (Nb and Pb), insulators ( $SiO_2$  and  $Al_2O_3$ ) and ferromagnets (Py and [Co/Pd]<sub>multilayers</sub>) as well as the deposition procedures are beyond the goal of this dissertation. Shortly, Nb/ $SiO_2$ /Py hybrids were made by sputtering deposition at *Argonne National Laboratory* (Chicago, IL (USA)) by Dr. V. Novosad, Dr. V. Yefremenko and Dr. S.A. Moore, [Co/Pd]<sub>multilayers</sub>/ $Al_2O_3$  were fabricated by Dr. V. Novosad, whereas Pb thin films were made by electron beam deposition at *Temple University* (Philadelphia, PA (USA)) by Dr. S.A. Moore. The choice of the materials is strongly dependent on the investigating technique. The ferromagnetic domain size as well as the weakness of the out-of-plane magnetic stray field of Py are suitable for MFM experiments, whereas, on the contrary, [Co/Pd]<sub>multilayers</sub>, having a relatively high out-of-plane stray field, would cause a magnetic overlapping of superconducting vortices, eventually not individually resolvable by MFM. On the contrary, the vortex-vortex separation induced by the Py magnetic template as well as the domain size would be too big for STM/STS investigation. In addition to this, while Nb is not a good material for STM measurements, due to the ease in oxidation, Pb, with a  $T_c = 7.2K$ , is not suitable for the presented MFM experiments, performed in an Omicron-Scanning Force Microscope, limited by a base temperature of 5K.

The working principle of MFM and STM/STS is presented in Chapter 2, followed by the description of the cryogenic Ultra-High Vacuum systems used in performing the scanning probe microscopy experiments.

In Chapter 3, low temperature MFM experiments on Nb/Py hybrids are presented with the aim of investigating the conditions of spontaneous vortex nucleation as well as their in-field behavior. Being Nb a conventional low-temperature superconductor and Py a room temperature ferromagnet with a peculiar stripe-like configuration of the out-of-plane magnetic domains, a field cooling of Nb in the spatially non-uniform Py stray field occurs every time the S film is cooled down below its critical temperature ( $T_s \approx 9K$ ). In such a way, depending on the intensity of the out-of-plane component  $M_0$  of the Py magnetization vector, alternating up and down, *spontaneous* quantum fluxes with opposite polarities, vortex - antivortex (V-AV) pairs, can be nucleated in Nb film and guided along the magnetic channels. As a consequence, the nucleation of spontaneous V-AV can be indirectly tuned, by increasing the intensity of  $M_0$ , by making thicker F films or by decreasing the S thickness. In addition to this, MFM measurements in external (static and dynamic) magnetic field are presented, with the aim of studying vortex dynamics.

In Chapter 4, peculiar vortex distribution in presence of strong, randomly distributed, pinning sites, called *bifurcations* of the magnetic template, have been studied in Nb/Py by low temperature MFM as well as in Pb/[Co/Pd]*multilayers* by low temperature STM/STS. It has been shown how the enhancement of the stray field at the bifurcation core as well as the topology of the bifurcation itself definitely affect vortex arrangement, bringing to the formation of strongly confined vortex cluster. The complementarily of MFM and STM/STS has been successfully used to get insights into the vortex confinement matter.

Finally, in Chapter 5, a new method to perform quantitative MFM experiments is developed and presented. The main idea is to extract a magnetic characterization of the MFM tip by probing a sample with well known magnetic signal. The superconducting vortex, always supporting a flux quantum  $\Phi_0 = \frac{hc}{2e}$ , is thus a perfect object to use in developing such a characterization procedure. Moreover, an example of quantitative MFM experiment on Nb/Py is presented, bringing to the estimate of the out-of-plane magnetization component  $M_0$  of  $1\mu m$ -Py film.



# Bibliography

- [1] V. L. Ginzburg and L. D. Landau, *J. Exptl. Theoret. Phys.* **20**, 1064 (1950)
- [2] A.A. Abrikosov, *Sov. Phys. JETP* **5**, 1174 (1957)
- [3] A.I. Buzdin, *Rev. Mod. Phys.* **77**, 935 (2005)
- [4] S. Erdin, I. F. Lyuksyutov, V. L. Pokrovsky, and V. M. Vinokur, *Phys. Rev. Lett.* **88**, 1 (2002)
- [5] G.M. Genkin, V.V. Skuzovaktin, I.D. Tokman, *J. Magn. Magn. Mater.* **130**, 51 (1993)
- [6] I.K. Marmoros, A. Matulis and F. M. Peeters, *Phys. Rev. B* **53**, 2677(1996)
- [7] R. Lahio, E. Lähderanta, E. B. Sonin, K.B. Traito, *Phys. Rev. B* **67**, 144522 (2003)
- [8] A.I. Gubin, K.S. Il'in, S.A. Vitusevich, M. Siegel, N. Klein, *Phys. Rev. B* **72**, 064503 (2005)
- [9] M.V. Milosevic, and F. M. Peeters, *Physica C* **404**, 246 (2004)
- [10] Q.H. Chen, C. Carballeira and V. V. Moshchalkov, *Phys. Rev. B* **79**, 104520 (2009)
- [11] , J.C. Piña, M. A. Zorro and C. C. de Souza Silva, *Physica C* **470**, 762 (2010)
- [12] M.V. Milosevic, F. M. Peeters and B. Jank, *Supercond. Sci. Technol.* **24**, 024001, (2011)
- [13] L. N. Bulaevskii, and E. M. Chudnovsky, M. P. Maley, *Appl. Phys. Lett.* **76**, 18 (2000)

- 
- [14] J. Ze, Y. Huadong and Z. You-He, *Supercond. Sci. Technol.* **27**, 105005 (2014)
- [15] A.A. Bespalov, A.S. Melnikov and A. I. Buzdin, *EPL (Europhysics Letters)* **110**, 37003 (2015)
- [16] A.Y. Aladyshkin, A. I. Buzdin, A. A. Fraerman, A. S. Mel'nikov, D. A. Ryzhov and A. V. Sokolov, *Phys. Rev. B* **68**, 184508 (2003)
- [17] A.Y. Aladyshkin, and V. V. Moshchalkov, *Phys. Rev. B* **74**, 064503 (2006)
- [18] Aladyshkin, A. Y., D. A. Ryzhov, A. V. Samokhvalov, D. A. Savinov, A. S. Mel'nikov and V. V. Moshchalkov, *Phys. Rev. B* **75**, 184519 (2007)
- [19] Aladyshkin, A. Y., A. S. Mel'nikov, I. M. Nefedov, D. A. Savinov, M. A. Silaev and I. A. Shereshevskii, *Phys. Rev. B* **85**, 184528 (2012)
- [20] M. Houzet, and A. I. Buzdin, *Phys. Rev. B* **74**, 214507 (2006)
- [21] S.V. Mironov, and A. S. Melnikov, *Phys. Rev. B* **86**, 134505 (2012)
- [22] A.Z. Miguel, S. Tiago and C. d. S. S. Clécio, *Supercond. Sci. Technol.* **27**, 055002 (2014)

# Chapter 1

## S/F hybrids

### 1.1 Introduction

Superconductivity has a great potential to play a significant role in the development of new clean energy technologies by minimizing the losses in electrical current transport. However, the widespread use of superconducting materials is still limited by a few critical parameters, such as critical current, critical magnetic field and critical temperature and, therefore, the active research on new superconducting technologies is underway.

Conventional superconductors are well described in the framework of the Ginzburg-Landau (G-L) theory [1]. Within G-L theory, the introduction of the G-L parameter  $k = \frac{\xi}{\lambda}$  leads to differentiation between type I and type II superconductors for cases when  $k > \frac{1}{\sqrt{2}}$  and  $k < \frac{1}{\sqrt{2}}$ , respectively. The two characteristic superconducting length scales, the *coherence length*  $\xi$  and *penetration depth*  $\lambda$ , are intimately related to the superconducting material. The superconducting order parameter describing the local density of the superconducting Cooper pairs varies at length scale defined by the coherence length, while the penetration depth characterizes the distance at which the external magnetic field is exponentially screened from the interior of a superconducting sample (*Meissner effect*). In type II superconductors, the nucleation of quantized magnetic flux tubes, *Abrikosov vortices*, enables the persistence of the superconducting state in high applied magnetic fields up to the upper critical field  $H_{c2}$  at which the superconductivity is destroyed. The mixed state (or Shubnikov state) of type

II superconductors persists in applied magnetic fields  $H$  between  $H_{c1} < H < H_{c2}$ , where  $H_{c1}(T)$  and  $H_{c2}(T)$  are the lower and upper critical fields, respectively, making these materials very technologically relevant. It has been theoretically predicted by Abrikosov [2] and later experimentally shown by Trauble and Essman [3] that the mixed state is a macroscopic quantum fluid having each vortex carrying a flux quantum  $\Phi_0 = \frac{h}{2e}$ , where  $h$  is the Planck constant and  $e$  is the electron charge. The vortex causes a local suppression of the superconducting order parameter on the length scale of  $\xi$ , while  $\lambda$  measures the exponential decay of the magnetic field when moving away from the vortex core. In 1957, Abrikosov predicted a lattice arrangement of vortices (fig. 1.1) in order to minimize the energy of the system. The vortex lattice period  $d$  is set by the intensity of the external magnetic field  $H$  according to the relation  $d = \sqrt{\frac{2\Phi_0}{\sqrt{3}H}}$ .

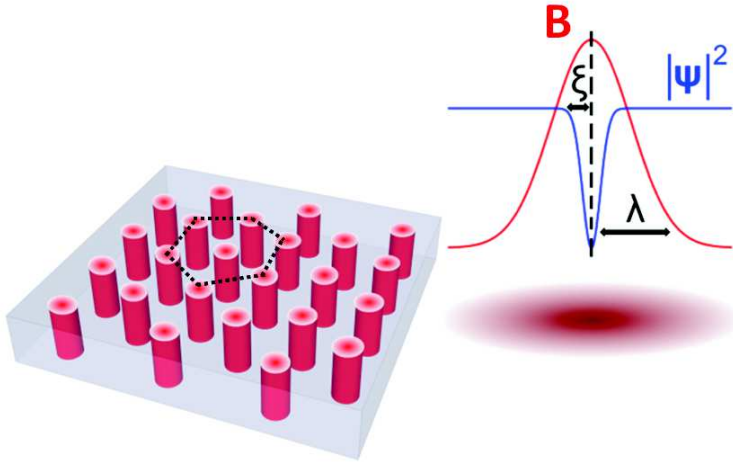


**Figure 1.1:** Periodic arrangement of vortices in a type-II superconductor in an external applied magnetic field  $\vec{B}$ . Each vortex has a normal core, where the amplitude of the superconducting order parameter  $|\psi|^2$  (blue line) drops to zero on the scale of  $\xi$  while the magnetic field profile (red line) exponentially decays on the scale of  $\lambda$ .

When an external current, exceeding the critical value, is applied to a superconductor in the mixed state, vortices are forced to move under the action of the Lorentz force causing energy dissipation. For this reason, the control of the vortex dynamics is one of the main challenges for technological applications and fundamental science. In order to restore a dissipation-free regime, the driving Lorentz force has to be counterbalanced

by a pinning force. In this scenario, the technological applications of type II superconductors deal with the capability to create and control pinning centers that locally induce a suppression or reduction of the superconducting order parameter. Lattice defects, dopant inclusions or peculiar sample geometry have been proposed in order to impose a pinning potential for the superconducting vortices [4]. An enhancement of the critical current has been reported by bulk processing of the superconductors to create pinning centers and by lithographic patterning of arrays of pinning centers. Magnetic pinning centers have also been widely used for enhancing vortex pinning properties since they locally suppress the superconducting order parameter (pair-breaking effect of the local magnetic moment) and magnetically attract vortex lines. Several methods of introducing magnetic pinning centers have been employed from deposition of magnetic nanoparticles to lithographically defining magnetic nanotextures on the superconducting layer [5] - [29].

Superconductor/Ferromagnet (S/F) thin film heterostructures, magnetically coupled in order to suppress the proximity effect [30], in which the ferromagnetic domains act as pinning centers, have been of great interest due to ease of fabrication, scalability for future applications, and due to basic fundamental physics governing the superconductivity in this hybrid systems [32] - [48].

## 1.2 Superconductor/Ferromagnet hybrids

In 1957 John Bardeen, Leon Cooper and Robert Schrieffer derived the microscopic theory of superconductivity in which, below a critical temperature  $T_c$ , electrons at the highest-energy filled states - the *Fermi surface* - build Cooper pairs with zero center-of-mass momentum, zero total spin (a spin singlet), and charge  $2e$ , constituting the superconducting condensate. Excitations above the condensate need a minimum finite energy  $|\Delta|$ , the so-called excitation gap [49], [50].

Slightly earlier, in 1956, Vitaly Ginzburg brought up the problem of coexistence of ferromagnetism and superconductivity, focusing on the so called *orbital-mechanism* [51]. Later, in 1958 Bernd Matthias, Harry Suhi and Ernest Corenzwit suggested an additional mechanism of interaction between superconductivity and ferromagnetism: the *quantum-mechanical exchange interaction* [52].

The condensate of conventional superconductors is definitely influenced by the exchange field of a ferromagnet as well as by its magnetic field, which can strongly reduce the

superconducting correlations. If the exchange field is sufficiently strong, it tries to align the spin of the electrons of a Cooper pair, that in the usual case of singlet superconductors are antiparallel, thus destroying the superconductivity. Those antagonistic tendencies lead to the so-called *paramagnetic effect* of pair breaking. A similar situation arises when the magnetic field is applied to Cooper pairs, where the role of the exchange interaction is played by the Zeeman interaction. In both cases, the interaction spin-polarizes the electrons, splits the energy levels depending on the direction of the spins (parallel or antiparallel to the external magnetization vector) by an amount given by twice the exchange or the Zeeman energy, and breaks apart the opposite-spin singlet Cooper pairs. In such a scenario, the strong interaction between the two S and F subsystems can dramatically change the properties of each constituting material.

A natural way to avoid the proximity effect consists in separating the S and F layers by a thin insulating film. In such a way S and F systems interact via the magnetic field induced by F-texture. Such textures can be either artificial (dots, wires) or topological (planar hybrids with F in multi-domain magnetic state). Here, the magnetic field coming out from F induces screening currents in S.

The calculation of vortex arrangement for interacting, spatially separated superconductors and ferromagnets is based on the static London-Maxwell equations. In particular, London's approximation works satisfactorily since the sizes of all structures in the problem exceed significantly the coherence length  $\xi$ . Whenever the proximity effects dominate, the London equation is not valid anymore.

### 1.3 Orbital Coupling

Nucleation and control of superconducting vortices via the underlying magnetic template is one of the main goal of studying S/F hybrid in orbital coupling [34], [53]-[57]. Particularly exciting is the possibility to substantially increase the vortex pinning due to the magnetic template, thereby increasing the critical current [32], [58].

Artificial periodic vortex pinning was first produced by modulating the S-film thickness by Daldini *et al.* [59]. Slightly later Hebard *et al.* used triangular arrays of holes[60],[61]. However, magnetic structures provide additional advantages in pinning vortices, whereas their pinning potential depends on several factors: orientation of the magnetic moment, strength of the stray field, ratio of magnetic domain size (or dot lattice constant) to the effective penetration depth, strength and direction of the ex-

ternal field.

In the past, a lot of effort has been spent both theoretically and experimentally in investigating many of the exciting effects that can occur in magnetically coupled S/F hybrid systems having artificial, lithographically defined, magnetic nanostructures as well as on planar S/F bilayers. Such works focused primarily on the effects of the underlying magnetic template on vortex nucleation [34], [53]-[57], [62]-[64], vortex dynamics [32], [65], [24], and on the nucleation of localized superconductivity above domains and domain walls [47],[48],[67]-[73].

In the 90s, the first experiments with a regular array of magnetic dots, magnetized in plane, were performed in the Louis Neel Laboratory in Grenoble [5],[74], as well as a dot array with out-of-plane magnetization was first prepared and studied by Morgan and Ketterson [75]. By measuring the critical current as a function of the external magnetic field, they found a strong asymmetry of the pinning properties under magnetic field reversal, proving for the first time, that vortex pinning by magnetic dots is different from that of non-magnetic pinning centres. Here in after experiments on nanostructured S/F hybrids has been focused on pinning properties of magnetic dot arrays covered by a thin superconducting film, as well as on the competing periodicity of artificial array of dots and vortex lattice (with periodicity fixed by the external magnetic field). The so-called matching field was found: whenever the vortex lattice, tuned by the external field, is commensurate with the lattice of pinning centers an increase of pinning strength occurs (with a precipitous drop in resistivity [76]).

Even more interesting is the situation having vortices of opposite polarities (namely *vortices* and *antivortices*) induced by magnetic dots. The spontaneous formation of vortex-antivortex pairs due to perpendicularly magnetized dots has been theoretically addressed by Erdin [77]. He assumed that each dot creates only one vortex in the S film right on the top of it as well as one antivortex in the interstitial position and he studied the symmetry of the vortex-antivortex lattice as a function of  $\frac{R}{L}$  and  $\frac{Lm\Phi_0}{\epsilon_V}$ , where  $R$  is the dot radius,  $L$  is the dot lattice constant,  $m$  is the dot magnetization and  $\epsilon_V$  is the energy of the vortex in absence of the magnetic dot.

Moreover, planar S/F hybrids, with F magnetized in the out-of-plane direction, allow for the investigation of the fundamental properties underlying the magnetic interaction between superconducting and ferromagnetic layers, without any need of lithographic steps. Lyuksyutov and Prokrovsky argued that such a system is unstable with respect to the spontaneous formation of vortices of one vorticity[78]. Only when the ferromag-

netic film splits into domains with alternating magnetization, spontaneous vortices and antivortices, with opposite circulation directions, might appear. Such a domain structure makes the transport properties of these S/F bilayers strongly asymmetric. Kayali and Pokrovsky have calculated the pinning force on superconducting vortices due to a stripe-like configuration of magnetic domains, showing that in absence of a driving force they line themselves up in straight chains [58]. In presence of a permanent current, critical currents have been calculated in both parallel and perpendicular configurations. Theory predicts a strong anisotropy of the critical current resulting in a ratio of the parallel to perpendicular critical current in the range  $10^2 - 10^4$ . The anisotropy is associated with the fact that the motion of vortices is very different if the current is perpendicular or parallel to the domain walls. In perpendicular configuration, vortices move along the proper magnetic channels, whereas the antivortices, in neighboring domains, move in opposite directions. In such a case, the stripe pinning is very small. In the case of parallel current all vortices are forced to move across the domain walls which instead provide very strong periodic pinning force. From the experimental point of view, such anisotropy in vortex motion has been measured, for instance, by Karapetrov *et. al* in S/F/S trilayers [80]. They found an increase of the critical current in parallel direction three to five times the one in perpendicular direction, still extremely small with respect to the theoretical predictions.

### 1.3.1 Magnetostatic Interaction

The total energy of a S/F bilayer, only magnetically coupled, can be written as follow:

$$U = U_{SV} + U_{VV} + U_{VM} + U_{mm} + U_{dw} \quad (1.1)$$

where  $U_{SV}$  is the sum of energies of single vortices,  $U_{VV}$  is the vortex-vortex interaction,  $U_{VM}$  is the energy of interaction between superconducting vortices and underlying magnetic template,  $U_{mm}$  is the self-interaction energy of the magnetic layer and  $U_{dw}$  is the surface tension energy of the domain walls. For simplicity, let's assume to be in presence of a periodic domain structure consisting of two equivalent sublattices. In such a case the magnetization  $M_{0,z}(\vec{r})$  alternates when passing from one sublattice to another, with vortex density  $n(\vec{r})$ . Magnetization is supposed to have a constant absolute value  $M_{0,z}(\vec{r}) = M_0 s(\vec{r})$ , where  $s(\vec{r})$  is the periodic step function equal to  $\pm 1$

at one sublattice and  $-1$  at the other one. The single-vortex energy is given by:

$$U_{SV} = (\varepsilon_V^0 - M_0 \Phi_0) \int n(\vec{r}) s(\vec{r}) d^2 x \quad (1.2)$$

where  $\varepsilon_V^0 = \frac{\Phi_0}{16\pi^2 \lambda^2} \ln\left(\frac{\lambda}{\xi}\right)$  is the single vortex energy, in absence of a magnetic template. The vortex-vortex interaction is the following:

$$U_{VV} = \int n(\vec{r}) V(\vec{r} - \vec{r}') s(\vec{r}') d^2 x d^2 x' \quad (1.3)$$

where  $V(\vec{r} - \vec{r}')$  is the pair interaction energy between vortices located at the points  $\vec{r}$  and  $\vec{r}'$ . The interaction energy between vortices and the magnetic field generated by F is:

$$U_{vm} = -\frac{\Phi_0}{8\pi^2 \lambda} \int \vec{\nabla} \phi(\vec{r} - \vec{r}') n(\vec{r}') \cdot \vec{a}^{(M_0)}(\vec{r}) d^2 x d^2 x' \quad (1.4)$$

where  $\phi(\vec{r} - \vec{r}')$  is a phase shift created at a point  $\vec{r}$  by a vortex centered at  $\vec{r}'$  and  $\vec{a}^{(m)}(\vec{r})$  is the value of the vector potential induced by the F-film upon the S-film. The magnetic self-interaction is given by:

$$U_{mm} = -\frac{M_0}{2} \int B_z^{(M_0)}(\vec{r}) s(\vec{r}) d^2 x \quad (1.5)$$

Finally, the energy of domain walls is:

$$U_{dw} = \varepsilon_{dw} L_{dw} \quad (1.6)$$

where  $\varepsilon_{dw}$  is the linear tension of the domain wall and  $L_{dw}$  is its total length.

Erdin *et al.* [34],[79] have compared energies of stripe, square and triangular domain wall lattices and found that the stripe structure has the lowest energy.

### 1.3.2 Planar S/F hybrids with ferromagnetic stripe domains

In the framework of S/F bilayers in which the ferromagnet exhibits stripe-like magnetic domains, with alternating up-and-down out-of-plane magnetization vectors  $\pm \vec{M}_0$ , the magnetization values required for spontaneous vortex-antivortex nucleation can be deduced, for given values of stripe domain width  $w$  of F layer, superconducting penetration depth  $\lambda$  and thickness  $d_s$  of S film. Starting from eq.1.1, two different theoretical models dealing with the two opposite limits of superconductor film thickness greater [55] and smaller [53] than the penetration depth,  $\frac{d_s}{\lambda} > 1$  and  $\frac{d_s}{\lambda} < 1$  respectively, addressed the problem of spontaneous vortex nucleation.

In presence of a dilute vortex system (vortex-vortex distance much greater than the penetration depth) the  $U_{VV}$  energy can be neglected, as well as  $U_{mm}$  and  $U_{dw}$ , under the assumption that the ferromagnet is quenched below the superconducting critical temperature. In such a way,  $U_{mm}$  and  $U_{dw}$  can be considered as constants, simply causing a rescaling of the total energy.

In the limit of  $\frac{w}{\lambda} > 1$  and  $\frac{d_s}{\lambda} > 1$ ,  $U_{SV} = \frac{\Phi_0 H_{c1} l}{4\pi}$ , where  $H_{c1} = \frac{\Phi_0}{4\pi\lambda^2} \ln\left(\frac{\lambda}{\xi}\right)$  is the lower critical field and  $l$  is the vortex length, and  $U_{vm} = -\sum_i \frac{\varepsilon_i \Phi_0 \varphi(\vec{r}_i)}{4\pi}$ , where  $\varepsilon_i = \pm 1$  depends on the direction of the vortex flux,  $\vec{r}_i$  is the position of the vortex in the interface plane and  $\varphi(\vec{r}_i) = \pm 8M_0 \int_0^{r_i} \ln \tan\left(\frac{\pi x}{2w}\right) dx$  is the magnetic potential. By requiring:

$$U = 2U_{SV} + U_{VM} < 0 \quad (1.7)$$

the threshold magnetization values needed to nucleate the first straight vortex-antivortex pair  $M_{cs}$  (with length  $l = d_s$ ) (fig.1.2a), which pierces through the superconducting film, or the first vortex semiloop  $M_{cl}$  (fig.1.2b), which is bent within the superconducting film, result in:

$$M_{cs} = 0.2 \frac{d_s}{w} H_{c1} \quad (1.8)$$

$$M_{cl} = \frac{H_{c1}}{8 \ln\left(\frac{4w}{\pi\lambda}\right)} \quad (1.9)$$

respectively. If  $M_{cl} > M_{cs}$ , the formation of straight vortices is energetically favorable, and vice versa. The energy profiles of a straight (red) and semiloop (blue) vortex are shown in fig.1.2c indicating that the minimum energy of the straight vortex is achieved in the middle of the magnetic stripe domain, whereas the semiloop vortex crosses over the stripe domain wall [55].

On the other hand, in the opposite limit of  $\frac{w}{\lambda} > 1$  and  $\frac{d_s}{\lambda} < 1$ , the model of Genkin et al. has to be taken into account [53], where the threshold magnetization for spontaneous straight vortex nucleation results in:

$$M_c = \ln\left(\frac{\lambda_{eff}}{\xi}\right) \left(\frac{\Phi_0}{(4\pi)^2}\right) \frac{1}{w\lambda_{eff}} \quad (1.10)$$

with  $\lambda_{eff}(T) = \lambda(T) \coth\left(\frac{d_s}{\lambda(T)}\right)$  [56], being the penetration depth affected by the superconducting thickness. In the latter, spontaneous vortex formation will thus be energetically regulated by the threshold condition  $M_0 > M_c$ .

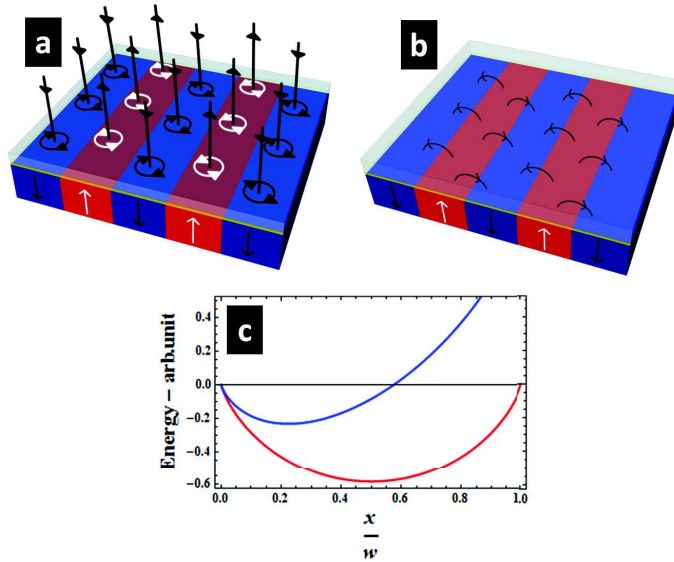


**Figure 1.2:** 3D representation of a magnetically-coupled S/F heterostructure with the F layer in the stripe regime. a) in black and white the screening supercurrents are shown, straight Vortices and Anti-vortices piercing the superconducting layer are represented by the straight arrows; b) semi-loop vortices close inside the superconducting layer; c) plot of the straight vortex (red) and semi-loop vortex (blue) energy as a function of the position across the stripe.

## 1.4 Exchange Coupling

An alternative approach to the study of the S/F systems consists in favoring the electrical coupling between S and F layers. In such a case the exchange field existing in the ferromagnet splits the Fermi spheres for up and down spin, giving to the Cooper pair two options for survival. It can keep its spins pointing in opposite directions with respect to the magnetization vector and acquire instead a nonzero center-of-mass momentum or it can become an equal-spin pair, in which the two spins point in the same direction with respect to the magnetization vector. That first possibility was independently discovered in 1964 by Peter Fulde and Richard Ferrell at the University of Maryland and by Anatoly Larkin and Yurii Ovchinnikov at the Moscow Physico-Technical Institute [81], [82]. For this reason, it is known as the FFLO state (Fulde and Ferrell in fact submitted and published slightly earlier). The FFLO state exhibits an inhomogeneous pair wavefunction that oscillates periodically in space. As shown in fig.1.3a, due to spin-spin interactions in ferromagnet, the electronic bands for up

spins (blue) and down spins (red) are shifted with respect to each other by an amount  $2E_{ex}$ . That exchange splitting shifts the momenta at the Fermi energy  $E_F$  from  $k_F$  to the new positions  $\vec{k}_{F\uparrow} = \vec{k}_F + \frac{\vec{Q}}{2}$  and  $\vec{k}_{F\downarrow} = \vec{k}_F - \frac{\vec{Q}}{2}$ . In this condition, two electrons at the Fermi energy with opposite spin and momenta  $\vec{k}_{F\uparrow}$  and  $\vec{k}_{F\downarrow}$  form a Cooper pair with center-of-mass momentum  $\pm\vec{Q}$ . By doing this, the contributions to the pair amplitude are proportional to  $e^{\pm i(\vec{k}_{F\uparrow} - \vec{k}_{F\downarrow}) \cdot \vec{R}}$ , thus leading to a modulation of the pair amplitude with position  $\vec{R}$ . The FFLO state was predicted as an intrinsic, bulk effect, however the existence of FFLO-type states was established without doubt in the early 2000s in ferromagnetic metals in contact with a superconductor, the so-called proximity structures. The *proximity effect* describes penetration of the pair amplitude from a superconductor into an adjacent metal (normal or ferromagnet).

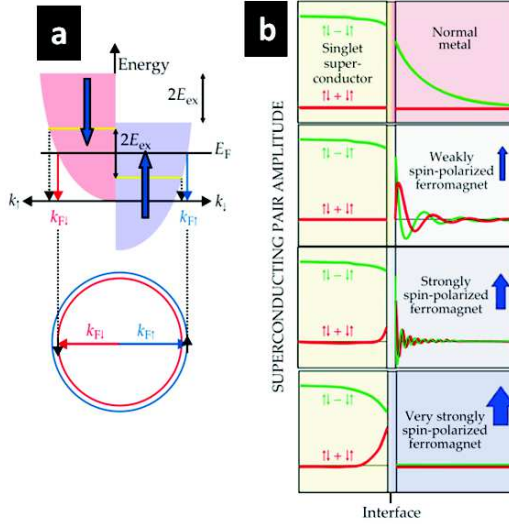


**Figure 1.3:** a) Shift of up-spin band (red) and down-spin band (blue) due to the exchange interaction in a ferromagnet. Such a splitting shifts the momenta at the Fermi energy  $E_F$  from  $\vec{k}_F$  to  $\vec{k}_{F\uparrow} = \vec{k}_F + \frac{\vec{Q}}{2}$  and  $\vec{k}_{F\downarrow} = \vec{k}_F - \frac{\vec{Q}}{2}$ . b) Amplitude of the pair wavefunction as a function of distance from the superconductor-metal interface, in the case of a normal metal, weakly, strongly and very strongly spin-polarized ferromagnet. Figure adapted from [85]

Figure 1.3b plots the amplitude of the pair wavefunction as a function of distance from the superconductor-metal interface. In the case of a normal metal, the singlet state (green) penetrates over large distances, typically on the order of microns and increasing with decreasing temperature, being  $\xi_N = \sqrt{\frac{\hbar D}{2\pi K T}}$  and  $\xi_N = \frac{\hbar v_F}{2\pi K T}$  the propagation length in the normal metal of the condensation amplitude respectively

in the diffusive and ballistic limit, where  $D$  is the electronic diffusion constant,  $k$  is the Boltzmann constant and  $v_F$  is the Fermi velocity. In contrast, in ferromagnets the proximity effect induces FFLO amplitudes -both singlet (green), and triplet (red) with zero spin projection on the magnetization axis- that oscillate and penetrate over a length scale that rapidly becomes shorter as the exchange splitting  $E_{ex}$  increases, being  $\xi_F = \sqrt{\frac{\hbar D}{2E_{ex}}}$  and  $\xi_F = \frac{\hbar v_F}{2E_{ex}}$  the propagation length in the ferromagnet of the condensation amplitude respectively in the diffusive and ballistic limit. In the limit of large exchange splitting, corresponding to strongly spin-polarized ferromagnets, Cooper pairs can penetrate only over atomically short distances into the barrier between the superconductor and the ferromagnet, and not into the ferromagnet itself. At the same time, the internal structure of Cooper pairs in the superconductor is strongly modified near the interface. That modification is due to phase shifts that electrons acquire when quantum mechanically penetrating into the interface barrier regions. The net phase difference  $\theta$  acquired during reflection leads to singlet-triplet mixing of Cooper pairs in a layer roughly  $15 - 150nm$  thick next to the interface, depending on the material.

Despite the success from a fundamental perspective, one problem for practical applications became quickly evident: for a clear and controllable effect, weakly spin-polarized systems, like ferromagnetic copper-nickel or palladium-nickel alloys, must be used otherwise the proximity amplitudes become too short ranged. But the rapidly developing field of spintronics had provided strong motivation to search for long-range proximity effects in ferromagnets. Such long range amplitudes would lead to long-range supercurrents and to valuable applications. The ultimate goal is to find completely spin-polarized supercurrents, which would necessarily have to be triplet with non-zero spin projection on the magnetization axis. It was clear very early that in the case of pairs composed of two equal spins ( $\uparrow\uparrow$  or  $\downarrow\downarrow$ ), the two  $\uparrow$  spins at the Fermi energy can pair with equal and opposite momenta,  $k_{F\uparrow}$  and  $-k_{F\uparrow}$ , without introducing a finite center-of mass momentum, and likewise for two  $\downarrow$  spins. Thus, no oscillations will occur for equal-spin proximity amplitudes, and the penetration is long range, meaning that the penetration length behaves as it does in a normal metal, increasing to microns with decreasing temperature. At this point, the biggest obstacle became how to create an appreciable amount of such equal-spin pairs, which are triplet states not suppressed by the exchange field, i.e. with non-zero spin projection on the magnetization axis. Starting from 2001, several papers theoretically analyzed examples of S/F structures in which the triplet component are induced. The common feature of these structures

is that the magnetization is not homogeneous [86], [87]. It is well known, for instance, that the magnetization of any ferromagnet can be quite inhomogeneous due to the presence of domain walls.

### 1.4.1 Proximity effect in S/F hybrids

The essence of proximity phenomena is the change of the order parameter (Cooper pair wavefunction), which oscillates in space inside the ferromagnetic layer. Therefore, the London approximation is not valid anymore and equations for the order parameter must be solved. They are either the Bogolyubov de Gennes equations [88],[89] or more conveniently the Gor'kov equations [90] for the Green functions. Unfortunately the solution of these equations is not an easy problem in the spatially inhomogeneous case, combined with the scattering by impurities and/or irregular boundaries, that is a typical situation for experimental investigation of S/F proximity effects. Fortunately, if the scale of variation of the order parameter is much larger than atomic, the semiclassical approximation can be applied. Equations for the superconducting order parameter in the semiclassical approximation were derived a long time ago by Eilenberger [91] and by Larkin and Ovchinnikov [82]. They were further simplified in the case of strong elastic scattering (the diffusion approximation) by Usadel [92].

The oscillations of the order parameter lead to a series of interesting phenomena:

1. oscillations of the critical temperature versus the thickness  $d_f$  of magnetic layer;
2. periodic transitions from the 0- to  $\pi$ -phase in the S/F/S Josephson junction when varying the thickness  $d_f$  of the ferromagnetic layer and the temperature  $T$ ;
3. oscillations of the critical current versus  $d_f$  and  $T$ .

In S/F structures with a high interface transparency, the critical temperature of the superconducting transition  $T_c$  is considerably reduced, as theoretically calculated in many works [93] and experimentally reported in many publications [94]- [98]. Good agreement between theory and experiment as been achieved in some cases [99]. However, despite many papers published on this subject, the problem of the dependence of  $T_c$  on  $d_f$  is not completely clear. For example, Jiang *et al.* [94] and Ogrin *et al.* [100] claimed a nonmonotonic dependence of  $T_c$  on the thickness of the ferromagnet observed on Gd/Nb samples. However, Aarts *et al.* [95] in another experiment on V/FeV claimed that the interface transparency plays a crucial role in the interpretation of the experimental data, showing both nonmonotonic and monotonic dependence

of  $T_c$  on  $d_f$ . Moreover, Bourgeois *et al.* [101], showed a monotonic decrease of the Pb/Ni critical temperature with increasing  $d_f$ .

Although the experimental results concerning the behavior of  $T_c$  are still controversial, there is more evidence for these oscillations in experiments on the Josephson current measurements. It turns out that under certain conditions the Josephson critical current  $I_c$  changes its sign and becomes negative. This effect was first predicted by Bulaevskii *et al.* [102] in the case of two superconductors separated by a region containing magnetic impurities. Later, the Josephson current through a S/F/S junction was calculated for the first time by Buzdin *et al.* [103]. In this case the energy of the Josephson coupling  $E_J = \left(\frac{\hbar I_c}{e}\right) (1 - \cos \varphi)$  has a minimum in the ground state when the phase difference  $\varphi$  is equal not to 0, as in ordinary Josephson junctions, but to  $\pi$  (the  $\Pi$ -junction). Recent experiments confirmed the  $0 - \pi$  transition of the critical current in S/F/S junctions [104]- [108], together with oscillations of the critical current  $I_c$  as a function of  $T$  and  $d_f$ .

For a detailed review of advances in theoretical models as well as experimental results on proximity effect in S/F hybrids refer to [30].



# Bibliography

- [1] V. L. Ginzburg and L. D. Landau, *J. Exptl. Theoret. Phys.* **20**, 1064 (1950)
- [2] A.A. Abrikosov. *Sov. Phys. JETP* **5**, 1174 (1957)
- [3] U. Essmann and H. Trauble, *Phys. Lett.* **24**, 526 (1967)
- [4] A. M. Campbell, and J.E. Evetts, *Critical Currents in Superconductors - Monographs on Physics*, Taylor and Francis Ltd., London (1972)
- [5] Y. Otani, B. Pannetier, J. P. Nozieres, and D. Givord, *J. Magn. Magn. Mater.* **126**, 622 (1993)
- [6] M. Baert, V. V. Metlushko, R. Jonckheere, V. V. Moschalkov, and Y. Bruynseraede, *Phys. Rev. Lett.* **74**, 3269 (1995)
- [7] J. I. Martin, M. Velez, J. Nogues, and I. K. Schuller, *Phys. Rev. Lett.* **79**, 1929 (1997)
- [8] J. I. Martin, Y. Jaccard, A. Hoffman, J. Nogues, J. M. George, J. L. Vicent, and I. K. Schuller, *J. Appl. Phys.* **84**, 411 (1998)
- [9] J. I. Martin, M. Velez, J. Nogues, A. Hoffman, Y. Jaccard, and I. K. Schuller, *J. Magn. Magn. Mater.* **177**, 915 (1998)
- [10] J. I. Martin, M. Velez, A. Hoffman, I. K. Schuller, and J. L. Vicent, *Phys. Rev. Lett.* **83**, 1022 (1999)
- [11] M. V. Milosevic, and F. M. Peeters, *Phys. Rev. B* **68**, 094510 (2003)
- [12] D. B. Jan, J. Y. Coulter, M. E. Hawley, L. N. Bulaevskii, M. P. Maley, Q. X. Jia, B. B. Maranville, F. Hellman, and X. Q. Pan, *Appl. Phys. Lett.* **82**, 778 (2003)

- [13] M. Lange, M. J. Van Bael, Y. Bruynseraede, and V. V. Moshchalkov, *Phys. Rev. Lett.* **90**, 19 (2003)
- [14] M.V. Milosevic, and F. M. Peeters, *Physica C* **404**, 281 (2004)
- [15] M.V. Milosevic, and F. M. Peeters, *Phys. Rev. Lett.* **93**, 267006 (2004)
- [16] M. V. Milosevic and F. M. Peeters, *Phys. Rev. B* **69**, 104522 (2004)
- [17] M.V. Milosevic and F. M. Peeters, *Phys. Rev. Lett.* **94**, 227001 (2005)
- [18] A. V. Silhanek, W. Gillijns, M. V. Milosevic, A. Volodin, V. V. Moshchalkov, and F. M. Peeters, *Phys. Rev. B* **76**, 100502(R) (2007)
- [19] A. Angrisani Armenio, C. Bell, J. Aarts, and C. Attanasio, *Phys. Rev. B* **76**, 054502 (2007)
- [20] T. G. Holesinger, L. Civale, B. Maiorov, D. M. Feldmann, J. Y. Coulter, D. J. Miller, V. A. Maroni, Z. Chen, D. C. Larbalestier, R. Feenstra, X. Li, Y. Huang, T. Kodenkandath, W. Zhang, M. W. Rupich, and A. P. Malozemoff, *Adv. Mater.* **20**, 391 (2008)
- [21] T. Aytug, M. Paranthaman, K. J. Leonard, K. Kim, A. O. Ijaduola, Y. Zhang, E. Tuncer, J. R. Thompson, and D.K. Christen, *J. Appl. Phys.* **104**, 043906 (2008)
- [22] T. Shapoval, V. Metlushko, M. Wolf, V. Neu, B. Holzapfel, L. Schultz, *Physica C* **470**, 867 (2010)
- [23] T. Shapoval, V. Metlushko, M. Wolf, B. Holzapfel, V. Neu, and L. Schultz, *Phys. Rev. B* **81**, 092505 (2010)
- [24] A. V. Kapra, V. R. Misko, D. Y. Vodolazov, and F. M. Peeters, *Supercond. Sci. Technol.* **24**, 024014 (2011)
- [25] D.H. Tran, W.B.K. Putri, C.H. Wie, B. Kang, N.H. Lee, W.N. Kang, J.Y. Lee, W.K. Seong, *Thin Solid Films* **526**, 241 (2012)
- [26] O. Polat, M. Ertugrul, J. R. Thompson, K. J. Leonard, J. W. Sinclair, M. P. Paranthaman, S. H. Wee, Y. L. Zuev, X. Xiong, V. Selvamanickam, D. K. Christen and T. Aytug, *Supercond. Sci. Technol.* **25**, 025018 (2012)

- [27] V. Selvamanickam, Y. Chen, Y. Zhang, A. Guevara, T. Shi, Y. Yao, G. Majkic, C. Lei, E. Galtsyan and D. J. Miller, *Supercond. Sci. Technol.* **25**, 045012 (2012)
- [28] C.F. Tsai, J.H. Lee, and H. Wang, *Supercond. Sci. Technol.* **25**, 075016 (2012)
- [29] V. Selvamanickam, Y. Chen, T. Shi, Y. Liu, N. D. Khatri, J. Liu, Y. Yao, X. Xiong, C. Lei, S. Soloveichik, E. Galstyan and G. Majkic, *Supercond. Sci. Technol.* **26**, 035006 (2013)
- [30] A.I. Buzdin, *Rev. Mod. Phys.* **77**, 935 (2005)
- [31] A.V. Khoryushin, P. B. Mozhaev, J. E. Mozhaeva, N. H. Andersen, J.C. Grivel, J. B. Hansen, and C. S. Jacobsen, *Physica C* **485**, 39 (2013)
- [32] L. N. Bulaevskii, and E. M. Chudnovsky, M. P. Maley, *Appl. Phys. Lett.* **76**, 18 (2000)
- [33] M. Lange, M. J. Van Bael, V. V. Moshchalkov, and Y. Bruynseraede, *Appl. Phys. Lett.* **81**, 322 (2002)
- [34] S. Erdin, I. F. Lyuksyutov, V. L. Pokrovsky, and V. M. Vinokur, *Phys. Rev. Lett.* **88**, 1 (2002)
- [35] I. F. Lyuksyutov, and V. L. Pokrovsky, *Advances in Physics* **54**, 1 (2005)
- [36] M.V. Milosevic, G.R. Berdiyrov, and F. M. Peeters, *Phys. Rev. Lett.* **95**, 147004 (2005)
- [37] W. Gillijns, A. Yu. Aladyshkin, A. V. Silhanek, and V. V. Moshchalkov, *Phys. Rev. B* **76**, 060503(R) (2007)
- [38] A. Y. Aladyshkin, A. V. Silhanek, W. Gillijns and V. V. Moshchalkov, *Supercond. Sci. Technol.* **22**, 053001 (2009)
- [39] G. Karapetrov, M. V. Milosevic, M. Iavarone, J. Fedor, A. Belkin, V. Novosad, and F. M. Peeters, *Phys. Rev. B* **80**, 180506(R) (2009)
- [40] G. Carapella, P. Sabatino, and G. Costabile, *Phys. Rev. B* **81**, 054503 (2010)
- [41] H. Yamazaki, N. Shannon, and H. Takagi, *Phys. Rev. B* **81**, 094503 (2010)
- [42] L. Y. Zhu, Marta Z. Cieplak, and C. L. Chien, *Phys. Rev. B* **82**, 060503(R) (2010)

- [43] V. Vlasko-Vlasov, U. Welp, W. Kwok, D. Rosenmann, H. Claus, A. A. Buzdin, and A. Melnikov, *Phys. Rev. B* **82**, 100502(R) (2010)
- [44] A. Yu. Aladyshkin, A. S. Mel'nikov, I. M. Nefedov, D. A. Savinov, M. A. Silaev, and I. A. Shereshvskii, *Phys. Rev. B* **85**, 184528 (2012)
- [45] V. Vlasko-Vlasov, A. Buzdin, A. Melnikov, U. Welp, D. Rosenmann, L. Uspenskaya, V. Fratello, and W. Kwok, *Phys. Rev. B* **85**, 064505 (2012)
- [46] M. Z. Cieplak, Z. Adamus, M. Konczykowski, L. Y. Zhu, X. M. Cheng, and C. L. Chien, *Phys. Rev. B* **87**, 014519 (2013)
- [47] Z. Yang, M. Lange, A. Volodin, R. Szymczak, and V.V. Moshchalkov, *Nature Materials* **3**, 793 (2004)
- [48] M. Iavarone, S. A. Moore, J. Fedor, S. T. Ciocys, G. Karapetrov, J. Pearson, V. Novosad, S. D. Bader, *Nature Communications* **5**, 4766 (2014)
- [49] J. Bardeen, L. N. Cooper, and J. R. Schrieffer, *Phys. Rev.* **106**, 162 (1957)
- [50] J. Bardeen, L. N. Cooper, and J. R. Schrieffer, *Phys. Rev.* **108**, 1175 (1957)
- [51] V.L. Ginzburg, *Zh. Eksp. Teor. Fiz.* **31**, 202 [*Sov. Phys. JETP* **4**, 153 (1957)]
- [52] B.T. Matthias, H. Suhl, and C. Corenzwit, *Phys. Rev. Lett.* **1**, 152 (1958)
- [53] G.M. Genkin, V.V. Skuzovaktin, I.D. Tokman, *J. Magn. Magn. Mater.* **130**, 51 (1993)
- [54] I.K. Marmorkos, A. Matulis and F. M. Peeters, *Phys. Rev. B* **53**, 2677(1996)
- [55] R. Lahio, E. Lähderanta, E. B. Sonin, K.B. Traito, *Phys. Rev. B* **67**, 144522 (2003)
- [56] A.I. Gubin, K.S. Il'in, S.A. Vitusevich, M. Siegel, N. Klein, *Phys. Rev. B* **72**, 064503 (2005)
- [57] M.V. Milosevic, and F. M. Peeters, *Physica C* **404**, 246 (2004)
- [58] M.A. Kayali, and V. L. Pokrovsky, *Phys. Rev. B* **69**, 132501 (2004)
- [59] O. Daldini, P. Martinoli, J.L. Olsen and G. Berner, *Phys. Rev. Lett.* **32**, 218 (1974)

- [60] A.F. Hebard, A.T. Fiory and S. Somekh, *IEEE Trans. Magn.* **13**, 589 (1977)
- [61] A.T. Fiory, A.F. Hebard and S. Somekh, *App. Phys. Lett.* **32**, 73 (1978)
- [62] Q.H. Chen, C. Carballeira and V. V. Moshchalkov, *Phys. Rev. B* **79**, 104520 (2009)
- [63] , J.C. Piña, M. A. Zorro and C. C. de Souza Silva, *Physica C* **470**, 762 (2010)
- [64] M.V. Milosevic, F. M. Peeters and B. Jank, *Supercond. Sci. Technol.* **24**, 024001, (2011)
- [65] J. Ze, Y. Huadong and Z. You-He, *Supercond. Sci. Technol.* **27**, 105005 (2014)
- [66] A.A. Bespalov, A.S. Melnikov and A. I. Buzdin, *EPL (Europhysics Letters)* **110**, 37003 (2015)
- [67] A.Y. Aladyshkin, A. I. Buzdin, A. A. Fraerman, A. S. Mel'nikov, D. A. Ryzhov and A. V. Sokolov, *Phys. Rev. B* **68**, 184508 (2003)
- [68] A.Y. Aladyshkin, and V. V. Moshchalkov, *Phys. Rev. B* **74**, 064503 (2006)
- [69] Aladyshkin, A. Y., D. A. Ryzhov, A. V. Samokhvalov, D. A. Savinov, A. S. Mel'nikov and V. V. Moshchalkov, *Phys. Rev. B* **75**, 184519 (2007)
- [70] Aladyshkin, A. Y., A. S. Mel'nikov, I. M. Nefedov, D. A. Savinov, M. A. Silaev and I. A. Shereshevskii, *Phys. Rev. B* **85**, 184528 (2012)
- [71] M. Houzet, and A. I. Buzdin, *Phys. Rev. B* **74**, 214507 (2006)
- [72] S.V. Mironov, and A. S. Melnikov, *Phys. Rev. B* **86**, 134505 (2012)
- [73] A.Z. Miguel, S. Tiago and C. d. S. S. Clécio, *Supercond. Sci. Technol.* **27**, 055002 (2014)
- [74] O. Geoffroy, D. Givord, Y. Otani, B. Pannetier and F. Ossart, *J. Magn. Magn. Mater.* **121**, 223 (1993)
- [75] D.J. Morgan and J.B. Ketterson, *Phys. Rev. Lett.* **80**, 3614 (1998)
- [76] Gomez, A., E. M. Gonzalez, D. A. Gilbert, M. V. Milosevic, L. Kai and J. L. Vicent, *Supercond. Sci. Technol.* **26**, 085018 (2013)

- [77] S. Erdin, *Physica C* **391**, 140 (2003)
- [78] I.F. Lyuksyutov and V.L. Pokrovsky, *Mod. Phys. Lett. B* **14**, 409 (1999)
- [79] V.L. Pokrovsky and H. Wei, *Phys. Rev. B* **69** 104530 (2004)
- [80] G. Karapetrov, A. Belkin, M. Iavarone, V. Yefremenko, J.E. Pearson, R. Divan, V. Cambel, and V. Novosad, *Supercond. Sci. Technol.* **24**, 024012 (2011)
- [81] P. Fulde, and R.A. Ferrel, *Phys. Rev.* **135**, 550 (1965)
- [82] A.I. Larkin, and Y.N. Ovchinnikov, *Zh. Eksp. Teor. Fiz.* **55**, 2262 [*Sov. Phys. JETP* **20**, 762 (1965)]
- [83] I.F. Lyuksyutov and V.L. Pokrovsky, *Phys. Rev. Lett.* **81**, 2344 (1998)
- [84] D.E. Feldman, I.F. Lyuksyutov, V.L. Pokrovsky, and V.M. Vinokur *Europhys. Lett.* **51**, 110 (200)
- [85] M. Eschrig, *Physics Today* **64**, 43 (2011)
- [86] A. Kadigrobov, R.I. Shekhter and M. Johnson, *Europhys. Lett.* **54**, 394 (2001)
- [87] F.S. Bergeret, A.F. Volkov and K.B. Efetov, *Phys. Rev. Lett.* **86**, 4096 (2001)
- [88] N.N. Bogolyubov, *Zh. Eksp. Teor. Fiz.* **34**, 58; **34**, 73 [*Sov. Phys. JETP* **7**, 41; **7**, 51 (1958)]
- [89] P.G. de Gennes, *Rev. Mod. Phys.*, **36** 225 (1964)
- [90] L.P. Gor'kov, *Zh. Exp. Teor. Fiz.* **34**, 735 [*Sov. Phys. JETP* **7**, 505 (1958)]
- [91] G. Eilenberger, *Z. f. Physik* **214**, 195 (1968)
- [92] K. Usadel, *Phys. Rev. Lett.* **25**, 507 (1970)
- [93] A.I. Buzdin, and M. Y. Kupriyanov, *Pis'ma Zh. Eksp. Teor. Fiz.* **53**, 308 [*JETP Lett.* **53**, 321 (1991)]
- [94] J.S. Jiang, D. Davidovic, D. Reich, and C. L. Chien, *Phys. Rev. Lett.* **74**, 314 (1995)
- [95] J. Aarts, J.M.E. Geers, E. Brück, A. A. Golubov, and R. Coehoorn, *Phys. Rev. B* **56**, 2779 (1997)

- [96] T. Mühge, N. Garif'yanov, Y. V. Goryunov, K. Theis-Bröhl, K. Westerholt, I. A. Garifullin, and H. Zabel, *Physica C* **296**, 325 (1998)
- [97] L. Lazar, K. Westerholt, H. Zabel, L. R. Tagirov, Y. V. Goryunov, N. N. Garif'yanov, and I. A. Garifullin, *Phys. Rev. B* **61**, 3711 (2000)
- [98] Gu, J. Y., C.Y. You, J. S. Jiang, J. Pearson, Y. B. Bazaliy, and S. D. Bader, *Phys. Rev. Lett.* **89**, 267001 (2002)
- [99] L.Lazar, K. Westerholt, H. Zabel, L. R. Tagirov, Y. V. Goryunov, N. N. Garif'yanov, and I. A. Garifullin, *Phys. Rev. B* **61**, 3711 (2000)
- [100] F.Y. Ogrin, S.L. Lee, A.D. Hillier, A. Mitchell, and T.H. Shen, *Phys. Rev. B* **62**, 6021 (2000)
- [101] O. Bourgeois, and R. C. Dynes, *Phys. Rev. B* **65**, 144503 (2002)
- [102] L.N. Bulaevskii, V. V. Kuzii, and A. A. Sobyenin, *Pis'ma Zh. Eksp. Teor. Fiz.* **25**, 314 [*JETP Lett.* **25**, 290 (1977)]
- [103] A.I. Buzdin, L. N. Bulaevskii, and S. V. Panyukov, *Pis'ma Zh. Eksp. Teor. Fiz.* **35**, 147 [*JETP Lett.* **35**, 178 (1982)]
- [104] V.V. Ryazanov, V. A. Oboznov, A. Y. Rusanov, A. V. Veretennikov, A. A. Golubov, and J. Aarts, *Phys. Rev. Lett.* **86**, 2427 (2001)
- [105] Blum, Y., M. K. A. Tsukernik, and A. Palevski, *Phys. Rev. Lett.* **89**, 187004 (2002)
- [106] T. Kontos, M. Aprili, J. Lesueur, F. Genet, B. Stephanidis, and R. Boursier, *Phys. Rev. Lett.* **89**, 137007 (2002)
- [107] A. Bauer, J. Bentner, M. Aprili, M. L. D. Rocca, M. Reinwald, W. Wegscheider, and C. Strunk, *Phys. Rev. Lett.* **92**, 217001 (2004)
- [108] H. Sellier, C. Baraduc, F. Lefloch, and R. Calemczuk, *Phys. Rev. Lett.* **92**, 257005 (2004)



## Chapter 2

# Scanning Probe Microscopy

### 2.1 Introduction

Recently, a lot of effort has been focused on developing experimental techniques for studying vortex matter at the nanoscale. Since a collective behavior of vortex dynamics can be extracted, for example, from electronic and heat transport and magnetic measurements [1]-[10], the real challenge lies in the capability to investigate single vortex, lattice arrangements and local mechanism of motion with a high spatial resolution. An overall view on the vortex lattice, and its structural characteristics, can be provided by small-angle neutron scattering in the reciprocal space [11],[12], and by Bitter decoration [13],[14], time-resolved magneto-optic techniques [14]-[18] and holography electron microscopy [19] in real space. The first observation of isolated vortices was pioneered by Essman and Trauble in 1967 [13]. In a low magnetic fields, they used small magnetic particles to decorate the surfaces of different superconductors in order to get information on the arrangement of vortices in the vortex lattice. By using this technique, large areas hundreds of microns square of the sample surface can be investigated by taking a snapshot of the lattice. More recently, real space imaging of superconducting vortices has been obtained by using scanning probe microscopy and spectroscopy (SPM/S) techniques. Among all of them, scanning SQUID microscopy [20] and scanning Hall probe microscopy [21],[22], with a submicron spatial resolution, have been successfully used to study the geometries, dynamics and interactions of vortices in different systems. On the other hand, scanning tunneling microscopy (STM), with a subnanometric resolu-

tion, is the only technique able to image individual vortex cores by spatially mapping the amplitude of the superconducting order parameter [23]-[25]. The STM method is sensitive to the electronic properties of the sample surface and thus require clean and flat surfaces. Although it provides a unique opportunity to image vortices at high magnetic fields (due to sensitivity to the amplitude of the order parameter rather than the magnetic profiling), STM technique cannot distinguish between the polarity of the vortices. On the other hand, magnetic force microscopy (MFM) provides information about the vortex polarity and requires less stringent surface quality, albeit the method is constrained to low enough magnetic field as to distinguish the magnetic profiles of individual flux quantum [26]-[35]. Being directly sensitive to the strength and direction of the stray field, MFM provides information that is not easily available elsewhere.

## 2.2 Scanning Probe Microscopy

The Scanning Probe Microscopies allow the study of several surface properties. Depending on the used technique as well as on the intrinsic physical nature and geometry of the *probe* and the sample, a study of the sample topography, of the electric and magnetic domains distribution on the sample surface and of its electric and electromechanical properties can be carried out. For instance, the Atomic Force Microscopy (AFM) relies on the tip-sample van der Waals interaction, Electrostatic Force Microscopy (EFM) and Kelvin Probe Force Microscopy (KPFM) on the electrostatic interaction, Magnetic Force Microscopy (MFM) on the magnetostatic interaction, Scanning Tunneling Microscopy (STM) on the quantum-mechanical effect of electron tunneling through an energy barrier (tip-sample separation), to name a few of them.

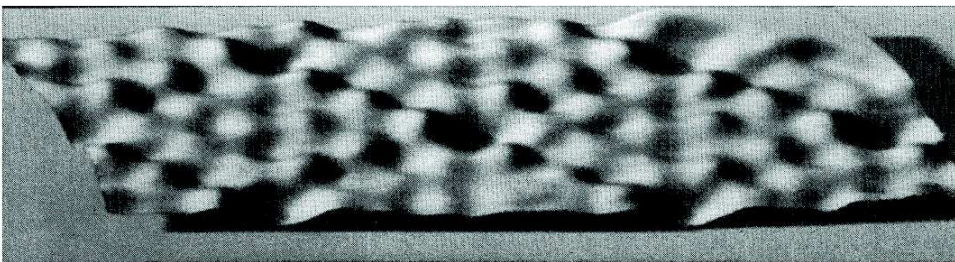


**Figure 2.1:** First STM image of atomic structure in Si(111) by Binig and Rohrer [36]

The concept of STM was first developed by Binnig and Rohrer in 1982 at IBM Zurich [36]. Few years later, in 1986, the researchers were awarded the Nobel Prize in Physics. Figure 2.1 shows the first STM image of the atomic structure of Si(111).

In the standard experimental setup of SPM measurements, either the sample or the tip is located at the end of a *piezo-scanner* (or *piezo-tube*), which deflects in  $x-y-z$  directions by applying high voltage (see fig.2.2). Four electrodes are placed on the outside of the tube, which is usually made of lead-zirconate-titanate (PZT), for  $x-y$  motion, as well as an electrode is inside the tube for  $z$  elongation/contraction. The direction of the movement is tuned by the voltage polarity. While the  $x$  and  $y$  motions are required to raster the tip on the sample surface, the piezo displacement in  $z$  direction is kept constant, when working in *open loop* or is adjusted during the scanning by a feedback circuit, set on the *interaction setpoint*, in *closed loop* mode.

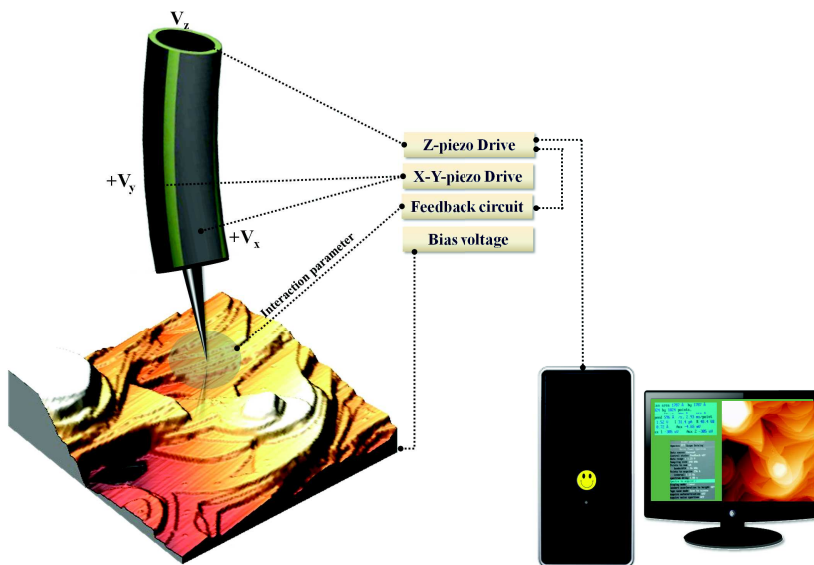


**Figure 2.2:** STM experimental setup. A sharp tip is located at the end of a piezo tube, having four electrodes all around it. Only  $+V_x$  and  $+V_y$  are visible in the picture, connected to the  $x-y$ -Piezo Drive unit. The  $z$ -Piezo Drive unit supplies high voltage to the  $z$ -piezo and can be eventually connected to the *Feedback Circuit*, when working in *closed loop mode*. The feedback loop detects the interaction parameter and adjusts the voltage on the  $z$ -piezo to keep a constant *interaction setpoint*.

The detection of the interaction parameter strongly depends on the specific technique. In STM the probe is made by an atomically sharp tip which eventually guar-

anties the interaction between a single atom at the tip apex and the atoms of the sample surface. The application of a bias voltage between tip and sample, separated by a vacuum energy barrier, brings to an experimental detectable electron tunneling current, through a tunneling current amplifier. In AFM-based techniques, the probe is made by a cantilever having a sharp tip at the end of it (with a typical curvature radius of  $1 \div 10nm$ ). In the simplest case, the tip-sample interaction causes a deflection of the cantilever, which can be detected, for instance, by an interferometric apparatus that will be described in details in session 2.3.1.

In AFM and STM, the modulation of the interaction parameter on the sample surface, van der Waals force and tunneling current respectively, is strongly dependent on the sample roughness and, in open loop, it's a direct way to image the sample topography. Differently, in closed loop, a setpoint of cantilever deflection/tunneling current for AFM/STM respectively, is chose and the feedback loop adjusts the voltage on the scanning piezo in the  $z$ -direction to keep it constant. Being the displacement versus voltage response of the piezo-tube pre-calibrated a topographic map can be created by monitoring the voltage applied to the  $z$ -piezo.

MFM and STM experiments on Superconductor/Ferromagnet heterostructures, only magnetically coupled, will be presented in this dissertation.

### 2.2.1 Magnetic Force Microscopy

In 1987 Martin and Wickramasinghe developed the idea of the Magnetic Force Microscopy, coating an AFM probe with a thin ferromagnetic layer, thus able to feel long-range interactions with magnetic samples [37]. The engineering design of the AFM probe, as well as of the AFM itself, came slightly earlier, in 1986, by Binnig, Quate and Gerber [38]. In the simplest approximation of the atomic lattice as a series of masses and springs, the spring constat of the interatomic interaction results in  $k_{at} \approx 10 \frac{N}{m}$ . As a consequence, the fabrication of a *cantilever*, with spring constant lower than  $k_{at}$ , thus deflecting because of the interatomic interaction between a sharp tip at end of it and a sample, is not easy but possible.

Standard AFM measurements can be carried out in three different modalities: *contact*, *tapping* and *non-contact*. In *contact mode*, the cantilever is deflected as a consequence of tip-sample van der Waals repulsive interaction. A feedback loop can be used to keep constant such a deflection ( $\delta$ ), pulling away the probe from the surface in presence of a

topographic mountain and pushing it down when a depression occurs, thus ensuring a constant tip-sample force, given by the Hooke law  $F_{tip-sample} = k_{cantilever}\delta$ . In *tapping mode* the cantilever is forced to oscillate by a piezo vibrator at its own resonance frequency in close proximity to the sample surface, setting up an intermittent tip-sample contact and periodically jumping from attractive to repulsive interaction regime. The interaction causes a shift of the oscillating frequency as well as a modulation of the oscillating amplitude (with respect to free frequency and amplitude). A feedback loop can be used to keep constant the amplitude, moving the probe closer or further from the surface, depending on its roughness. In *non-contact mode* the cantilever is forced to oscillate at its own resonance frequency with nanometric amplitude. When an attractive tip-sample interaction occurs a shift of the resonance frequency is detected. By keeping a fixed tip-sample separation, the modulation of such a shift while scanning is a measure of the sample topography.

The MFM in vacuum operates in non-contact regime, whereas at tip-sample separation of  $50 \div 200nm$  the non-magnetic short range interactions are completely undetected. In *static mode* the magnetic probe, magnetized along the longitudinal axis, moves at constant height with respect to the sample surface. Due to the magnetostatic interaction with the out-of-plane stray field coming out from the sample surface, the cantilever deflects toward the sample if attracted, further away if repulsed, giving rise of a map of magnetic domains.

In *oscillating mode*, also called *Frequency Modulation-MFM*, the cantilever is excited by a piezo vibrator at its own resonance frequency. Whenever a magnetic interaction occurs between out-of-plane sample stray field and tip longitudinal magnetization, frequency and amplitude of the oscillation change. Figure 2.3 sketches the frequency modulation of an oscillating cantilever due to its interaction with an out-of-plane stray field having almost a square wave shape. Attractive interaction results in a negative shift with respect to the free frequency, whereas a positive shift occurs when the interaction is repulsive. The MFM image is made by mapping the frequency modulation on the sample surface.

The cantilever frequency shift can be formally derived by writing the equation for its dynamic in presence of magnetic tip-sample interaction.

The tip-sample force for small oscillations of the cantilever around the tip-sample sep-

aration  $z_0$ , can be written as follows:

$$F_{mag} = F_{mag,z_0} + \left. \frac{\partial F_{mag}}{\partial z} \right|_{z(t)} \quad (2.1)$$

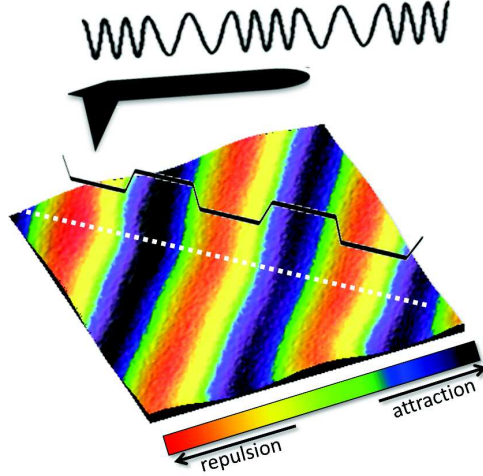


**Figure 2.3:** Sketch of FM-MFM mode. An oscillating cantilever is interacting with a square wave magnetic stray field. Attractive/repulsive interactions are mapped through the frequency shift of the cantilever oscillations and represented by color contrast.

By modelling the ferromagnetic layer of the tip as made by infinitesimally small elements of volume  $dV'$  and magnetic moments  $\vec{M}(\vec{r}')$ , each of them interacting with the stray field  $H(\vec{r} - \vec{r}')$  coming out from the position  $\vec{r}$  on the sample surface (see fig.2.4), the energy of the tip-sample interaction can be written as follows:

$$E_{mag} = - \int_{V_{layer}} \vec{M}(\vec{r}') \cdot \vec{H}(\vec{r} - \vec{r}') dV' \quad (2.2)$$

At constant tip-sample separation  $z_0$

$$\vec{F}_{mag,z_0} = -\vec{\nabla} E_{mag} = \int_{V_{layer}} \vec{\nabla}(\vec{M} \cdot \vec{H}) dV' \quad (2.3)$$

which has a  $z$  component:

$$F_{mag,z} = -\frac{\partial E_{mag}}{\partial z} = \int_{V_{layer}} (M_x \frac{\partial H_x}{\partial z} + M_y \frac{\partial H_y}{\partial z} + M_z \frac{\partial H_z}{\partial z}) dV' \quad (2.4)$$

By deriving the eq.2.4:

$$\frac{\partial F_{mag,z}}{\partial z} = \int_{V_{layer}} \left( M_x \frac{\partial^2 H_x}{\partial z^2} + M_y \frac{\partial^2 H_y}{\partial z^2} + M_z \frac{\partial^2 H_z}{\partial z^2} \right) dV' \quad (2.5)$$

which it is integrated on the entire ferromagnetic layer volume.

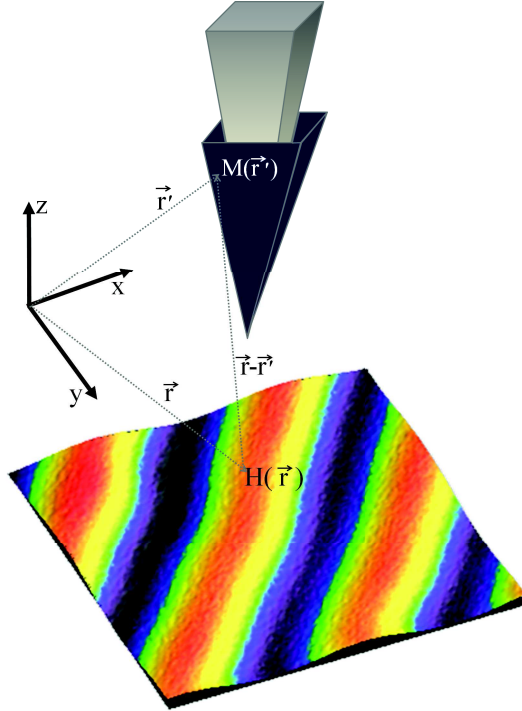


**Figure 2.4:** Model of magnetic tip-sample interaction. The ferromagnetic coating layer can be considered as made by by infinitesimally small elements of volume  $dV'$  and magnetic moments  $\vec{M}(\vec{r}')$ , each of them interacting with the stray field  $H(r - r')$  coming out from the position  $r$  on the sample surface.

By combining equations 2.4 and 2.5 in 2.1 and solving the problem of cantilever dynamic, the shift of the resonance frequency with respect to the free frequency  $f_0$  can be explicitly derived, resulting in:

$$df = \frac{f_0}{2k_{cant}} \frac{\partial F_{mag,z}}{\partial z} \quad (2.6)$$

The MFM experiments presented in this dissertation were performed in FM-MFM mode at  $T=6K$  by using a commercial Si cantilever, equipped with a magnetic tip and having a resonance frequency  $f_0 \approx 75kHz$  and elastic constant  $k \approx 2.8 \frac{N}{m}$ . The

tip, coated by a ferromagnetic Co/Cr film, is characterized by nominal low moment  $\mu < 0.3 \times 10^{-13} \text{emu}$  and measured coercivity  $H_{c,tip} = 550 \div 600 Oe$ . The magnetic imaging was done by scanning in non-contact regime and by mapping line by line the frequency shift  $df = f - f_0$  of the resonating cantilever, due to the stray field coming out from the sample. MFM maps were obtained by scanning at constant tip-sample heights, between  $60 \div 150 \text{nm}$ , and the attractive/repulsive tip-sample interaction was mapped using color contrast.

### 2.2.2 Scanning Tunneling Microscopy and Spectroscopy

Scanning tunneling microscopy (STM) relies on the quantum mechanical tunneling effect which predicts that electrons have a finite probability to tunnel through an energy barrier. In an STM experimental setup a metallic tip is brought close to a sample (conducting or semiconducting) and kept at nanometric distance from it. In these conditions, there is a non-zero probability for the electrons of the tip to traverse the vacuum barrier region in between and reach the sample, and vice versa. Once a bias voltage is applied, a net flow of electrons in one direction arises, resulting in a measurable tunneling current. Such a tunneling current is exponentially dependent on the distance between the tip and sample, which gives rise to a sub-Å resolution in the  $z$ -direction.

Inside the barrier region the electron wavefunction is a decaying exponential:

$$\Psi(z) = \Psi(0)e^{-\kappa z} \text{ and } \kappa = \frac{\sqrt{2m(\Phi - eV)}}{\hbar} \quad (2.7)$$

where  $z$  is the distance between the tip and the sample,  $\Phi$  describes the height of the barrier and is related to the workfunctions of the sample and tip, and  $eV$  is the electron energy supplied by the bias. The probability of a single electron to tunnel across the barrier is:

$$|\Psi(z)|^2 = |\Psi(0)|^2 e^{-2\kappa z} \quad (2.8)$$

and the resulting current is proportional to the tunneling probability of all the electrons in the energy region  $(E_F - eV) \div E_F$ :

$$I(z) \propto \sum_{E_n=E_F-eV}^{E_F} |\Psi_n(0)|^2 e^{-2\kappa z} \propto I(0)e^{-2\kappa z}. \quad (2.9)$$

For a typical workfunction value of around 5eV, a 1Å change in tip-sample separation can result in almost an order of magnitude change in tunneling current.

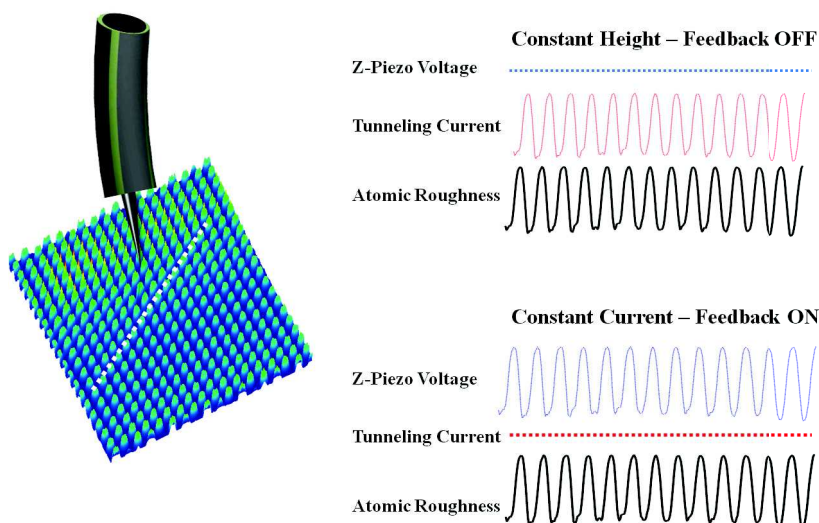


**Figure 2.5:** STM map with atomic resolution of freshly cleaved HOPG, in ambient temperature and pressure. The atomic roughness is given by modulation of the tunneling current in *constant height mode*, by modulation of the voltage on the *z*-piezo in *constant current mode*.

The two STM scanning modalities are sketched in fig.2.5, where an STM map ( $4\text{nm} \times 4\text{nm}$  in size) with atomic resolution is shown. It was acquired on freshly cleaved HOPG (Highly Oriented Pyrolytic Graphite) in ambient temperature and pressure by means of a commercial Multimode V by Bruker, and with a *PtIr* tip. In *constant height mode* the feedback is inactive during scanning. The tip is stabilized in one point above the surface, thus the atomic roughness results in modulation of the tunneling current. On the contrary, in *constant current mode* a desired value of the tunneling current is defined as the setpoint of the feedback loop. During scanning the feedback adjusts the voltage on the scanning piezo in the *z*-direction to keep the current constant, where the distance versus voltage response of the piezo material has been pre-calibrated. In this way, by monitoring the voltage applied to the *z*-piezo the topographic map can be created.

Apart from the capability of imaging morphology with very high spatial resolution and eventually making atomic resolved maps, the power of the STM relies on the possibility

of getting insight into the electronic density of states (DOS) of the investigated samples. The tunneling rate of electrons between the tip and sample is governed by Fermi's Golden Rule:

$$w = \frac{2\pi}{\hbar} |M|^2 \delta(E_\psi - E_\chi) \quad (2.10)$$

where  $\psi$  and  $\chi$  describe the individual electronic wavefunctions of tip and sample respectively, with energy  $E_\psi$  and  $E_\chi$ .

Bardeen [39] has shown that for non interacting electrodes (separate wavefunctions of the tip and sample, roughly orthogonal) and elastic tunneling, the element matrix is given by:

$$M = -\frac{\hbar^2}{2m} \int_{z=z_0} \left( \chi^* \frac{\partial \psi}{\partial z} - \psi \frac{\partial \chi^*}{\partial z} \right) dS \quad (2.11)$$

which describes the overlap of the tip and sample wavefunctions in the barrier region, being the surface of integration the entire barrier region. Following the treatment of Bardeen, the net tunneling current is the sum of the current flowing from the tip to the sample and vice versa:

$$I = I_{tip \rightarrow sample} - I_{sample \rightarrow tip} \quad (2.12)$$

$$I = \frac{4\pi e}{\hbar} \int_{-\infty}^{\infty} |M|^2 \rho_t(E_t) \rho_s(E_s) \{f(E_t)[1 - f(E_s)] - f(E_s)[1 - f(E_t)]\} dE \quad (2.13)$$

where  $e$  is the electron charge,  $\hbar$  is the reduced Planck's constant,  $M$  is the tunneling matrix element,  $\rho_{s,t}$  are respectively the density of states of the sample and tip, and  $f(E) = [1 + e^{-(E-E_f)/k_B T}]^{-1}$  is the Fermi distribution function with  $k_B$  the Boltzmann constant and  $T$  the temperature.

By applying a bias voltage  $V$  and defining  $E_t = E$  and  $E_s = E + eV$ , the equation 2.13 can be simplified to:

$$I(V) = \frac{4\pi e}{\hbar} \int_{-\infty}^{\infty} |M|^2 \rho_t(E) \rho_s(E + eV) \{f(E) - f(E + eV)\} dE \quad (2.14)$$

The tunneling current depends on the nature of the tip and sample through the tunneling matrix element, which describes the overlap of their wavefunctions in the barrier region, as well as on their local DOS. In practice,  $|M|$  is often taken out of the integral because it is considered constant at low voltage and a set tip-sample separation, even if it will change for different tip and sample combinations, different tip materials, and

even for different tips of the same material but different shape. Moreover, in the limit of small bias voltage around the Fermi energy, the density of states of the metallic tip can be considered constant and taken out of the integral. Finally, if the measurements are made at low temperature, the Fermi function are almost step functions with a cut off of  $k_B T$ , which allows to further simplify the current expression:

$$I(V) \propto \frac{4\pi e}{\hbar} |M|^2 \rho_t(0) \int_{E_F}^{E_F+eV} \rho_s(E+eV) dE \quad (2.15)$$

thus the derivative with respect to the voltage gives the *differential tunneling conductance* ( $dI/dV$ ), which is directly proportional to the electronic DOS of the sample:

$$\frac{dI}{dV} \propto \rho_s(eV) \quad (2.16)$$

The most common method to experimentally measure the  $dI/dV$  versus  $V$  is to use the *lock-in* method. By modulating the bias voltage  $V$  with a small AC voltage of known frequency ( $V_m \sin \omega t$ ) and expanding in a power series:

$$I(V + V_m \sin \omega t) = I(V) + \left. \frac{dI}{dV} \right|_V V_m \sin \omega t + \frac{1}{4} \left. \frac{d^2 I}{dV^2} \right|_V V_m^2 (1 - \cos 2\omega t) + \dots \quad (2.17)$$

it is possible to measure directly the differential conductance by acquiring the DC signal of the first harmonic of the output, which is phase locked to the known frequency. In doing this, the choice of the AC voltage magnitude is commonly limited by a lower value of  $\sim k_B T$ , which sets the thermal broadening of the measurements. However, higher AC signal might be used in order to maximize the signal to noise ratio, due to additional instrumental and electronic noises.

All differential conductance spectra presented in this dissertation were taken with the same tunneling parameters, with the junction stabilized at  $V=10$  mV and  $I=100$  pA, and with an AC modulation of  $0.2$  mV at  $T = 1.5$  K. Moreover, conductance maps can be built by acquiring the conductance value at specific energy (Fermi energy in this dissertation) while scanning the tip over the sample surface at high voltage (20 mV). Topography is always acquired simultaneously to check the location where the spectroscopic information was recorded.

## 2.3 Cryogenic Scanning Microscopes

The ultra-high vacuum (UHV) cryogenic microscopes used during this dissertation are a Scanning Force Microscope (SFM), provided by Omicron and equipped with

Scala-PRO electronics, and a USM1300  $^3\text{He}$  system, provided by Unisoku and equipped with RHK electronics, housed in *Università degli studi di Salerno* (Salerno, Italy) and *Temple University* (Philadelphia, PA, USA) respectively. Omicron-SFM and Unisoku-STM have been used to perform FM-MFM and STM experiments respectively.

### 2.3.1 Cryogenic SFM - Omicron

The low temperature SFM-Omicron, in *Università degli studi di Salerno*, is shown in fig.2.6. By loading tips and samples into the *load lock chamber* and by pumping it down to  $10^{-8}\text{Torr}$  before transferring, any contamination of *preparation chamber* and *UHV chamber* can be avoided. The latter, in particular, where the scan head is housed, is always kept at pressure as low as  $10^{-10}\text{Torr}$ . The *preparation chamber* is equipped with a single source e-beam evaporator, for *in-situ* sample deposition, a heating stage for high-temperature deposition as well as for surface cleaning of samples prepared *ex-situ*, a hydrogen gun for surface cleaning and surface hydrogenation. Transfer rods allow the move of tips/samples for one chamber to the other as well as to place them on the scan head, which is fixed at the end of a mobile rod. A motor allows the vertical movements of the rod from the UHV chamber down to the cryostat.

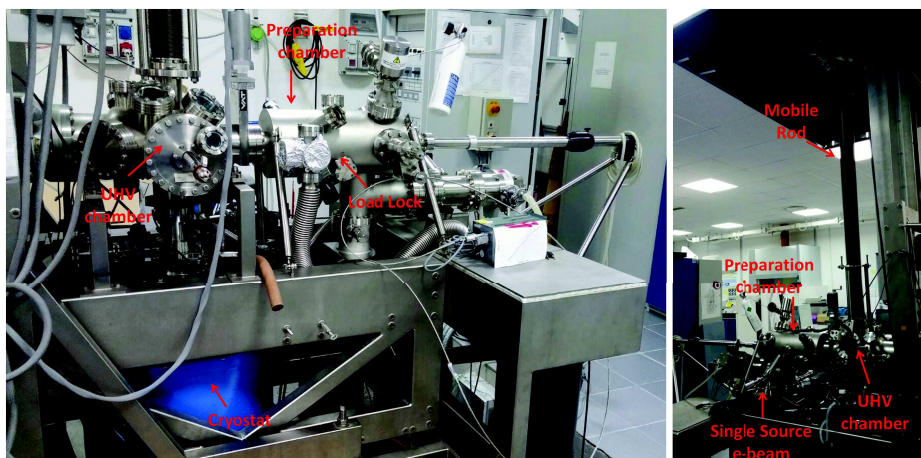


**Figure 2.6:** Low Temperature Scanning Force Microscope - Omicron

Moving from the outside, the cryostat is concentrically made by the *outer vacuum chamber* (OVC), the *liquid nitrogen tank*, the *liquid helium tank*, the *variable temper-*

ature insert (VTI) and the *inner vacuum chamber* (IVC). During the measurements, the scan head is located in the IVC, which is directly connected to the UHV chamber on the top of the cryostat.

The role of the outer vacuum chamber as well as of the nitrogen tank is to reduce the liquid helium consumption by minimizing the thermal exchange with the external environment. For the same reason additional vacuum jackets are placed between nitrogen and helium tanks as well as between helium tank and VTI.

The scan head is cooled down by the mechanical/thermal contact between the female cone of the VTI and male cone of the rod, whereas the VTI is filled by cold gas/liquid helium that flows from the helium tank through a capillary of variable impedance, software-regulated by an electromechanical *needle valve* (see fig.2.7). This configuration allows to reach a base temperature of  $4.2K$  and  $5K$  at the female cone and at the scan head respectively, due to thermal dispersion along the line. Eventually, by pumping on the VTI, temperature as low as  $2.2K$  can be reached. A heater is placed on the male cone of the rod, allowing a fine regulation of the sample temperature in the range  $5K \div 100K$ . Without filling the cryostat with liquid nitrogen/helium, room temperature measurements can be eventually performed.

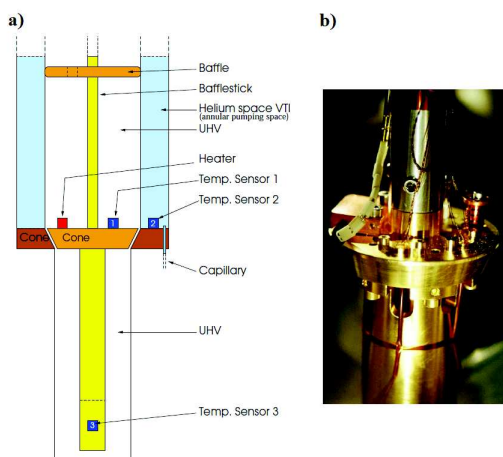


**Figure 2.7:** a) sketch of mechanical/thermal contact between VTI female cone and rod male cone. b) picture of rod male cone.

The picture of the scan head is shown in fig.2.8. The sample is glued on the sample

holder and is loaded on the top of the piezo-scanner tube, which moves in  $x - y - z$  directions during the surface scanning. The tip is mounted on a transfer plate, faced down toward the sample. An optical fiber, which is part of an interferometric unit, is used to detect the tip-sample interaction.

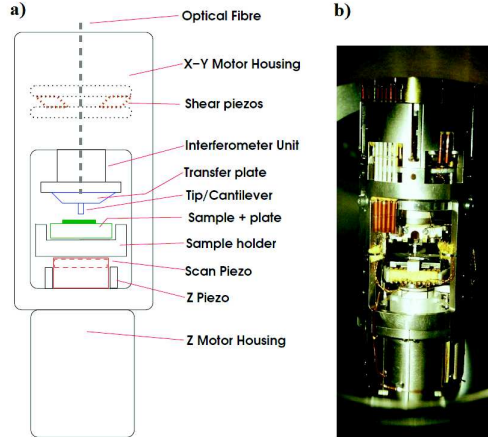


**Figure 2.8:** a) sketch of the scan head. b) real picture of the scan head.

The tip-sample approach/retract is guided by the *slip-stick* movement of  $Z$ -piezo stacks, surrounding a sapphire prism placed on the bottom of the sample holder (see fig.2.9). By quickly applying a voltage  $V_0$  to the piezo-stacks, they deform and slide against the sapphire. It is worth to notice that the voltage is applied to one piezo-stack per time, so that the others keep the sapphire prism in place. Once all of them are deformed, if the voltage is slowly ramped down to zero, the piezo-stacks go back to the equilibrium position causing a movement of the prism due to the friction between the piezoelectric elements and the prism itself. The direction of the movement is tuned by the polarity of the voltage. During the approach, this operation is performed iteratively while the tip-sample interaction is continuously recorded, until the setpoint value is reached.

The piezo-sensitivities decrease at low temperature by a factor of about 2.8 at 77K and 5.5 at 4.2K.

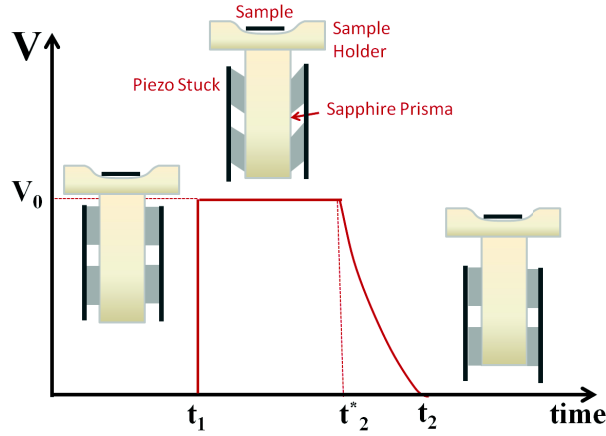


**Figure 2.9:** Working principle of piezo-stacks. A voltage  $V_0$  is applied to one piezo-stack per time, causing their deformation. Then, by slowly ramping the voltage down to zero, to all the piezo-stacks at the same time, the prism is pushed to move due to the friction between the piezoelectric elements and the prism itself.

The tip-sample interaction is detected by a *Fabry-Perot interferometer*, as shown in fig.2.10. The *Light Detector Unit* (LDU) emits a radiation with wavelength  $\lambda = 830\text{nm}$ , which runs into a 2m long optical fibre. At the end of the sharpened cut fiber, the radiation is partially transmitted and partially reflected. The transmitted component is reflected by the back of the cantilever. In such a case, the signal on the photodiode will be the interference between the two reflected components and the intensity of the signal will be a function of the fiber-cantilever distance  $d$ , as  $I = I_0 + I_1 \cos\left(\frac{2\pi}{\lambda}2d\right)$ . Finally, at the bottom of the cryostat, in the liquid helium tank, the superconducting magnet is housed, concentrically to the scan head. It is made by several km of NbTi wires, with a critical temperature  $T_c = 9.5\text{K}$ , and capable to apply axial field as high as 7T.

In order to reduce the external noise, the laboratory in which the Omicron-SFM has been installed is located on the ground floor of the Physics Department building in *Università degli Studi di Salerno*, thus to reduce the influence of the building vibration. In addition to this, the system is mounted on four pneumatic damping legs, which stand on a concrete mass. Such a mass has the role of first stage dumping of external vibrations, which are even more attenuated by lifting up the isolation legs. All pumping lines and cables are strongly fixed before reaching the system.

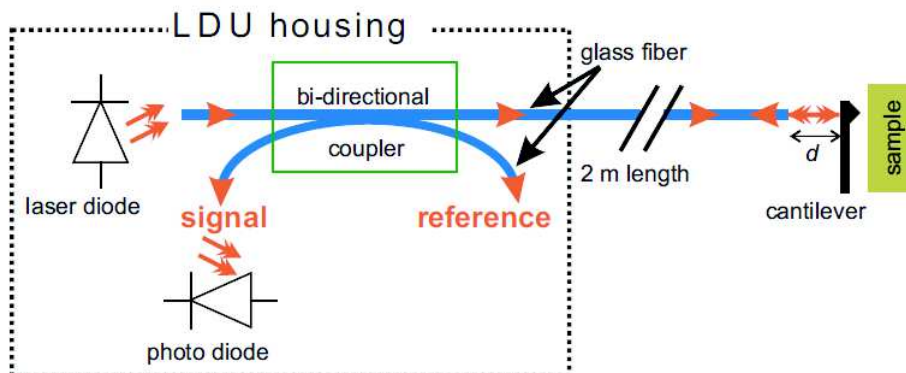


**Figure 2.10:** sketch of the interferometric apparatus for the detection of tip-sample interactions. The LDU emits a radiation with wavelength  $\lambda = 830nm$ , which runs into an optical fibre. The photodiode collects the light interference between the two reflected components of the incident radiation, due to the the end of the fiber and the back of the cantilever respectively. Their interference is a function of the relative fiber-cantilever distance.

### 2.3.2 Cryogenic STM/STS - Unisoku

The low temperature USM1300  $^3\text{He}$  system, at *Temple University*, is shown in fig.2.11. Apart from *load lock chamber*, *preparation chambers* and *UHV chamber*, many capabilities are present. A triple source e-beam evaporator is placed in the preparation chamber for *in-situ* deposition of superconducting samples, as well as a single source e-beam evaporator is housed in a second, smaller, preparation chamber, right under the load lock, for the deposition of magnetic materials. The system is also equipped with ion gun for milling, e-beam for tip shaping and preparation, low-energy electron diffraction and Auger spectrometers, liquid nitrogen cooling stage for low temperature deposition and low temperature sample cleavage stage. While the load lock is pumped down to  $10^{-8}\text{Torr}$  before transferring tips and samples, the main preparation chamber and the UHV chamber are constantly kept at pressure in the low  $10^{-11}\text{Torr}$  range. Transfer rods allow to transfer tips/samples in the system as well as to load them directly on the STM head, which is placed all the time on the bottom of the cryostat, without any optical access.

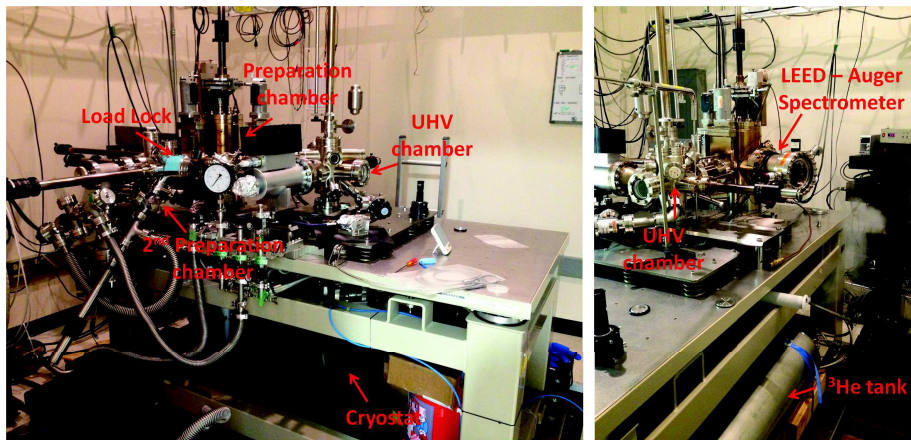


Figure 2.11: Low Temperature Scanning Tunneling Microscope - Unisoku

Moving from the outside, the cryostat is made by the *outer vacuum chamber*, the *liquid helium tank*, the *1K pot*, the  *$^3\text{He}$  pool* connected with an external  $^3\text{He}$  tank, and the *inner vacuum chamber* where, at the bottom of the cryostat, the STM head is housed. As before, the role of the vacuum jackets is to reduce thermal exchanges and minimize the liquid helium consumption.

The liquid helium flows through a capillary, encountering an impedance that is set by manually operating a *needle valve*, from the helium tank into the 1K pot, where a base temperature of  $1.5\text{K}$  can be reached by pumping on the bath. The thermal contact of the STM head with the  $^3\text{He}$  pool, made by a gold wire, and of the  $^3\text{He}$  pool with the 1K pot ensures a cooling of the sample down to  $1.5\text{K}$ . Additionally, by pumping on the  $^3\text{He}$  pool a temperature as low as  $350\text{mK}$  can be reached. Measurements at temperature higher than  $1.5\text{K}$  are still possible but they require longer time for temperature stabilization, in order to avoid thermal drift effects. Moreover, room temperature STM/STS experiments can be successfully performed.

Differently from the case of the Omicron-SFM, in USM1300  $^3\text{He}$  system, the tip is sit on the piezo-scanner, which is inside of a sapphire prism, surrounded by piezo-stucks, on the bottom of the STM head. The slip-stick mechanism that guides the tip-sample approach and retract has been already discussed in subsection 2.3.1 (see fig.2.9). The sample is faced down toward the tip.

As before, the piezo-sensitivities are affected by the temperature, decreasing by a factor of about 2.8 at  $1.5\text{K}$ .

Finally, at the bottom of the cryostat, in the liquid helium tank, the superconducting

magnet is housed, concentrically to the STM head. It is made by NbTi wires and it is capable to apply axial field as high as 9T.

In order to reduce the external vibrational noise, the laboratory in which the STM is housed has been specifically designed, with the aim of decoupling the instrument from the external environment, using as many vibration dampening stages as possible, each of them with a different resonance frequency. First of all, the system has been installed in the basement of the *Science education and Research College of Temple University*, in order to avoid building vibration. In addition to this, it is placed on a passive vibration isolation table, which stands on 40 Tonn inertial mass, decoupled from the floor by six vibration isolation legs. A raised floor, completely decoupled from the inertial mass has been built in order to walk around the system for routine operations without affecting its stability. All pumping lines and cables are damped before reaching the system. By doing this, vibrational noise lower than a picometer can be regularly achieved.

In addition to this, an RF and acoustic shielded room has been built all around the system. It consists of a Faraday cage which strongly attenuates any RF noise up to 10 GHz. In order to accomplish such a goal, care has been taken in choosing and designing special low-pass filters, capable to pass the signals from the outside electronics to the inside of the shielding room without damaging the RF and acoustic shield.

# Bibliography

- [1] U. Hartmann, *Adv. Electron. Electron Phys.* **47**, 49 (1994)
- [2] J.J. Krebs, B.T. Jonker, and G.A. Prinz, *J. Appl. Phys.* **61**, 3744 (1987)
- [3] A. Berger and M.R. Pufall, *Appl. Phys. Lett.* **71**, 965 (1997)
- [4] L. Louail, K. Ounadjela, and R. Stamps, *J. Magn. Magn. Mater.* **167**, L189 (1997)
- [5] W.S. Kim, W. Andra, and W. Kleeman, *Phys. Rev. B* **58**, 6346 (1998)
- [6] A. Berger and M.R. Pufall, *J. Appl. Phys.* **85**, 4583 (1999)
- [7] K. Ha and R.C. O’Handley, *J. Appl. Phys.* **87**, 5944 (2000)
- [8] G. Grimaldi, A. Leo, A. Nigro, S. Pace, and R. P. Huebener, *Phys. Rev. B* **80**, 144521 (2009)
- [9] G. Grimaldi, A. Leo, A. Nigro, A. V. Silhanek, N. Verellen, V. V. Moshchalkov, M.V. Milosevic, A. Casaburi, R. Cristiano, and S. Pace, *Appl. Phys. Lett.* **100**, 202601 (2012)
- [10] G. Grimaldi, A. Leo, P. Sabatino, G. Carapella, A. Nigro, S. Pace, V. V. Moshchalkov, and A. V. Silhanek, *Phys. Rev. B* **92**, 024513 (2015)
- [11] M. R. Eskildsen, *Front. Phys.* **6(4)**, 398 (2011)
- [12] M.R. Eskildsen, E.M. Forgan, H. Kawano-Furukawa, *Rep. Prog. Phys.* **74**, 124504 (2011)
- [13] U. Essmann and H. Trauble, *Phys. Lett.* **24**, 526 (1967)

- [14] L.Y. Vinnikov, J. Karpinski, S.M. Kazakov, J. Jun, J. Anderegg, S.L. Bud'ko, P.C. Canfield, *Phys. Rev. B* **67**, 092512 (2003)
- [15] M. Terao, Y. Tokunaga, M. Tokunaga, T. Tamegai, *Physica C* **426**, 94 (2005)
- [16] P.E. Goa, H. Hauglin, A.A.F. Olsen, M. Basiljevic, T.H. Johansen, *Rev. Sci. Instrum.* **74**, 141 (2003)
- [17] P.E. Goa, H. Hauglin, M. Basiljevic, E. Il'yashenko, P.L. Gammel, T.H. Johansen, *Supercond. Sci. Technol.* **14**, 729 (2001)
- [18] M. Tokunaga, M. Kobayashi, Y. Tokunaga, T. Tamegai, *Phys. Rev. B* **66**, 060507(R) (2002)
- [19] A. Tonomura, *J. Supercond.* **7**, 2 (1994)
- [20] L.N. Vu, M.S. Wistrom, D.J. Van Harlingen, *Appl. Phys. Lett.* **63**, 1693 (1993)
- [21] A.M. Chang, H.D. Hallen, H.F. Hess, H.L. Kao, J. Kwo, A. Sudbo, T.Y. Chang, *Europhys. Lett.* **20(7)**, 645 (1992)
- [22] T. Nishio, Q. Chen, W. Gillijns, K. De Keyeser, K. Vervaeke, V.V. Moshchalkov, *Phys. Rev. B* **77**, 012502 (2008)
- [23] A. Kohen, T. Cren, T. Proslie, Y. Noat, W. Sacks, D. Roditchev, F. Giubileo, F. Bobba, A.M. Cucolo, N. Zhigadlo, S.M. Kazakov, J. Karpinski, *Appl. Phys. Lett.* **86**, 212503 (2005)
- [24] G. Karapetrov, J. Fedor, M. Iavarone, M. T. Marshall, and R. Divan, *Appl. Phys. Lett.* **87**, 162515 (2005)
- [25] H. Suderow, I. Guillamón, J.G. Rodrigo, and S. Vieira, *Supercond. Sci. Technol.* **27**, 063001 (2014)
- [26] T. Shapoval, V. Metlushko, M. Wolf, V. Neu, B. Holzapfel, L. Schultz, *Physica C* **470**, 867 (2010)
- [27] T. Shapoval, V. Metlushko, M. Wolf, B. Holzapfel, V. Neu, and L. Schultz, *Phys. Rev. B* **81**, 092505 (2010)
- [28] M. Iavarone, A. Scarfato, F. Bobba, M. Longobardi, G. Karapetrov, V. Novosad, V. Yefremenko, F. Giubileo, and A. M. Cucolo, *Phys. Rev B* **84**, 024506 (2011)

- [29] M. Iavarone, A. Scarfato, F. Bobba, M. Longobardi, S. A. Moore, G. Karapetrov, V. Yefremenko, V. Novosad, and A. M. Cucolo, *IEEE Trans. Magn.* **48**, 3275 (2012)
- [30] A. M. Cucolo, A. Scarfato, M. Iavarone, M. Longobardi, F. Bobba, G. Karapetrov, V. Novosad, and V. Yefremenko, *J. Supercond. Nov. Magn.* **25**, 2167 (2012)
- [31] F. Bobba, C. Di Giorgio, A. Scarfato, M. Longobardi, M. Iavarone, S. A. Moore, G. Karapetrov, V. Novosad, V. Yefremenko, and A. M. Cucolo, *Phys. Rev. B* **89**, 214502 (2014)
- [32] A.P. Volodin, and M.V. Marchevsky, *Ultramicroscopy* **42**, 757 (1992)
- [33] A. Volodin, K. Temst, C. Van Haesendonck, and Y. Bruynseraede, *Appl. Phys. Lett.* **73**, 8 (1998)
- [34] E. W. J. Straver, J. E. Hoffman, O. M. Auslaender, D. Rugar, and Kathryn A. Moler, *Appl. Phys. Lett.* **93**, 172514 (2008)
- [35] O. M. Auslaender, L. Luan, E. W. J. Straver, J. E. Hoffman, N. C. Koshnick, E. Zeldov, D. A. Bonn, R. Liang, W. N. Hardy, and K. A. Moler, *Nature Physics* **5**, 35 (2009)
- [36] G. Binnig and H. Rohrer, *Rev. Mod. Phys.* **59**, 3 (1987)
- [37] Y. Martin and K. Wickramasinghe, *Appl. Phys. Lett.* **50**, 1455 (1987)
- [38] G. Binnig, C.F. Quate, and Ch. Gerber, *Phys. Rev. Lett.* **56**, 9 (1986)
- [39] J. Bardeen, *Phys. Rev. Lett.* **6**, 57 (1961)



# Chapter 3

## Vortex nucleation and dynamics in Nb/Py hybrids

### 3.1 Introduction

The study of the vortex matter at the nanoscale has recently caught a lot of attention due to its applicability in many systems. Superconducting vortices are a well known and established class of vortices, each of them carrying a single flux quantum and spontaneously arranging in a regular lattice inside the superconductor. At the nanoscale, they can be experimentally investigated by using scanning probe microscopy techniques, such as magnetic force microscopy (MFM), at low temperature and in external magnetic field. On the other hand, the progress of the deposition techniques together with the lithography technologies allows the fabrication of Superconductor/Ferromagnet (S/F) multilayers only magnetically coupled, where the response of superconducting vortices to the nano-variation in size and geometry of S and F layers can be studied. In fact, by controlling the S and F thickness, the formation of spontaneous vortex-antivortex pairs (V-AV), their confinement and mobility can be tuned.

In the following, MFM experiments on nucleation and dynamics at the nanoscale of superconducting vortices in magnetically coupled S/F heterostructures made by Nb/Py will be discussed. Nb thin films exhibit type-II superconductivity whereas Py is a ferromagnet presenting peculiar stripe-like magnetic domains due to an alternating

out-of-plane component of the magnetization.

Two different theoretical models dealing with the two opposite limits of superconductor film thickness greater [1] and smaller [2] than the penetration depth,  $\frac{d_s}{\lambda} > 1$  and  $\frac{d_s}{\lambda} < 1$  respectively, will be compared with MFM results. In Chapter 1, section 1.3.3, the critical magnetization values required for spontaneous vortex nucleation were deduced in the framework of S/F bilayers in which the ferromagnet exhibits alternating up-and-down out-of-plane magnetization vectors. In agreement with such models, in magnetically coupled Nb/Py systems the vortex formation is due to the out-of-plane components of Py magnetization  $\pm M_0$ . Hereinafter, we will define V or AV as the quantum fluxes formed on the top of  $-M_0$  or  $+M_0$  domains, respectively. In the limit of  $\frac{w}{\lambda} > 1$  and  $\frac{d_s}{\lambda} > 1$ , the model of Laiho et al. has been taken into account [1]. The threshold magnetization values required to nucleate the first pair of spontaneous straight vortices  $M_{cs}$ , which pierces through the superconducting film, or the first vortex semiloop  $M_{cl}$ , which is bent within the superconducting film, result in  $M_{cs} = 0.2 \frac{d_s}{w} H_{c1}$  and  $M_{cl} = \frac{H_{c1}}{8 \ln\left(\frac{4w}{\pi\lambda}\right)}$  respectively. If  $M_{cl} > M_{cs}$ , the formation of straight vortices is energetically favorable, and vice versa. On the other hand, in the opposite limit of  $\frac{w}{\lambda} > 1$  and  $\frac{d_s}{\lambda} < 1$ , the model of Genkin et al. has to be taken into account [2], where the threshold magnetization for spontaneous straight vortex nucleation results in  $M_c = \frac{\lambda_{eff}}{4\pi w} H_{c1}$ , with  $\lambda_{eff}(T) = \lambda(T) \coth\left(\frac{d_s}{\lambda(T)}\right)$  [3]. Spontaneous vortex formation will thus be energetically regulated by the threshold condition  $M_0 > M_c$ .

Close to the superconducting critical temperature  $T_s$ , the superconducting lower critical field is almost zero, giving  $M_{c(s,l)}(T_s) \approx 0$ , so that the critical magnetizations for the nucleation of spontaneous vortices are lower than  $M_0$ . As a consequence, at  $T \sim T_s$ , the threshold condition is always satisfied and spontaneous vortices might be formed in the Nb layer. By further decreasing the temperature,  $H_{c1}(T)$  increases with a corresponding increase in  $M_{c(s,l)}(T)$ . For this reason, at some point  $M_0 < M_{c(s,l)}$  can occur and vortices can move out from the superconducting layer. In particular, vortices escape from the S layer when  $M_0 < M_{c(s,l)}$  and  $U_{SV} < U_{BL}$ , i.e. the energy required to pin a vortex  $U_{SV} = \frac{1}{4\pi} H_{c1} \Phi_0 d_s$  is much lower than the Bean-Livingstone barrier  $U_{BL} = \frac{\pi+2}{4\pi} H_{c1} \Phi_0 \lambda$  [4].

The following experimental results indicate that, in the given Nb/Py system, vortex nucleation and confinement is regulated only by the intensity of the out-of-plane component of the magnetization with respect to the threshold value set by the thickness

of both the S and F layers. Additionally, the external magnetic field allowed the investigation of in-field vortex nucleation, V-AV unbalancing and vortex motion. A field cooling process was used to probe the change in V-AV population number whereas the sweep of the magnetic field below the superconducting critical temperature was used to force vortices into motion, resulting either in high mobility or in high rigidity followed by vortex avalanche events depending on the threshold condition regime.

## 3.2 Sample Fabrication and Preliminary Characterizations

Nb/SiO<sub>2</sub>/Py heterostructures with 1μm, and 2μm of Py layers and Nb thickness in the range 50÷360 nm were fabricated in Argonne National Laboratory (Chicago, IL (USA)) by Dr. V. Novosad, Dr. V. Yefremenko and Dr. S.A. Moore. In order to electronically decouple the F and S layers and suppress the proximity effect [5], a 10 nm thin insulating SiO<sub>2</sub> layer was placed between them. Py films were deposited by dc sputtering from a Ni<sub>80</sub>Fe<sub>20</sub> target onto a Si substrate at a base pressure of  $1.5 \times 10^{-7} Torr$ , followed by a 10nm SiO<sub>2</sub> layer. The Nb films were deposited by dc sputtering at room temperature in a dedicated system with a base pressure of  $2 \times 10^{-8} Torr$ . Those were characterized by both transport and magnetic measurements, showing a superconducting critical temperature of  $T_s = (8.8 \pm 0.1)K$ . From transport measurements [6] and by using the dirty limit expression as derived by Gor'kov [7, 8],  $\xi(0K) = 12nm$  and  $\lambda(0K) = 61nm$  were inferred. As a consequence, the superconducting lower critical field was calculated to be  $H_{c1}(0K) = 720G$ . At the MFM measurement temperature of 6K,  $\xi(6K) = \xi(0K)\sqrt{\frac{T_s}{T-T_s}} \approx 21nm$ ,  $\lambda(6K) = \frac{\lambda(0K)}{\sqrt{1-(\frac{T}{T_s})^2}} \approx 68nm$  and  $H_{c1}(6K) = \frac{\Phi_0}{4\pi\lambda(6K)^2} \ln\left(\frac{\lambda(6K)}{\xi(6K)}\right) = 418G$  have been derived.

Py is a ferromagnetic material where competing magnetic energies (magnetostatic, exchange, magneto-elastic, domain wall and anisotropy) determine the domain configurations. In thin films, periodic stripe-like domains occur above a critical thickness of  $t_c = 2\pi\frac{A}{K_u}$  [9], where  $A$  is the exchange constant and  $K_u$  is the perpendicular anisotropy constant [10, 11].  $K_u$  and consequently the critical thickness  $t_c$  can be strongly affected by the deposition parameters [?]. In the studied Py films, by considering the typical value  $A = 1 \times 10^{-6} \frac{erg}{cm}$ ,  $t_c = 100 \div 300nm$  is calculated. Stripe domains appear as a consequence of a slight magnetization canting with respect to the overall in-plane

orientation. The small out-of-plane components ( $\pm M_0$ ) point alternatively in upward and downward directions across adjacent stripes. The width  $w$  of the stripes can be controlled by the Py thickness  $d_m$  following the phenomenological relation  $w = \alpha\sqrt{d_m}$  [10, 11].

Typical magnetic hysteresis loops of Py  $1\mu\text{m}$  and Py  $2\mu\text{m}$ , in perpendicular (3.1a-b) and parallel (3.1c-d) configurations, are reported in 3.1. By measuring the saturation fields  $H_{s\parallel} = 130 \div 160\text{Oe}$  and  $H_{s\perp} = 11 \div 12\text{kOe}$ , the saturating magnetization  $M_s$  as well as the uniaxial anisotropy constant  $K_u$  can be estimated, resulting in  $M_s = \frac{H_{s\perp} + H_{s\parallel}}{4\pi} \approx 900\text{G}$  and  $K_u = \frac{M_s H_{s\parallel}}{2} \approx 6.3 \times 10^4$ . The comparison between parallel and perpendicular saturation field values confirms the presence of an easy magnetization axis mainly oriented in the film's plane whereas the ratio  $\frac{K_u}{K_d} \ll 1$  (here  $K_d = 2\pi M_s^2$  is the stray field energy density) indicates a weak perpendicular anisotropy.

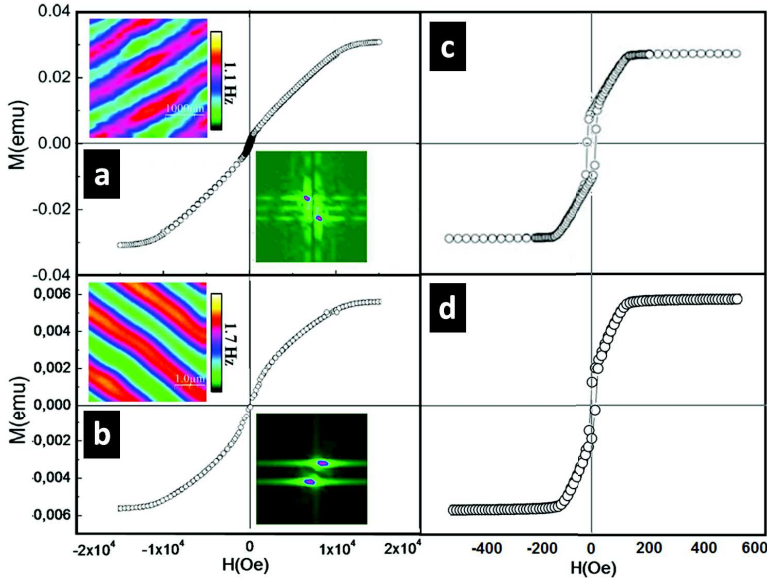


**Figure 3.1:** a) Magnetic hysteresis loop of  $1\mu\text{-Py}$  in perpendicular applied magnetic field. Top left corner: MFM map of Nb(100nm)/Py( $1\mu\text{m}$ ) at  $T=12\text{K}$  and tip-Py separation of  $h=140\text{nm}$ . Bottom right corner: FFT of the MFM map. b) Magnetic hysteresis loop of  $2\mu\text{mPy}$  in parallel applied magnetic field. Top corner: MFM map of Nb(200nm)/Py( $2\mu\text{m}$ ) at  $T=12\text{K}$  and  $h=180\text{nm}$ . Bottom right corner: FFT of the MFM map. c)-d) Magnetic hysteresis loop of  $1\mu\text{m-}$  and  $2\mu\text{m-Py}$  in parallel applied magnetic field

The MFM maps shown in the insets to fig. 3.1a-b, respectively on Nb/Py( $1\mu\text{m}$ ) and

Nb[nm]	Py[ $\mu\text{m}$ ]	$w[\text{nm}] + \Delta w$	$\frac{w}{\lambda}$	$\frac{d_s}{\lambda}$	$M_{cs}(6K)$	$M_{cl}(6K)$	$M_c(6K)$
50	1.0	$490 \pm 2\%$	7	0.74	–	–	15.9
100				1.5	15.1	32.6	–
150				2.2	24.9	33.9	–
200				2.9	33.9	34.2	–
360				5.3	61.5	34.3	–
120	2.0	$790 \pm 4\%$	12	1.8	11.9	26.1	–
200				2.9	21.1	25.2	–

**Table 3.1:** The characteristic parameters of the measured Nb/Py bilayers and the respective critical magnetization values at  $T = 6K$  are shown. By increasing the Py thickness, the stripe width also increases following a square root dependence. Note that  $M_{cs}$  is always lower than  $M_{cl}$  except in the Nb(360nm)/Py(1 $\mu\text{m}$ ) sample

Nb/Py(2 $\mu\text{m}$ ) samples, are taken at  $T=12K$  and relative separation of the tip from the Py surface of 140nm and 380nm. Before the MFM experiments were performed, the magnetic stripes were oriented along the preferred direction by applying an in-plane external magnetic field greater than  $H_{s\parallel}$ . Frequency spans of 1.1Hz in Nb/Py(1 $\mu\text{m}$ ) and 1.7Hz in Nb/Py(2 $\mu\text{m}$ ), even though the tip-Py(2 $\mu\text{m}$ ) separation is higher, indicate that the magnetic signal coming out from the 2 $\mu\text{m}$ -Py sample surface is definitely stronger than the one from 1 $\mu\text{m}$ -layer. In addition to this, in the 2 $\mu\text{m}$  ferromagnetic layer, not only the stripe conformation is much more straight and regular, but also the magnetic roughness along the single stripe is significantly lower, as measured by a frequency shift of around 0.16 Hz in 2 $\mu\text{m}$ -Py and 0.4 Hz in 1 $\mu\text{m}$ -Py layer. From the Fast Fourier Transform (FFT) analysis of the MFM maps, acquired in different areas of the sample surface, an average stripe width respectively of  $490\text{nm} \pm 2\%$  and  $790\text{nm} \pm 4\%$  can be inferred, confirming the theoretical expectation  $w = \alpha\sqrt{d_m}$  [10, 11].

In order to quantitatively compare the MFM results with the theoretical threshold conditions for vortex nucleation, the thickness  $d_s$  of the Nb films and the magnetic domain width  $w$  were experimentally measured by tuning the thin film deposition rate and time, and by a statistical analysis of the MFM maps by FFT. Moreover, the knowledge of  $\xi(6K)$  and  $\lambda(6K)$  derived from transport and magnetic measurements allows the estimate of  $H_{cl}(6K)$ .

In table3.1 the thickness of the superconducting films and the magnetic domain width

are compared to the magnetic size of the vortex as well as the strength of the critical magnetizations is derived. For all the analyzed hybrids, the ratio  $\frac{w}{\lambda}$  is greater than 1. On the other hand, Nb(50nm)/Py(1 $\mu$ m) sample, being within the limit  $\frac{d_s}{\lambda} < 1$ , satisfies the conditions of model [2], whereas all other samples are in agreement with model [1], having  $\frac{d_s}{\lambda} > 1$ . From table 3.1, one can note that the formation of spontaneous straight vortices, at the measurement temperature of  $T = 6K$ , is energetically favored in most cases, since it results  $M_{cs}(6K) < M_{cl}(6K)$ . Only in the case of Nb(360nm)/Py(1 $\mu$ m) sample the semi-loop vortices are expected.

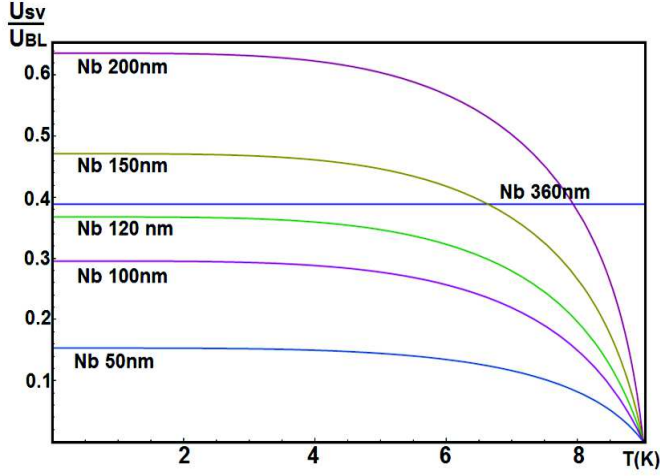


Figure 3.2: Temperature-dependence of the ratio in the studied Nb/Py

As introduced in section 3.1, once vortices are formed at  $T \approx T_s$ , they will stay in the superconducting layer if the intensity of the out-of-plane components  $M_0$  of the Py magnetization is enough to sustain them (i.e. the temperature-dependent threshold conditions are satisfied). If under-threshold, they can still be confined in the superconductor whenever the energy of the single vortex  $U_{sv}$  is higher than the energy of the Bean-Livingston Barrier  $U_{BL}$ , so that the escape condition is not satisfied. In fig.3.2, the plot of the ratio  $\frac{U_{sv}}{U_{BL}}$  as a function of the temperature for all of our samples is reported. Being  $\frac{U_{sv}}{U_{BL}} < 1$  always respected, spontaneous V-AV occurrences will be only regulated by the  $M_0$  value, thus ruling out Bean-Livingston confinement.

In particular, by comparing the calculated values of the critical magnetizations of 15.9G for Nb(50nm)/Py(1 $\mu$ m) and 15.1G for Nb(100nm)/Py(1 $\mu$ m), with the measured value

$M_0 = 16G$  [6], [14], [15], we expect a spontaneous formation of V-AV in both samples, even though the threshold values are very close to the measured  $M_0$ .

### 3.3 Superconducting Vortex Nucleation

In fig.3.3a-b the MFM images of Nb(100nm)/Py(1 $\mu$ m) and Nb(50nm)/Py(1 $\mu$ m), below the superconducting critical temperature, are shown. As expected, the Nb(100nm)/Py(1 $\mu$ m) bilayer (3.3a) forms spontaneous vortices and antivortices in the center of the oppositely polarized stripes, with a vortex polarity collinear with the magnetization of the underlying stripe domain [13]. In a scan area of  $3.8\mu\text{m} \times 3.8\mu\text{m}$  a low density of vortices, with unequal number of vortices and antivortices, with "up" polarity vortices dominating, is observed. To gain further insight into the imbalanced vortex - antivortex phenomenon, FC measurements in both positive and negative magnetic fields were performed. Depending on the magnetic field present during cooling, a change in the relative density of vortices and antivortices is expected to occur as a consequence of the compensation or enhancement of the local magnetization  $M_0$  by the applied magnetic field. Figure 3.3c shows an MFM image acquired after a FC in  $H=+6G$ . Antivortices appear above the proper stripes whereas no vortices are present above oppositely polarized magnetic stripes. On the other hand, the map acquired after a FC in higher negative field  $H=-27G$  (fig. 3.3d) still shows the presence of both V and AV, even though the density of vortices with the same polarity as the external applied field becomes higher.

No clear evidence of spontaneous V-AV formation was shown by the Nb(50nm)/Py(1 $\mu$ m) sample but instabilities or jumps in the MFM image (marked with arrows in fig. 3.3b), and high contrast modulation along the stripes were measured. These jumps, which always appear in the direction of the fast-scan axis, are due to the interaction of a magnetic object (eventually a vortex) with the magnetic tip itself. Jumps due to the vortex motion are also visible in 3.3c-d and their geometrical confinement inside the stripes proves the role of the Py out-of-plane component as a strong magnetic pinning source acting against the possibility for vortices to move perpendicularly to the stripe domains, by crossing the domain wall barrier.

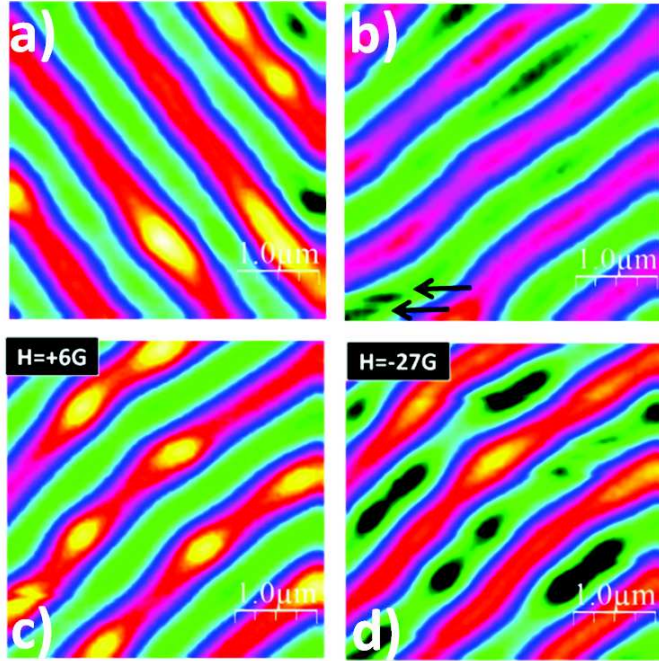


**Figure 3.3:** MFM maps in zero field cooling of a) Nb(100nm)/Py(1 $\mu$ m),  $T = 6K$ ,  $h = 130nm$ ; b) Nb(50nm)/Py(1 $\mu$ m),  $T = 6K$ ,  $h = 200nm$ . MFM of Nb(100nm)/Py(1 $\mu$ m) at  $T = 6K$  and  $h = 180nm$  field cooled in c)  $H = +6G$ , d)  $H = -27G$

The behavior below the superconducting critical temperature of samples with thicker superconducting layers, Nb(360nm)/Py(1 $\mu$ m), Nb(200nm)/Py(1 $\mu$ m) and Nb(150nm)/Py(1 $\mu$ m) is presented in fig. 3.4 [13]. The Nb diamagnetism causes the attenuation of the stripe contrast as the thickness of the superconducting layer grows up. Keeping the tip-sample separation fixed at  $h = 110nm$  above the Nb surface, a low magnetic contrast is observed in the thickest sample (Nb 360nm - fig. 3.4a), where the magnetic template is almost completely shielded. On the contrary, magnetic stripes appear visible whenever the Nb thickness is at or below 150nm (fig. 3.4c). Clearly, a more efficient screening of the Py out-of-plane magnetization component occurs in the thickest superconducting layer. In Nb(200nm)/Py, fig. 3.4b, the tip-sample separation has been reduced down to  $h = 60nm$  in order to gain sensitivity.

All attempts to unveil spontaneous V-AV in Nb(360-200-150nm)/Py(1 $\mu$ m) failed, thus confirming the agreement between the theoretical model [1], which predicts  $M_{cs} = 61.5G, 33.9G, 24.9G$  respectively, and the measured value  $M_0 = 16G$ , estimated from

the transport measurements.

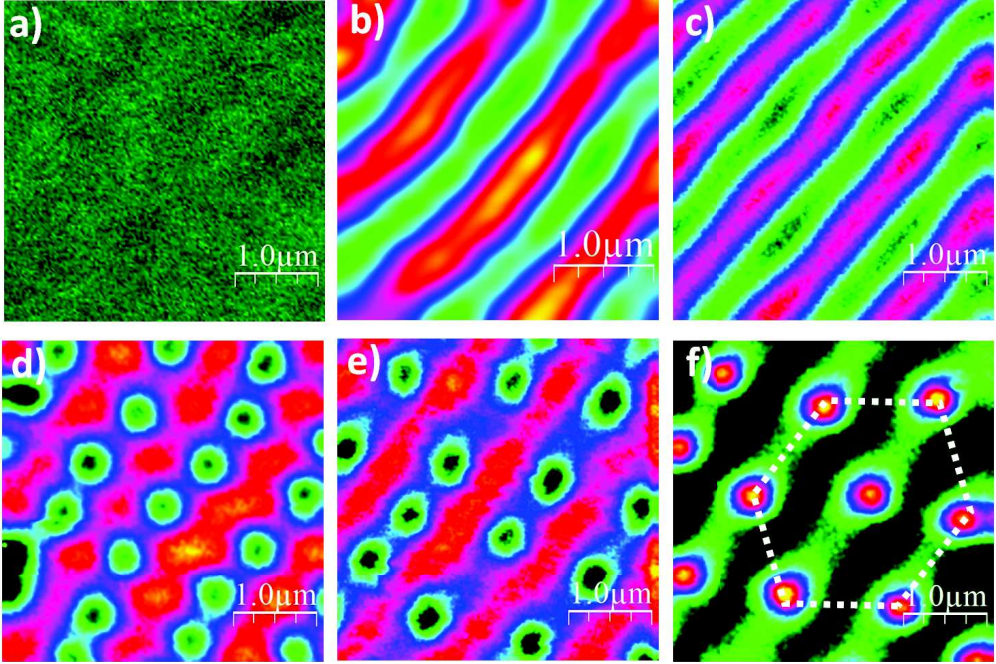


**Figure 3.4:** MFM maps in zero field cooling of a) Nb(360nm)/Py(1 $\mu$ m),  $T=6K$ ,  $h=110nm$ ; b) Nb(200nm)/Py(1 $\mu$ m),  $T=6K$ ,  $h=60nm$ ; Nb(150nm)/Py(1 $\mu$ m),  $T=6K$ ,  $h=110nm$ . MFM maps of d) Nb(360nm)/Py(1 $\mu$ m), e) Nb(200nm)/Py(1 $\mu$ m) and f) Nb(150nm)/Py(1 $\mu$ m) field cooled respectively in  $H = -16G$ ,  $H = -11.5G$ ,  $H = +10G$

Since the stray field from 1 $\mu$ mPy film was not sufficient by itself to induce vortices, these Nb/Py samples were cooled down in an out-of-plane external applied magnetic field. In fig. 3.4d-e-f, the three MFM maps acquired at  $T = 6K$  for Nb(360nm)/Py(1 $\mu$ m), Nb(200nm)/Py(1 $\mu$ m) and Nb(150nm)/Py(1 $\mu$ m), field cooled in  $H = -16G$ ,  $H = -11.5G$  and  $H = +10G$  respectively, are reported. As expected, only the vortices parallel to the external field direction are created. In fig. 3.7f, the intensity of the field was tuned in order to get a vortex-vortex distance matching the formation of a triangular (or hexagonal) vortex lattice, provided the stripe confinement.

The formation of spontaneous V-AV pairs in samples with thicker Py layer was demonstrated in Nb(200nm)/Py(2 $\mu$ m) (3.5a) and Nb(120nm)/Py(2 $\mu$ m) (fig. 3.5b). The experimental evidence of spontaneous V-AV

nucleation and its comparison with the model [1], to which these samples within the limit  $\frac{d_s}{\lambda} > 1$  refer, allow to infer the lower limit of the  $2\mu\text{m}$ -Py out-of-plane component value, resulting in  $|M_{0-Py2\mu m}| > 21.1G$ . In these samples the vortex density along the stripes is high and almost uniform as well as there is a tendency for spontaneous vortices and antivortices to be paired with each other. We correlate these experimental results to the stronger magnetic template, together with wider magnetic stripe domains, and to the thickest superconducting layer. As compared to the  $1\mu\text{m}$ -Py layers, the stripe conformation in the  $2\mu\text{m}$ -Py samples is more straight and regular, the magnetic signal coming out from the surface is stronger and the magnetic roughness along the single stripe is smaller, thus highlighting a much more uniform canting of the ferromagnet's magnetization. The frequency signal of the vortex compared to the stripe's magnetic background is  $0.97\text{mHz}$  in  $\text{Nb}(200\text{nm})/\text{Py}(2\mu\text{m})$ ,  $0.3\text{mHz}$  in  $\text{Nb}(120\text{nm})/\text{Py}(2\mu\text{m})$  and  $0.4\text{mHz}$  in  $\text{Nb}(100\text{nm})/\text{Py}(1\mu\text{m})$ , indicating that, as expected, superconducting leaks occur in the thinnest samples. We speculate that the decoupling of V-AV pairs in  $\text{Nb}(100\text{nm})/\text{Py}(1\mu\text{m})$  may be affected by the tendency of the magnetic field lines coming out from a vortex to close inside the leak, instead of the paired antivortex, as well as by the presence of smaller magnetic stripe domains so that any inhomogeneity in the stripe width induces very inhomogeneous vortex density.

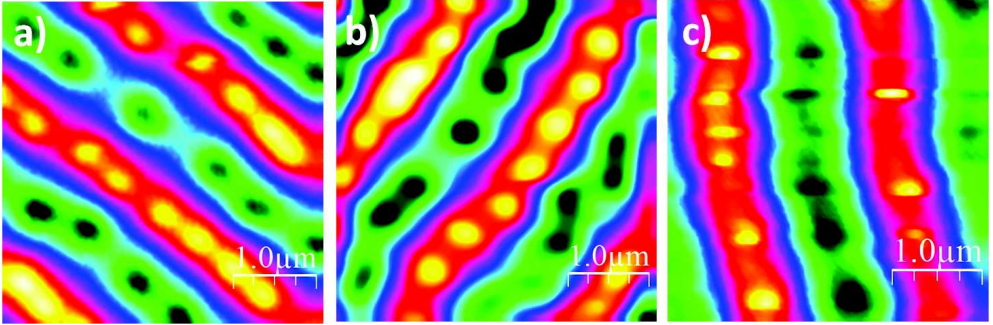


**Figure 3.5:** MFM maps in zero field cooling of a)  $\text{Nb}(200\text{nm})/\text{Py}(2\mu\text{m})$ ,  $T=6\text{K}$ ,  $h=180\text{nm}$ ; b)  $\text{Nb}(120\text{nm})/\text{Py}(2\mu\text{m})$ ,  $T=6\text{K}$ ,  $h=180\text{nm}$ . The MFM map of  $\text{Nb}(200\text{nm})/\text{Py}(2\mu\text{m})$  field cooled in  $H = +60G$ ,  $h=150\text{nm}$  is shown in (c)

Finally, in fig. 3.5c, the low temperature MFM map of  $\text{Nb}(200\text{nm})/\text{Py}(2\mu\text{m})$  after a field cooling in  $H = -60G$  is shown. The strength of the field is not enough to completely compensate the  $+M_0$  magnetic domain and, as a

consequence, both the families of quantum fluxes are still in the sample. A very high vortex mobility can be inferred from the frequent "vortex jumps" facilitated by the scanning with a magnetic tip.

### 3.4 Superconducting Vortex Dynamics

In fig. 3.6, the comparison between vortex motion in Nb(360nm)/Py(1 $\mu$ m) and Nb(200nm)/Py(2 $\mu$ m) under the sweeping of the magnetic field is reported. Figure 3.6a-b-c-d shows the behavior of vortices in Nb(360nm)/Py(1 $\mu$ m), after a field cooling of the sample in  $H = -21G$  and by sweeping the field up to positive values. After an initial phase, where the vortex configuration appeared rigid, few vortices start moving and, at  $H = +80G$  (fig.3.6a), a non-uniform spatial distribution of the vortex density takes place. As a consequence of jamming events, influenced either by the intrinsic pinning or by inhomogeneities in the magnetic template, anomalous accumulations of vortices can occur. By further increasing the external field pressure, a switching event happens at  $H = +122Oe$ , captured in fig.3.6b, and an antivortex avalanche enters during the external magnetic field sweep. The regular vortex pattern present in the lower half of fig.3.6b, recorded before the avalanche entered, is suddenly destroyed and a disordered flux distribution sets up in the upper half of the image 3.6b. From this point, by keeping the field constant, the vortex arrangement appears not to match the Py stripe pattern anymore (fig.3.6c). Such a disordered distribution of antivortices (with respect to the underlying magnetic background) remains present even when the external field is reduced to zero (fig.3.6d)). To check if the disordered vortex pattern was induced by any modification of the Py stripes, the sample was consequently warmed up above the Nb superconducting critical temperature, where stripes appeared to be unchanged from the original configuration.

The scenario of the vortex dynamic is completely different in

Nb(200nm)/Py(2 $\mu$ m), where spontaneous vortices appear below the superconducting critical temperature. In this case, there is no need to cool down the sample in a negative (positive) magnetic field and then sweep it to the opposite polarity, since both vortices and antivortices are already in the sample. The extremely high mobility of the spontaneous vortices was imaged by keeping the fast-scan axis as parallel as possible to the stripes in order to follow the vortex motion. Fig.3.6e-f-g-h show the MFM maps acquired while the field is sweeping respectively from  $-60G$  to  $-94G$ , from  $-159G$  to

$-191G$ , from  $-289G$  to  $-323G$  and from  $-483G$  to  $-516G$  and, due to the continuous motion of vortices under the tip apex, it was not possible to get a clear image of single, well defined, vortices. By sweeping the magnetic field down to  $-600G$ , no occurrences of avalanches were recorded.

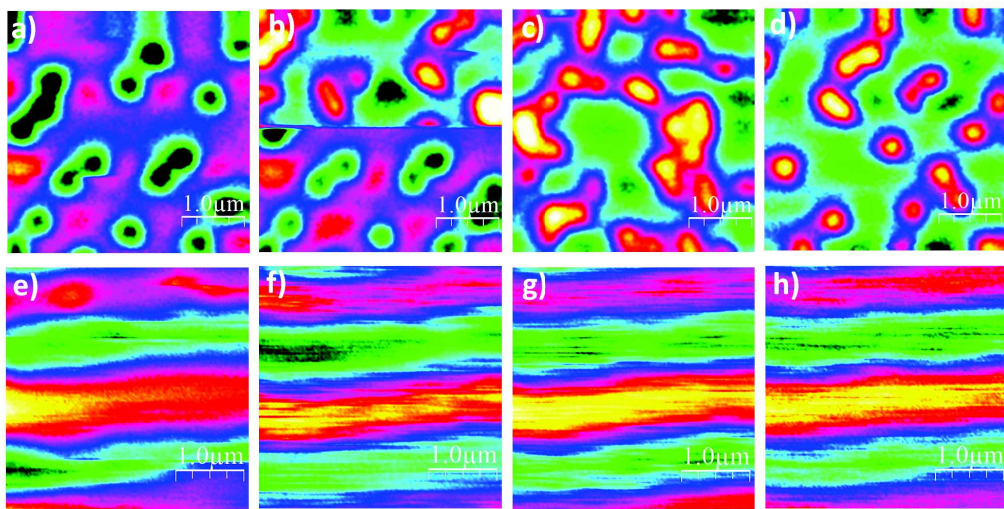


**Figure 3.6:** a)-d) MFM maps of Nb(360nm)/Py(1 $\mu$ m) at T=6K, h= 110nm. After a field cooling in  $H = -21G$ , the field has been swept up +80Oe (a), from +80Oe to +122G (b) kept constant at +122Oe (c) brought down to 0G (d). e)-f) MFM maps of Nb(200nm)/Py(2 $\mu$ m) at T=6K, h= 250nm. The field has been applied below  $T_s$  and swept from 0G to  $-600G$

### 3.5 Magnetization Measurements

Temperature-dependent low-field magnetization  $M(T)$  curves have been acquired on several Nb/Py samples, in zero-field-cooling (ZFC) and field-cooling (FC) processes as follows. The samples were first cooled down to 5K in zero magnetic field, then a small field was applied and the ZFC curve was obtained by measuring the magnetization as a function of the temperature during the warming of the samples up to 10K. After that, the FC curve was measured while cooling the sample down to 5K, in the presence of the applied magnetic field. In the inset of 3.7a, we report both the ZFC and FC curves measured in applied magnetic field of 20Oe perpendicular to the film plane for the sample Nb(200nm)/Py(2 $\mu$ m). The ZFC curve, in the main graph of 3.7a, shows the characteristic behavior of a superconducting  $M(T)$ , with the shielding of the magnetic field starting just below the superconducting critical temperature.

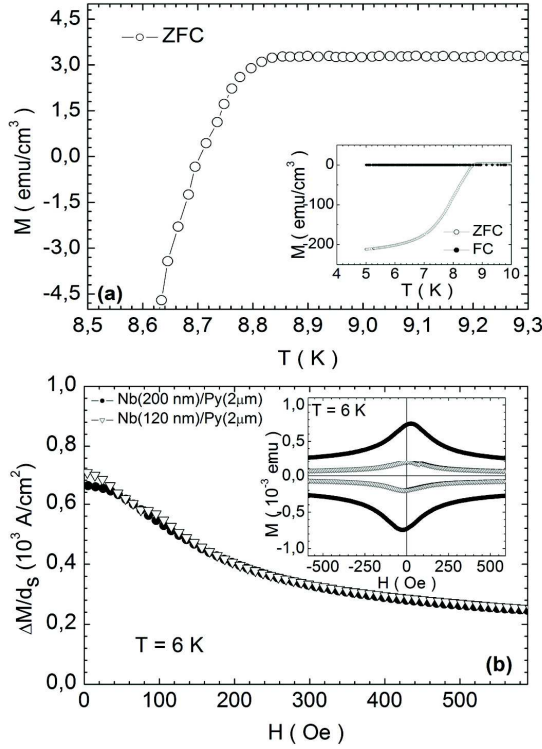


**Figure 3.7:** a) ZFC magnetization measured as function of  $T$  during the warming-up of the Nb(200nm)/Py( $2\mu\text{m}$ ) sample in a 20 Oe magnetic field perpendicular to the film plane. In the inset: ZFC and FC magnetization curves. b) Field dependence of the difference between the upper demagnetization branch and the lower magnetization branch of the loops in Nb(200nm)/Py( $2\mu\text{m}$ ) and Nb(120nm)/Py( $2\mu\text{m}$ ) normalized to the Nb layer thickness  $d_s$ . In the inset: hysteresis loops for both samples, at  $T=6$  K without the contribution of the Py film, in the perpendicular field configuration.

On the other hand, magnetic hysteresis loops measured below  $T_s$  (inset of fig.3.7) in perpendicular configuration on two different samples with the same Py thickness ( $2\mu\text{m}$ ), but Nb of 200nm and 120nm respectively, prove that the value of the critical current density  $j_c$  remains the same. This indicates that the vortex pinning is dominated by the underlying ferromagnetic layer rather than by an intrinsic pinning of Nb. The magnetic response of Nb layers at  $T=6$ K, shown in the inset of 3.75b, was determined by subtracting from the  $M(H)$  measured at  $T < T_s$  the same curve measured at  $T > T_s$ . From the hysteresis loops in the superconducting state, one can evaluate the critical current density by calculating the ratio  $\frac{\Delta M}{d_s}$ , where  $\Delta M$  is the difference between the

upper demagnetization and the lower magnetization branches of the loops and  $d_s$  is the Nb layer thickness. As shown in 3.7b, the  $\frac{\Delta M}{d_s}$  curves are perfectly overlapping.

### 3.6 Conclusions

In this chapter, vortex-antivortex formation in magnetically-coupled Nb/Py bilayers, by varying both the superconducting and ferromagnetic thicknesses has been investigated. By studying the magnetostatic interaction between S and F layers satisfying the constraint  $\frac{w}{\lambda} > 1$ , the threshold condition  $M_0 > M_{c(s,l)}$  to form spontaneous V-AV (straight or semiloops) can be derived, in both limits of superconducting layer thickness greater or smaller than the penetration depth,  $\frac{d_s}{\lambda} > 1$  or  $\frac{d_s}{\lambda} < 1$ . By analyzing the temperature behavior of  $M_{c(s,l)}(T)$ , one can deduce that vortices are always formed right below the superconducting critical temperature  $T_s$ , where  $M_{c(s,l)}(T_s) = 0$ . As the temperature decreases,  $M_{c(s,l)}(T)$  increases and the threshold condition can result to be no longer satisfied, allowing the exit of superconducting vortices from the S layer whenever the escape condition  $d_s \ll (\pi + 2)\lambda$  is respected. The studied Nb/Py samples always satisfy the escape condition, addressing the occurrences of spontaneous V-AV formation to a  $M_0$  value higher than  $M_{c(s,l)}(T)$ .

By referring to [2] for Nb(50nm)/Py(1 $\mu$ m) and to [1] for

Nb(100nm)/Py(1 $\mu$ m), we should expect spontaneous V-AVs if  $M_{0-Py(1\mu m)} > 15.9G$  and  $M_{0-Py(1\mu m)} > 15.1G$ , respectively. From transport measurements [6, 14, 15],  $M_{0-Py(1\mu m)} = 16G$  was estimated and from the imaging of spontaneous V-AVs in Nb(100nm)/Py(1 $\mu$  m),  $M_{0-Py(1\mu m)} > 15.1G$  was confirmed by MFM. On the other hand, the vortex nucleation in Nb(50nm)/Py(1 $\mu$  m) still leaves some open questions. A strong indication of the vortex nucleation in this sample is the presence of jumps appearing in the MFM map only below  $T_s$ . These jumps are the signatures of the interaction between the magnetic tip and the superconducting vortex. However, it is not surprising to find clearer evidence of spontaneous V-AVs in Nb(100nm)/Py(1 $\mu$ m) rather than in Nb(50nm)/Py(1 $\mu$ m). In fact, when the penetration depth  $\lambda(T)$  starts being greater than the superconducting thickness, it has to be corrected into  $\lambda_{eff}(T) = \lambda(T) \coth\left(\frac{d_s}{\lambda(T)}\right)$  [3]. As a consequence, as  $\lambda_{eff}(T) > \lambda(T)$ , vortices swell and a greater  $M_0$  value is required to accommodate them on the stripes. From a theoretical point of view, this results in using model [2] instead of [1] that fails to satisfy the validity condition  $\frac{d_s}{\lambda} > 1$ . In fig. 3.8, the behavior of  $M_c$  vs  $d_s$ , for the two models, together

with the dependence of  $\lambda_{eff}$  on the superconducting thickness, is reported. In the framework of model [2], any further reduction in the superconducting thickness, due for example to the presence of few oxide layers, will favor V-AV formation, provided that the condition  $\frac{w}{\lambda_{eff}} > 1$  is satisfied. In the case of Py( $1\mu\text{m}$ ), where  $w \approx 490\text{nm}$ , the thinnest superconducting layer satisfying the model results to be ideally  $10\text{nm}$  thick.

On the other hand, the spontaneous V-AV nucleation in

Nb( $120\text{nm}$ )/Py( $2\mu\text{m}$ ), Nb( $200\text{nm}$ )/Py( $2\mu\text{m}$ ) in comparison with the model [1] let us deduce  $M_{0-Py(2\mu\text{m})} > 21.1\text{G}$ .

In summary, the robustness of the two theoretical models describing spontaneous vortex formation in the S/F bilayer has been experimentally proved by the MFM results, as well as an estimate of the value of ferromagnet's spontaneous out-of-plane magnetization  $M_0$  has been inferred. In addition to this, the field cooled experiments demonstrate that either vortices or antivortices, depending on the sign of the external field, can be formed in the samples that lack sufficient magnetization to form spontaneous V-AV pairs. The zero-field cooled experiments on samples fulfilling the condition for spontaneous V-AV formation show that the V-AV population density can be unbalanced.

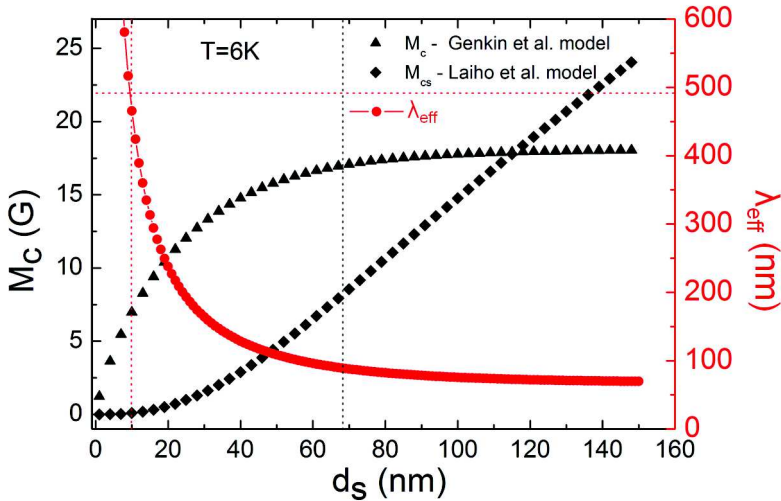


**Figure 3.8:** The behavior of  $M_c$ ,  $M_{cs}$  and  $\lambda_{eff}$  vs  $d_s$  at  $T=6\text{K}$  is reported. The intersection points between black dashed line- $M_c$  and black dashed line- $M_{cs}$  draw respectively the lower limit of the model [1] and the upper limit of [2]. The intersection point between the red dashed lines draws the lower limit of the model [2], resulting in  $d_s = 10\text{nm}$  in the studied S/F system

The dynamics of vortex and anti-vortex lattice under a changing applied magnetic

field has been additionally studied. Different behavior has been observed in the case of spontaneous V-AVs compared to the case of Vs (or AVs) formed in external field cooling. After a field cooling in a negative static field, Nb(360nm)/Py(1 $\mu$ m), in the under-threshold regime, correctly shows Vs populating the proper stripes. This vortex configuration appears rigid when the field is swept from negative to positive values, up to 122G when an avalanche of antivortices penetrates the superconducting layer. In fact, once this critical field is reached, vortices are locally driven out and antivortices completely penetrate inside the sample, regardless of underlying magnetic template. A different case of vortex lattice displacement before and after an avalanche in the Nb(200nm)/Py(1 $\mu$ m) sample is reported in literature [16]. In that case, even though the antivortices suddenly penetrated the Nb layer, the magnetic confinement imposed by the Py stripe domains was still visible. The antivortex dislocation occurring in Nb(360nm)/Py(1 $\mu$ m) can be addressed to the decreasing influence of the magnetic template on the Nb surface by increasing the Nb thickness so that, in a thick superconducting layer, during an abrupt phenomenon such as the avalanche, the antivortices can assume a disordered configuration. On the other hand, if the magnetic field is swept in the presence of spontaneous V-AVs, a completely different vortex dynamic occurs. No avalanches have been observed in Nb(200nm)/Py(2 $\mu$ m) by ramping the external magnetic field from 0 to  $-600G$ , but a continuous motion of V-AVs occurs, as revealed in the MFM data. The magnetic template guided the vortices along the magnetic channels, preventing them from crossing the domain walls.

# Bibliography

- [1] R. Lahio, E. Lähderanta, E. B. Sonin, K.B. Traito, *Phys. Rev. B* **67**, 144522 (2003)
- [2] G.M. Genkin, V.V. Skuzovaktin, I.D. Tokman, *J. Magn. Magn. Mater.* **130**, 51 (1993)
- [3] A.I. Gubin, K.S. Il'in, S.A. Vitusevich, M. Siegel, N. Klein, *Phys. Rev. B* **72**, 064503 (2005)
- [4] B.V. Petukhov, and V.R. Chechetkin, *Zh. Eksp. Teor. Fiz.* **65**, 1653 (1973) [Sov. Phys. JETP 38, 827 (1974)]
- [5] A.I. Buzdin, *Rev. Mod. Phys.* **77**, 935 (2005)
- [6] M. Iavarone, A. Scarfato, F. Bobba, M. Longobardi, G. Karapetrov, V. Novosad, V. Yefremenko, F. Giubileo, and A. M. Cucolo, *Phys. Rev B* **84**, 024506 (2011)
- [7] L.P.Gorkov, *Zh. Eksp. Teor. Fiz.* **36**, 1918 (1959) [Sov. Phys. JEPT 9, 1364 (1959)]
- [8] P.H. Kes, and C.C. Tsuei, *Phys. Rev. B* **28**, 5126 (1983)
- [9] J. B. Youssef, N. Vukadinovic, D. Billet, and M. Labrune, *Phys. Rev. B* **69**, 174402 (2004)
- [10] Y. Murayama, *J. Phys. Soc. Jap.* **21**, 2253 (1966)
- [11] S. Chikazumi, *Physics of Ferromagnetism*, Oxford University Press Inc., New York (1997)
- [12] N. Amos, R. Fernandez, R. Ikkawi, B. Lee, A. Lavrenov, A. Krichevsky, D. Litvinov, and S. Khizroev, *J. Appl. Phys.* **103**, 07E732 (2008)

- 
- [13] F. Bobba, C. Di Giorgio, A. Scarfato, M. Longobardi, M. Iavarone, S. A. Moore, G. Karapetrov, V. Novosad, V. Yefremenko, and A. M. Cucolo, *Phys. Rev. B* **89**, 214502 (2014)
- [14] A. Belkin, V. Novosad, M. Iavarone, J. Fedor, J.E. Pearson, A. Petrean-Troncalli, G. Karapetrov, *Appl. Phys. Lett.* **93**, 0725110 (2008)
- [15] A. Belkin, V. Novosad, M. Iavarone, R. Divan, J. Hiller, T. Proslie, J.E. Pearson, G. Karapetrov, *Appl. Phys. Lett.* **96**, 092513 (2010)
- [16] A. M. Cucolo, A. Scarfato, M. Iavarone, M. Longobardi, F. Bobba, G. Karapetrov, V. Novosad, and V. Yefremenko, *J. Supercond. Nov. Magn.* **25**, 2167 (2012)

# Chapter 4

## Vortex confinement in S/F hybrids

### 4.1 Introduction

Topological defects and singularities are often present in the microscopic structure of magnetic materials as showed by a variety of imaging methods: optical microscopies (magnetic Kerr and Faraday), electron-based microscopies (Lorentz, spin resolved scattering and photoemission), X-ray microscopies (transmission and circular dichroism), local probe microscopies (magnetic force and spin polarized scanning tunneling microscopy) [1]-[9]. Some of these techniques have been successfully used to investigate the superconducting vortex distribution and dynamics both in superconducting thin films and in S/F heterostructures [10]-[16] as well. Here, the existence of a stable mixed state results from the intrinsic repulsive interaction between superconducting vortices of the same polarity. However, peculiar cases of attractive vortex-vortex interaction have been also considered and reported in literature [17]-[23]. In such a scenario, a first order phase transition occurs at the lower critical field  $H_{c1}$ , with a discontinuous increase of flux density. In this case, many vortices abruptly penetrate the superconductor in the form of lattice or chains. Moreover, clusters of flux quanta might be induced in S/F superlattices as a consequence of the spatial modulation of the magnetic susceptibility, resulting in vortex attraction [24]. This being said, also in the standard scenario of vortex-vortex repulsion, vortex chains and vortex clusterization

as well as multi-vortex and giant vortex phases can be induced by a strong confinement potential, either magnetic or geometric [25]-[29].

Up to now, low temperature magnetic force microscopy (MFM) has been a useful tool to image vortex clusters pinned by a periodic array of magnetic dots in S/F structures [30],[31] as well as vortex chains in S/F bilayers only magnetically coupled [32]-[35]. On the other hand scanning tunneling microscopy and spectroscopy (STM/STS) has been successfully used by Roditchev *et al.* [36] to study the geometrical confinement effects on the stabilization of superdense multivortex and giant vortex phases. In this chapter, it will be shown as intrinsic dislocations of a stripe-like magnetic pattern, forming *bifurcations*, can act as confinement sites for superconducting vortices. The magnetic imaging of such dislocations, above and below the S critical temperature  $T_s$ , is of fundamental relevance to get insight into both their magnetic topology and their confinement power for superconducting vortices. To study the local magnetic behavior of ferromagnetic sample MFM is an extremely useful tool, even though it is only sensitive to out-of-plane stray fields and it is limited by a lower spatial resolution of few tenth of nm, strongly dependent on the lift-height used while scanning. MFM allows imaging of flux quanta as well, being sensitive to the London penetration depth  $\lambda$ , which measures the magnetic field decay from the normal core. On the other hand, once the magnetic structure is known, STM/STS, sensitive to spatial variation of the amplitude of the superconducting order parameter rather than the magnetic profile, make possible detailed measurements of the density of electronic states (DOS) outside and inside the vortex core, with a sub-nanometric spatial resolution.

## 4.2 Sample Fabrication and Preliminary Characterization

Several S/F heterostructures only magnetically coupled, made by Nb/Py and Pb/[Co/Pd]*multilayers*, were fabricated for MFM and STM/STS investigation respectively.

Nb/*SiO*<sub>2</sub>/Py, consisting of 100–, 150–, 200 – nm of Nb as the superconductor and 1–, 1.5 –  $\mu$ m of Py as ferromagnet, were fabricated ex-situ for MFM measurements, by following the deposition procedure described in Chapter 3, section 3.2.

Pb/*Al*<sub>2</sub>*O*<sub>3</sub>/[Co/Pd]*multilayers*, consisting of 30-nm film of Pb as the superconductor

and 200 bilayers of Co(2nm)/Pd(2nm) as the ferromagnet, were made for STM/STS analysis. The Co/Pd multilayers were deposited ex-situ, at *Argonne National Laboratory* (Chicago, IL (USA)) by Dr. Valentyn Novosad, on Si substrates by dc sputtering in a dedicated system and in presence of an applied in-plane magnetic field, favoring a stripe-like magnetic domain pattern. A 10-nm  $Al_2O_3$  film was made by rf sputtering deposition from an Al target, in order to insulate the F from the S layer and suppress the proximity effect. Finally, a 30-nm Pb film was deposited in-situ via e-beam evaporation at low temperature (120 K) and base pressure of  $10^{-11}$  Torr, followed by a room temperature annealing. This procedure guaranties a flat and clean surface, suitable for STM studies. The UHV chamber, where Pb films were made is linked to the STM chamber where the experiments were performed, in order to avoid surface contamination due to the exposure of the films to the air. It is well known that Pb bulk exhibits a type-I superconductivity (with  $\xi_{Pb,bulk}(0) \approx 83nm$  and  $\lambda_{Pb,bulk}(0) \approx 37nm$ ), however, Pb thin films allow the penetration of flux quanta, behaving as type-II superconductors. In a twin 30-nm Pb film a  $\xi_{Pb}(0) \approx 54nm$  [37] has been measured as well as  $\lambda_{Pb}(0) \approx 134nm$  has been calculated, by using  $\lambda_{Pb,bulk}(0) \approx 1.83 \frac{\xi_{Pb}(0)\lambda_{Pb}(0)}{\xi_{Pb,bulk}(0)}$  [38] and by taking into account the thickness correction  $\lambda_{eff}(T) = \lambda(T) \coth\left(\frac{d_s}{\lambda(T)}\right)$  [39]. Thick Py films, as well as Co/Pd multilayers, have striped magnetic domain pattern, made by magnetization vectors with out-of-plane components alternating direction from one stripe to the next. However, as discussed in Chapter 3, in Py, the in-plane easy magnetization axis is such that the canting angle of the magnetization vector is very small and magnetic stripe domains are formed only when a critical thickness ( $t_c \approx 200 - 300nm$ ) is overcome. Above this threshold, the stripe width  $w$  grows as the square root of the film thickness  $d_m$  [40],[41]. A Py thickness of  $1 - 1.5\mu m$  ensures stripes big enough ( $w \approx 500nm$ ) to accommodate vortices in Nb, whereas at the measurement temperature of  $T = 6K$ ,  $\lambda_{Nb}(6K) \approx 68nm$ . The domain size as well as the weakness of the out-of-plane magnetic stray field of Py are suitable for MFM experiments, whereas, on the contrary,  $[Co/Pd]_{multilayers}$ , having an out-of-plane easy magnetization axis and a relatively high stray field, would cause overlapping of superconducting vortices on the scale of  $\lambda$ , eventually not individually resolvable by MFM. On the other hand, a smaller domain width of  $w \approx 200nm$  can be achieved in  $Co(2nm)/Pd(2nm)_{200-bilayers}$ , which, for technical reasons, helps during STM/STS experiments. In fact, the Unisoku USM1300  $^3He$  STM has a maximum scan size of around  $500nm \times 500nm$  at the measurement temperature of  $T = 1.5K$ . In addition

to this, while Nb is not a good material for STM investigation, due to the ease in oxidation, Pb, with a  $T_c = 7.2K$ , is not suitable for the presented MFM experiments, performed in the Omicron-SFM, limited by a base temperature of  $5K$ .

Magnetic imaging available in literature as well MFM maps presented in this chapter clearly show that dislocations where two domains converge and coalesce in a single domain, namely *bifurcations*, often occur in ferromagnetic materials with stripe-like pattern of the magnetization (fig.4.1a). While those are driven only by the out-of-plane magnetization in  $[Co/Pd]_{multilayers}$ , in Py the role of the in-plane magnetization has to be taken into account.

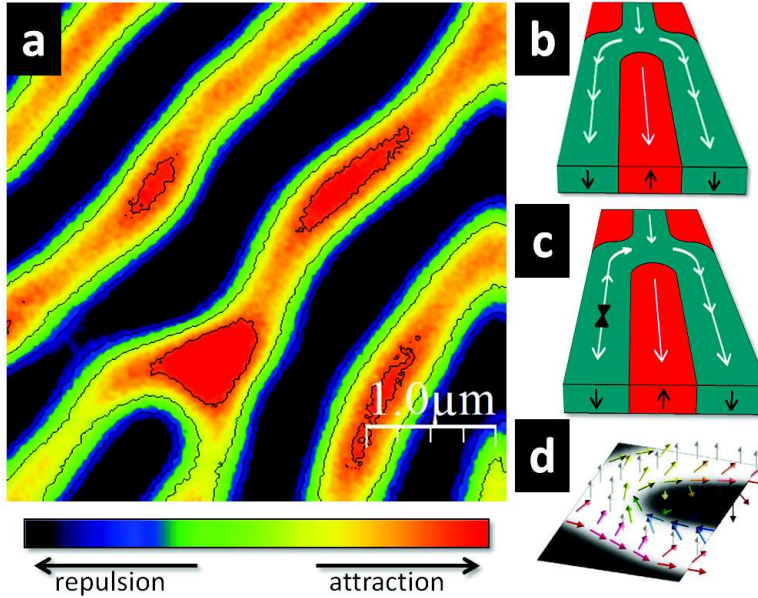


**Figure 4.1:** a) MFM map showing a *bifurcation* in Nb(200nm)/Py(1μm) at T=13K; b) sketch of the in-plane magnetization vector around the bifurcation; c) sketch of the in-plane magnetization vector around the bifurcation in presence of reversed in-plane domains. d) micromagnetic simulation of meron-like spine texture at the dislocation site [9].

From the micromagnetic point of view, two possibilities can occur at the bifurcation core: either the in-plane magnetization keeps the same direction all around the bifurcation (fig.4.1b) or an in-plane reversed magnetization vector makes half of a magnetic vortex around the endpoint of the opposite stripe (fig.4.1c). In fact, due to topological defects along the stripes, a Bloch point can suddenly occur, causing an in-plane

magnetization reversal process. From here, the in-plane magnetization with reversed component can travel along the stripe, eventually running into a bifurcation where it makes  $180^\circ$  rotation. However, in the latter case, not only the in-plane magnetization makes half of a magnetic vortex around the stripe endpoint but also the out-of-plane component flips its polarity by crossing the domain wall from the bifurcation core to the interrupted stripe (fig.4.1d). The combination of these two effects, gives rise to a *meron-like spin texture*. This peculiar magnetic configuration has been predicted to appear at stripe endpoints in helical magnets [44] and brought up to the evidence by high resolution transmission X-ray magnetic microscopy in ferromagnetic thin films [9]. Unfortunately, MFM cannot to discern whether or not there is a *meron* around the endpoint of the interrupted domain.

However, a common feature of all the MFM images acquired in several dislocations, on both Py and Co/Pd multilayers ferromagnets, is the strong enhancement of the magnetic contrast at the bifurcation core.

It is well known that materials with weak and high perpendicular anisotropy,  $Q = \frac{K_u}{K_d} \ll 1$  and  $Q = \frac{K_u}{K_d} \gg 1$ , present different magnetic domain arrangements as well as stray field profiles. In high-Q materials the stray field has been described as the consequence of a periodic distribution of magnetic charges  $\pm 4\pi M_s$  in neighboring domains, arising from the discontinuity of the magnetization at the surface (fig.4.2a). In low-Q materials, as Py, the domains are not homogeneously magnetized perpendicular to the surface but form a twisted structure (*closure domains*) (fig.4.2b,c). This corresponds to having magnetic charges that are not residing at the surface but are distributed within some layers near the surface. The resulting out-of-plane stray field is weaker than in the high-Q materials and presents smoother profile. However, recent micromagnetic simulations, based on experimentally measured magnetization loops, support the presence of closure domains also in  $[Co/Pd]_{multilayers}$  films, even being a high-Q material. Further investigation are needed to follow up in this direction.

Figures 4.2a,b show the front view of a section of high-Q and low-Q materials respectively, with a schematic of magnetic domain arrangement and stray field lines. As shown in fig.4.2b (and in the 3D sketch of fig.4.2c), in low-Q materials the *closure domains* appear at the domain walls near the sample surfaces with the aim of confining part of the magnetic flux inside the sample itself, because the gain in the magnetostatic energy is higher than the lost in the magnetic anisotropy. On the contrary, in high-Q materials, the magnetic anisotropy is too strong to allow the formation of closure

domains. In fact, in such domains, the magnetization direction is normal to the out-of-plane magnetization (as well as to the in-plane component in Py-like ferromagnets). The formation of the closure domains at the domain walls causes a reduction of the out-of-plane surface magnetization as well as a sinusoidal modulation of the out-of-plane stray field.

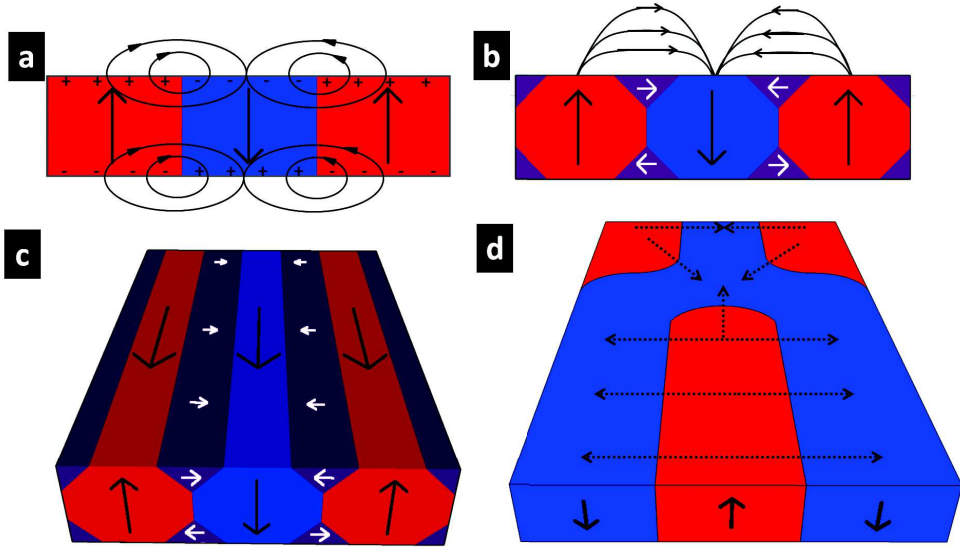


**Figure 4.2:** a)-b) front view of a section of high-Q and low-Q materials respectively, showing magnetic domain arrangement and stray field lines. c) 3D sketch of magnetic domain arrangement in low-Q materials; d) 3D sketch of a magnetic bifurcation. Dotted arrows are representative of stray field lines which converge at the bifurcation core and at the end point of the interrupted stripe.

Whether or not the closure domains are formed in the ferromagnet, the deviation from a regular domain arrangement that happens in presence of a bifurcation pushes the stray field lines to converge on the bifurcation core as well as at the end point of the interrupted stripe (see fig.4.2d), thus causing the experimentally measured enhancement of the out-of-plane stray field. In addition to this, in presence of closure domains, the stray field lines coming from the exceeding volume of magnetic material at the bifurcation core, with respect to the stripe magnetic channel, are not confined by the closure domains, thus allowing the enhancement of the out-of-plane magnetic signal.

### 4.3 MFM study of vortex confinement in Nb/Py

In fig.4.3, the comparison between MFM maps acquired above (fig.4.3a, b, c) and below (fig.4.3d, e, f) the Nb critical temperature on three different samples, respectively Nb(150nm, 200nm, 100nm)/Py( $1\mu\text{m}$ ), are shown. Above  $T_s$ , at  $T = 13\text{K}$ , the images show the peculiar stripe-like domain pattern of Py, with a stripe width  $w \approx 500\text{nm}$ , focusing on dislocations of the regular magnetic structure.

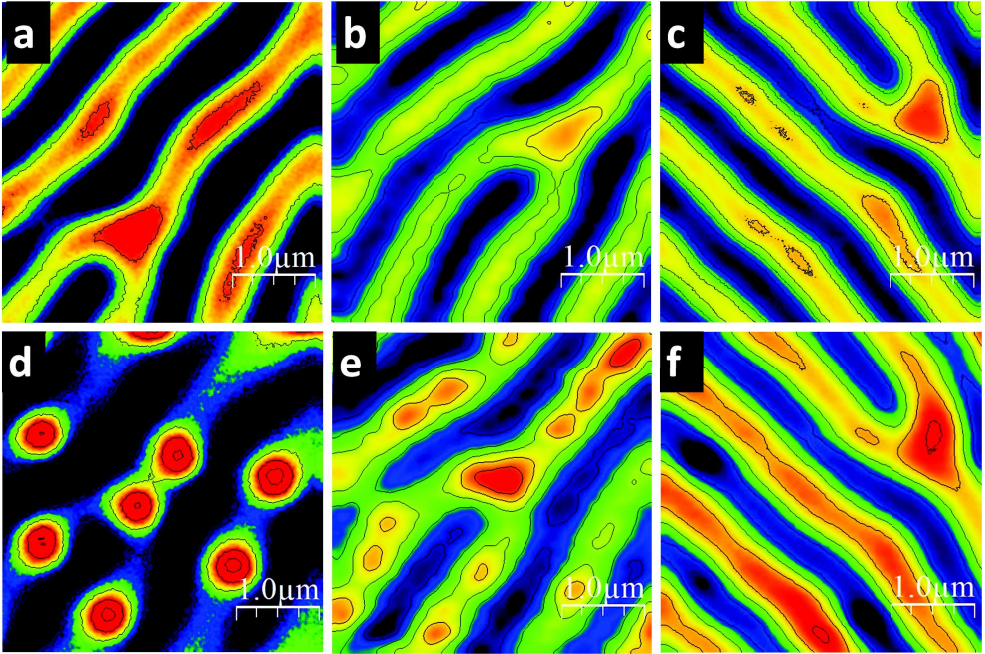


**Figure 4.3:** (a - b - c) MFM maps acquired at  $T = 13\text{K}$  and  $H = 0$  on Nb(150nm)/Py( $1\mu\text{m}$ ), Nb(200nm)/Py( $1\mu\text{m}$ ) and Nb(100nm)/Py( $1\mu\text{m}$ ) respectively. MFM maps acquired at  $T = 6\text{K}$  and on (d) Nb(150nm)/Py( $1\mu\text{m}$ ) field cooled in the magnetic tip's field, (e) Nb(200nm)/Py( $1\mu\text{m}$ ) field cooled in  $H = 30\text{Oe}$ , (f) Nb(100nm)/Py( $1\mu\text{m}$ ) zero field cooled. Each map is  $3.8\mu\text{m} \times 3.8\mu\text{m}$  in size. MFM maps above and below  $T_s$  are affected by a small thermal drift.

The significantly increase of the magnetic contrast at the core of the bifurcation is representative of stronger stray-field coming out from there.

Below the Nb  $T_s$ , superconducting vortices are favored to nucleate at the fork. Figure 4.3d shows the MFM map acquired on Nb(150nm)/Py( $1\mu\text{m}$ ) at  $T = 6\text{K}$  after a field cooling in the magnetic tip's field. A vortex sits in the middle of the dislocation and it is spaced from its nearest neighbor by a distance sensibly smaller than the recip-

rocal distance between the others. Differently, MFM maps acquired at  $T = 6K$  on Nb(200nm)/Py(1 $\mu m$ ) (fig.4.3e) and Nb(100nm)/Py(1 $\mu m$ ) (fig.4.3f) show a magnetic spot with strong contrast on the bifurcation, surrounded by individual vortices nucleated in a field cooling of  $H = 30Oe$  and in zero field cooling respectively. Unfortunately, the MFM lateral resolution is not enough to discriminate a vortex cluster rather than the nucleation of a giant vortex at the bifurcation.

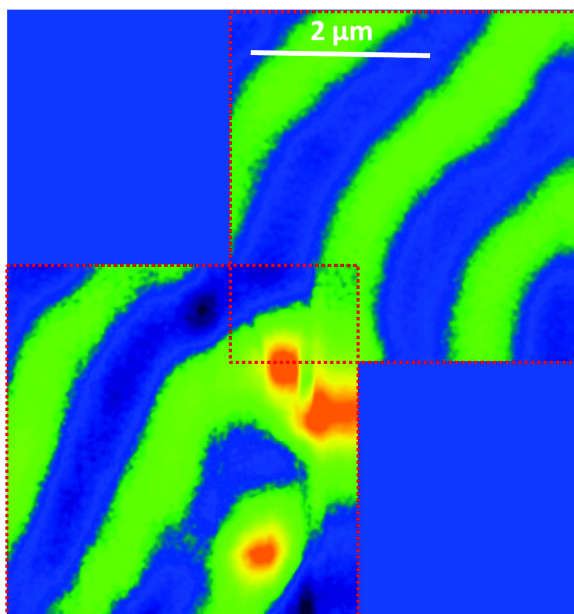


**Figure 4.4:** patchwork of two MFM images acquired at  $T = 6K$ , after a zero field cooling, in adjacent and partially overlapping locations on Nb(150nm)/Py(1.5 $\mu m$ ) surface. Each map is 3.8 $\mu m \times 3.8\mu m$  in size.

Moreover, a patchwork made by two MFM maps acquired after a zero field cooling on Nb(150nm)/Py(1.5 $\mu m$ ) at  $T = 6K$ , shows again a superconducting vortex nucleation at the dislocation site. It is worth to notice that either a couple of vortices, or a vortex moveable due to scanning, appear on the top of the bifurcation, a vortex of opposite polarity (antivortex) is consequently induced on the adjacent and opposite stripe and a third, red, vortex appears in proximity of the dislocation. No other vortices (or antivortices) populate the imaged areas, being the proof that the local equilibrium magnitude of the out-of-plane magnetization might not be enough to nucleate spontaneous vortices [35], [42], [43]. However, vortex nucleation is expected wherever the stray field is high enough, that might be bifurcations or topological defects of the

magnetic structure where Bloch points occur. In such a case, the spontaneous vortex nucleation at the bifurcation, together with the single isolated vortex along the stripe, might appear as a consequence of a Bloch point-meron pair.

In fig. 4.5 a strip of  $12\mu\text{m} \times 3.6\mu\text{m}$  in size, made by a patchwork of MFM images acquired at  $T = 6\text{K}$  in four adjacent and partially overlapping locations on Nb(150nm)/Py( $1\mu\text{m}$ ) surface, is presented. After a stray field unbalancing of  $7.5\text{Oe}$  was measured, the sample was cooled down in  $H = 11.5\text{Oe}$ . Such a value guaranties the achievement of the matching field  $H_m = \frac{2}{\sqrt{3}} \frac{\Phi_0}{d^2}$  [45], having one flux quantum per unit cell of the hexagonal array, where the vortex-vortex distance  $d$  is tuned by the pinning potential period, resulting in the stripe period in the considered system.

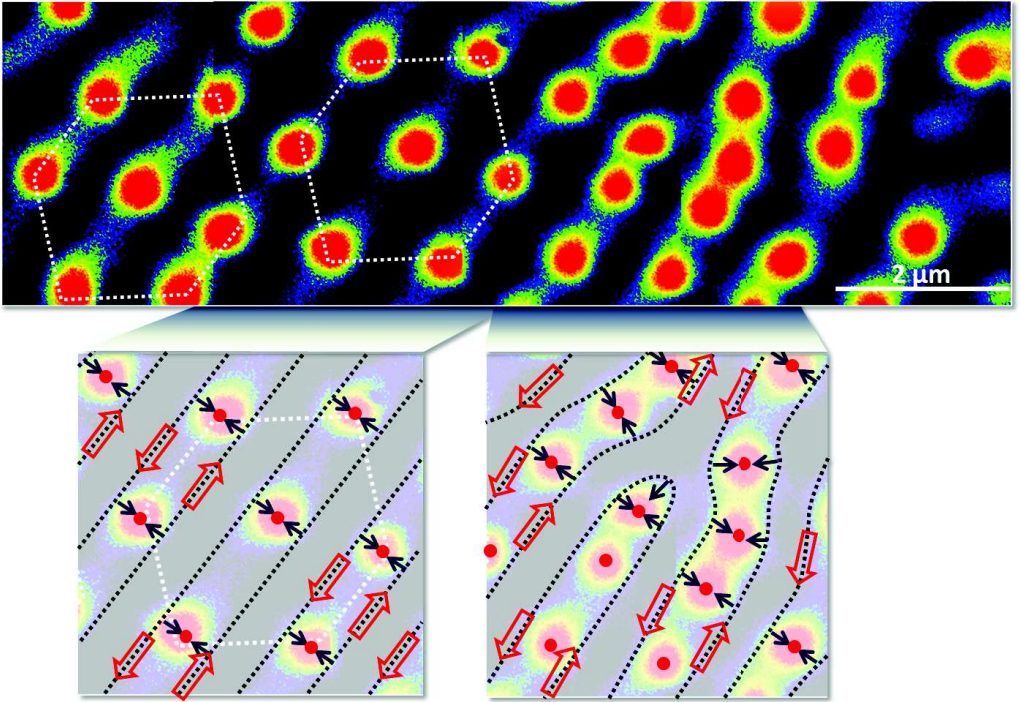


**Figure 4.5:** Upper side: patchwork of four MFM images acquired at  $T = 6\text{K}$ , after a field cooling in  $H = 11.5\text{Oe}$ , in adjacent and partially overlapping locations on Nb(150nm)/Py( $1\mu\text{m}$ ) surface. The total size of the strip is  $12\mu\text{m} \times 3.6\mu\text{m}$ . Bottom side: sketch of supercurrent path (red arrows) on the top of domain walls and of the Lorentz force vectors (blue arrows) acting on vortices.

After the field cooling, vortices nucleate on the proper underlying magnetic domains, with a polarity triggered by the external field. They appear on a partially shielded background, where the weakness of the superconducting diamagnetism, due to a thin

Nb film, helps to recognize the magnetic stripe-like pattern underneath. Wherever the stripe pattern is straight and regular, as in the left half-image of fig.4.5, hexagonal arrangement of vortex lattice occurs. In the right half-image the regularity of the hexagonal array is lost and an inhomogeneous distribution of flux quanta takes place, with a higher vortex density. Such less regular arrangement is clearly driven by the presence of two dislocations of the magnetic stripe structure. Here, the curvature of two stripes converging in the bifurcation, acts as an accumulation area, proving that the topology itself of the bifurcation affects vortex distribution. In fact, vortex configuration inside the stripes is set by Lorentz force, external magnetic field, vortex-vortex repulsion and magnetic confinement. In presence of straight magnetic domains, the Lorentz force vectors, being always normal to the domain walls where supercurrents flow and parallel to each others, push vortices in the middle of the stripes (bottom-left side of fig.4.5). In such a case, the vortex distribution is set by their reciprocal repulsion, causing an uniform intervortex distance, fixed by the net magnetic field experienced by the S, sum of F stray field and external applied field. Instead, whenever the domain walls curve, the Lorentz force vectors are locally not parallel (bottom-right side of fig.4.5), causing modulations of the intervortex distance. Moreover, right at the bifurcation core the matching condition is not longer satisfied because of the enlargement of the domain size and, in addition to this, the interruption of a domain abruptly causes one period shift of the vortex lattice.

In addition to this, MFM maps shows that a shortening of the vortex-vortex distance can happen whenever the magnetic channels abruptly interrupt or make a fork. In fact, along a magnetic channel of infinite length, provided the magnitude of the external field, vortices would make a chain keeping a constant vortex-vortex distance. Here, each vortex inside the chain, would feel the same net repulsive force from each one of its two sides, thus leading to a constant intervortex distance. On the contrary, a force unbalancing is felt by vortices close to magnetic channel interruptions. On one side they feel a long-range repulsive interaction due to the semi-infinite vortex chain, whereas on the other side only the Lorentz Force would keep them away from the domain wall.

## 4.4 STM/STS study of vortex confinement in Pb/[Co/Pd]

Whenever MFM fails in discriminating between vortex cluster and giant vortex, STM/STS techniques can be complementary used. Despite the lost of magnetic resolution, STM/STS allow vortex imaging with higher lateral resolution up to very high magnetic fields.

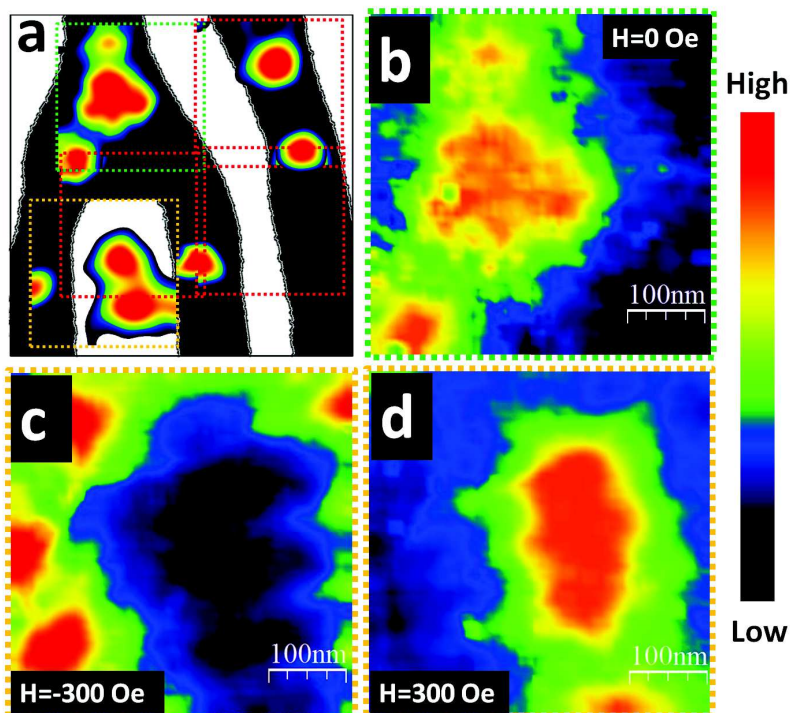


**Figure 4.6:** (a) cartoon of the position of spontaneous superconducting vortices in  $\text{Pb}(30\text{nm})/[\text{Co}(2\text{nm})/\text{Pd}(2\text{nm})]_{200}\text{bilayers}$  on the top of an orientative distribution of magnetic domains, made by five conductance maps, each of them  $438\text{nm} \times 438\text{nm}$  in size, acquired at the Fermi energy at  $T = 1.5\text{K}$  after a zero field cooling. (b) conductance map at the dislocation, in green dotted square, acquired at the Fermi energy at  $T = 1.5\text{K}$  and in zero field cooling. (c-d) conductance maps of the area in yellow dotted square, acquired at the Fermi energy at  $T = 1.5\text{K}$  after a field cooling in  $H = -300\text{Oe}$  and  $H = 300\text{Oe}$  respectively

The cartoon of fig.4.6a draws the position of superconducting vortices in

Pb(30nm)/[Co(2nm)/Pd(2nm)<sub>200-bilayers</sub>] with respect to an orientative distribution of magnetic domains. It is made by five conductance maps, acquired at the Fermi energy at  $T = 1.5K$  after a zero field cooling.

Vortices and antivortices appear as spots with higher zero bias conductance with respect to the superconducting background which is here masked by the cartoon of the magnetic texture. By repeatedly field-cooling the sample below  $T_s$  in opposite magnetic fields, the distribution of magnetic domains can be unambiguously determined by looking at the nucleation sites of superconducting flux quanta (downward stripes for vortices, upward stripes for antivortices) [37]. For example, fig. 4.7 shows two patchworks of conductance maps, acquired at the Fermi energy at  $T = 1.5K$ , after field cooling the sample in  $H = -300Oe$  and  $H = 300Oe$  respectively (except for the conductance map right on the top of the bifurcation core, which was taken in zero field cooling and it is here reported for spatial reference). Superconducting vortices appear on stripes with magnetization collinear to the external magnetic field. Room temperature MFM on Co(2nm)/Pd(2nm)<sub>200-bilayers</sub> [37] confirms stripe-like magnetic domains.

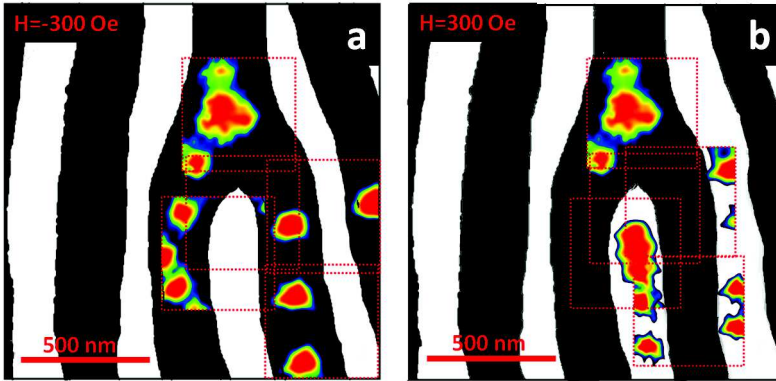


**Figure 4.7:** (a)cartoon of the magnetic structure of Co(2nm)/Pd(2nm)<sub>200-bilayers</sub>, deduced by field cooling the sample in  $H = -300Oe$  and  $H = 300Oe$  respectively. Only the map right on the top of the bifurcation core is acquired after a zero field cooling and it is here reported for spatial reference. Each map is  $438nm \times 438nm$  in size and it has been acquired at the Fermi energy at  $T = 1.5K$ .

Conductance maps in zero field cooling (fig. 4.6a) show the presence of spontaneous vortices and antivortices whereas an agglomeration of flux quanta (green dotted square in fig.4.6a, enlarged in 4.6b) appear at the bifurcation core, where the vortex nucleation is locally favored because of the enhancement of the stray field.

Figures 4.6c-d show conductance maps, at  $T=1.5K$  and at the Fermi energy, taken in

the area enclosed in the yellow dotted square, after a field cooling in  $H=-300\text{Oe}$  and  $H=300\text{Oe}$  respectively. A curling distribution of individual and well spaced vortices appears in fig.4.6c, while, in the opposite field, fig.4.6d, antivortices agglomerate at the end point of the interrupted stripe. Here, spectroscopic analysis confirms the nucleation of a vortex cluster, made by three individual flux quanta.

The 3D plot of fig.4.8a shows the evolution of superconducting DOS along the dotted line in the inset of fig.4.8b. Moving inside the vortex cluster, superconducting gap and coherence peaks become less pronounced and superconductivity is fully suppressed in three separate locations, where zero bias peaks are measured.

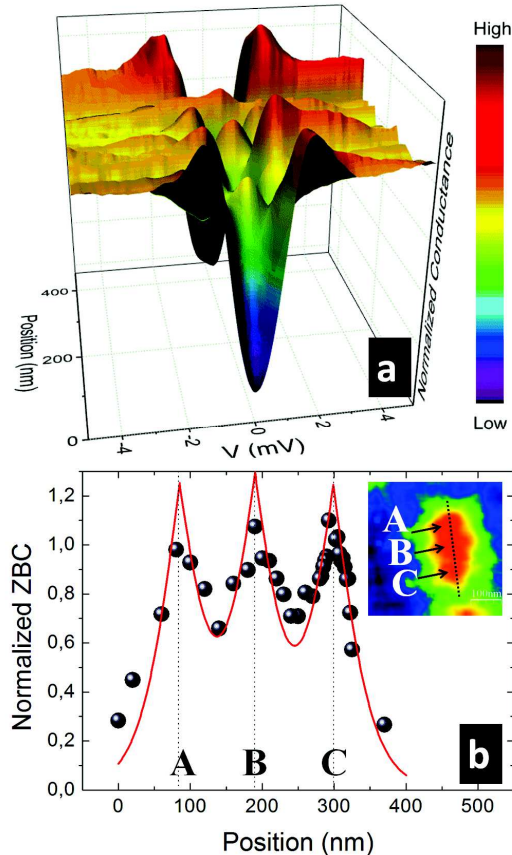


**Figure 4.8:** (a) 3D plot of the spatial evolution of the electronic DOS along the dotted line in the inset of (b). (b) Plot of normalized ZBC vs position along the dotted line in the inset.

In fact, when moving the STM tip closer to the vortex core a pronounced peak in the conductance spectra can be observed at small bias, whenever the superconductor

is in the clean limit regime [46], [47]. Moreover, superconducting DOS features are completely recovered outside of the cluster.

Normalized ZBC has been plotted as a function of position (black dots) in fig.4.8b. The three ZBC peaks have been fitted by the function  $\sum_{i=1,2,3} \left[ 1 - \tanh\left(\frac{(x-x_i)}{\xi}\right) \right]$ , where  $x_i$  is the position of each vortex core [48]. The best fit is given by  $\xi = 55nm$ , in good agreement with previous results on twin samples [37]. A vortex-vortex distance of 105nm and 109nm can be measured between A-B and B-C respectively, inferring an intervortex separation about 1.4 times smaller than the minimum value possible  $d = 2.8H_{c2}$ , achievable at the second critical field  $H_{c2}$  for fully separated vortices in bulk superconductors.

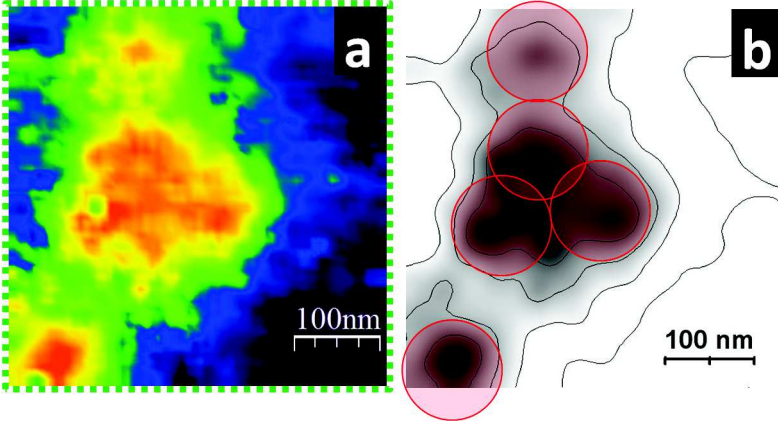


**Figure 4.9:** (a) 3D plot of the spatial evolution of the electronic DOS along the dotted line in the inset of (b). (b) Plot of normalized ZBC vs position along the dotted line in the inset.

Finally, in fig.4.9a, the conductance map at the dislocation, in green dotted square is enlarged. In fig.4.9b raw data have been filtered by a two-standard deviation 2D Gaussian smoothing, with a kernel size of 15 pixels, corresponding to 105nm (about the vortex size), and reported in a black-white color scale, with a completely saturated contrast of the superconducting background (made by SPIP-Image Metrology software). Red circles, with radius fixed by  $\xi = 55nm$ , on the top of the map, work as guide for the eye in order to identify the number of vortices inside the agglomeration. Three hot spots show up, suggesting the establishment of a multivortex phase with multiplicity  $L = 3$ .

## 4.5 Conclusions

In this chapter, direct observation of superconducting vortex clusters and vortex accumulation as a consequence of topological defects of the magnetic structure in S/F thin film hybrids has been reported.

MFM measurements clearly show that bifurcations, where two domains converge and coalesce in a single domain, often occur in ferromagnetic materials with stripe-like pattern of the out-of-plane magnetization and always support an enhancement of the out-of-plane stray field. Such a phenomenon has been related to the deviation from a regular path of the stray field lines which merge at the bifurcation core and at the end point of the interrupted stripes. This happens both in high-Q ferromagnets (Co/Pd multilayers) as well as low-Q ferromagnets (Py). However, more peculiar magnetic configurations can take place in low-Q materials, where *closure domains* are formed near to the surfaces, thus attenuating the surface magnetization, and *meron-like spin textures* can eventually occurs. In the latter, half of a magnetic vortex made by the in-plane magnetization around the end point of the interrupted stripes occurs together with the flipping of the out-of-plane magnetization by crossing the domain wall. When this happens, one should expect the presence of a Bloch point along the stripe, where an in-plane magnetization reversal process has taken place. Eventually a Bloch point might work as pinning site for superconducting vortices as well as the enhancement of the out-of-plane stray field.

Below  $T_s$  and in zero field cooling, vortex nucleation at the bifurcation can be favored even when the out-of-plane component of the magnetization is not enough for their spontaneous formation (fig.4.4) [35], [42], [43]. In such a case, a suspicious vortex distribution in a sample where the local equilibrium value of the out-of-plane magnetization was not enough to nucleate quantum fluxes, has been interpreted as a consequence of a Bloch point-meron pair underneath.

Apart from the peculiar magnetic configuration, the topology of the bifurcation itself always affect vortex distribution. In S/F hybrids, such distribution is set by Lorentz force, external magnetic field, vortex-vortex repulsion and magnetic confinement. Provided the magnitude of the magnetic field experienced by the S, it has been shown how the stripe curvature changes the vortex distribution due to the local variation of the Lorentz force vector direction, always normal to the domain walls. In addition to this, whenever the magnetic channels abruptly interrupt or make a fork, a shortening of the

intervortex distance occurs due to the unbalancing of the long range repulsion, which might bring to a vortex clusterization. However, sometimes the out-of-plane stray field at the bifurcation can be high enough to nucleate more than a single vortex, but, as shown in fig.4.3e-f, MFM might not be capable to distinguish between vortex clusters or giant vortex due to limited lateral resolution. Such occurrences leave as an open question whether or not the magnetic/geometric confinement due to bifurcations and stripe endpoints, is able to induce giant vortices. STM/STS have been used to address the problem, by performing experiments on  $\text{Pb}(30\text{nm})/[\text{Co}(2\text{nm})/\text{Pd}(2\text{nm})]_{200\text{-bilayers}}$ . A particularly dense agglomeration of vortices at the endpoint of a stripe has been reported. Tunneling spectroscopy has been used to resolve three distinct flux quanta, ruling out, in this case, the possibility of a giant vortex. Vortices inside the cluster result spaced by a distance 1.4 times shorter than the minimum value possible for fully separated vortices in bulk superconductors, achievable at the second critical field  $H_{c2}$ , proving a very strong magnetic confinement. In addition to this, the presence of zero bias peaks in the conductance spectra confirms that the Pb film is in the clean limit.

# Bibliography

- [1] P. Fischery, T. Eimüllery, G. Schützz, P. Guttmannx, G. Schmahlx, K. Prueglk, and G. Bayreutherk, *J. Phys. D: Appl. Phys.* **31**, 649 (1998)
- [2] O. Pietzsch, A. Kubetzka, M. Bode, and R. Wiesendanger, *Science* **292**, 2053 (2001)
- [3] A. Wachowiak, J. Wiebe, M. Bode, O. Pietzsch, M. Morgenstern, and R. Wiesendanger, *Science* **298**, 577 (2002)
- [4] Y. Murakami, D. Shindo, K. Oikawa, R. Kainuma, and K. Ishida, *Appl. Phys. Lett.* **82**, 3695 (2003)
- [5] A. Vansteenkiste, K.W. Chou, M.Weigand, M. Curcic, V. Sackmann, H. Stoll, T. Tyliszczak, G.Woltersdorf, C. H. Back, G. Schütz and B. VanWaeyenberge, *Nature Physics* **5**, 332 (2009)
- [6] F. Kronast, J. Schlichting, F. Radu, S.K.Mishra, T. Noll, and H.A. Dürr, *Surf. Interface Anal.* **42**, 1532 (2010)
- [7] W. Jiang, Y. Fan, P. Upadhyaya, M. Lang, M. Wang, L.-T. Chang, K. L. Wong, J. Tang, M. Lewis, J. Zhao, L. He, X. Kou, C. Zeng, X. Z. Zhou, R. N. Schwartz, and K. L. Wang, *Phys. Rev. B* **87**, 014427 (2013)
- [8] A. Hierro-Rodriguez, M. Velez, R. Morales,N. Soriano, G. Rodr?guez-Rodr?guez, L. M. A´ lvarez-Prado, J. I. Mart?n, and J. M. Alameda, *Phys. Rev. B* **88**, 174411 (2013)
- [9] C. Blanco-Roldan, C. Quiros, A. Sorrentino, A. Hierro-Rodriguez, L.M. Alvarez-Prado, R. Valcarcel, M. Duch, N. Torras, J. Esteve, J.I. Martin, M. Velez, J.M. Alameda, E. Pereiro, and S. Ferrer, *Nat. Comm.* **6**, 8196 (2015)

- [10] A.P. Volodin, and M.V. Marchevsky, *Ultramiroscopy* **42**, 757 (1992)
- [11] A. Oral, S. J. Bending, R. G. Humphreys, and M. Henini, *J. Low Temp. Phys.* **105**, 1135 (1996)
- [12] A. Volodin, K. Temst, C. Van Haesendonck, and Y. Bruynseraede, *Appl. Phys. Lett.* **73**, 8 (1998)
- [13] P.E. Goa, H. Hauglin, M. Baziljevich, E. Il'yashenko, P.L. Gammel and T.H. Johansen, *Supercond. Sci. Technol.* **14**, 729 (2001)
- [14] M. Terao, Y. Tokunaga, M. Tokunaga, and T. Tamegai, *Physica C* **426**, 94 (2005)
- [15] O. M. Auslaender, L. Luan, E. W. J. Straver, J. E. Hoffman, N. C. Koshnick, E. Zeldov, D. A. Bonn, R. Liang, W. N. Hardy, and K. A. Moler, *Nature Physics* **5**, 35 (2009)
- [16] R. B. G. Kramer, A.V. Silhanek, W. Gillijns, and V.V. Moshchalkov, *Phys. Rev. X* **1**, 021004 (2011)
- [17] J. Auer and H. Ullmaier, *Phys. Rev. B* **7**, 136 (1973)
- [18] M.C. Leung, *J. Low Temp. Phys.* **12**, 1/2 (1973)
- [19] V. G. Kogan, N. Nakagawa, and S. L. Thiemann, *Phys. Rev. B* **42**, 4 (1990)
- [20] A.I. Buzdin, and A.Yu. Simonov, *JEPT Lett.* **51**, 3 (1990)
- [21] A.I. Buzdin, S.S. Krotov, and D.A. Kuptsov, *Physica C:Supercond.* **175**, 42 (1991)
- [22] A.I. Buzdin, and A. Simonov, *Physica C* **175**, 143 (1991)
- [23] S. J. Bending, and M. JW Dodgson, *J. Phys.: Condens. Matter* **17**, R955 (2005)
- [24] A.A. Bepalov, A.S. Mel'nikov, and A.I. Buzdin, *EPL* **110**, 37003 (2015)
- [25] K. Tanaka, I. Robel, and B. Janko, *PNAS* **99**, 8 (2002)
- [26] I. F. Lyuksyutov, and V. L. Pokrovsky, *Advances in Physics* **54**, 1 (2005)
- [27] L.-F. Zhang, L. Covaci, M. V. Milosevic, G. R. Berdiyrov, and F. M. Peeters, *Phys. Rev. B* **88**, 144501 (2013)

- [28] M. Z. Cieplak, Z. Adamus, M. Konczykowski, L. Y. Zhu, X. M. Cheng, and C. L. Chien, *Phys. Rev. B* **87**, 014519 (2013)
- [29] T. Cren, D. Fokin, F. Debontridder, V. Dubost, and D. Roditchev, *Phys. Rev. Lett.* **102**, 127005 (2009)
- [30] T. Shapoval, V. Metlushko, M. Wolf, V. Neu, B. Holzapfel, L. Schultz, *Physica C* **470**, 867 (2010)
- [31] T. Shapoval, V. Metlushko, M. Wolf, B. Holzapfel, V. Neu, and L. Schultz, *Phys. Rev. B* **81**, 092505 (2010)
- [32] M. Iavarone, A. Scarfato, F. Bobba, M. Longobardi, G. Karapetrov, V. Novosad, V. Yefremenko, F. Giubileo, and A. M. Cucolo, *Phys. Rev. B* **84**, 024506 (2011)
- [33] M. Iavarone, A. Scarfato, F. Bobba, M. Longobardi, S. A. Moore, G. Karapetrov, V. Yefremenko, V. Novosad, and A. M. Cucolo, *IEEE Trans. Magn.* **48**, 3275 (2012)
- [34] A. M. Cucolo, A. Scarfato, M. Iavarone, M. Longobardi, F. Bobba, G. Karapetrov, V. Novosad, and V. Yefremenko, *J. Supercond. Nov. Magn.* **25**, 2167 (2012)
- [35] F. Bobba, C. Di Giorgio, A. Scarfato, M. Longobardi, M. Iavarone, S. A. Moore, G. Karapetrov, V. Novosad, V. Yefremenko, and A. M. Cucolo, *Phys. Rev. B* **89**, 214502 (2014)
- [36] T. Cren, L. Serrier-Garcia, F. Debontridder, and D. Roditchev, *Phys. Rev. Lett.* **107**, 097202 (2011)
- [37] M. Iavarone, S.A. Moore, J. Fedor, S.T. Ciocys, G. Karapetrov, J. Pearson, V. Novosad, and S.D. Bader, *Nat. Comm.* **5**, 4766 (2014)
- [38] J. Brisbois, B. Raes, J. Van de Vondel, V. V. Moshchalkov, and A. V. Silhanek, *J. Appl. Phys.* **115**, 103906 (2014)
- [39] A.I. Gubin, K.S. Il'in, S.A. Vitusevich, M. Siegel, N. Klein, *Phys. Rev. B* **72**, 064503 (2005)
- [40] Y. Murayama, *J. Phys. Soc. Jap.* **21**, 2253 (1966)

- [41] S. Chikazumi, *Physics of Ferromagnetism*, Oxford University Press Inc., New York (1997) [57]D. Mancusi, C. Di Giorgio, F. Bobba, A. Scarfato, A. M. Cucolo, M. Iavarone, S. A. Moore, G. Karapetrov, V. Novosad, V. Yefremenko, S. Pace, and M. Polichetti, *Supercond. Sci. Technol.* **27**, 125002 (2014)
- [42] G.M. Genkin, V.V. Skuzovaktin, and I.D. Tokman, *J. Magn. Magn. Mater.* **130**, 51 (1993)
- [43] R. Laiho, E. Lähderanta, E.B. Sonin, and K.B. Traito, *Phys. Rev. B* **67**, 144522 (2003)
- [44] M. Ezawa, *Phys. Rev. B* **83**, 100408(R) (2011)
- [45] M. Tinkham, *Introduction to Superconductivity*, 2nd edition, McGraw-Hill, Inc. (1996)
- [46] H. F. Hess, R. B. Robinson, R. C. Dynes, J. M. Valles, Jr., and J. V. Waszczak, *Phys. Rev. Lett.* **62**, 214 (1989)
- [47] Joel D. Shore, Ming Huang, Alan T. Dorsey, and James P. Sethna, *Phys. Rev. Lett.* **62**, 26 (1989)
- [48] A. Kohen, T. Cren, Th. Proslir, Y. Noat, W. Sacks, D. Roditchev, F. Giubileo, F. Bobba, A. M. Cucolo, N. Zhigadlo, S. M. Kazakov, and J. Karpinski, *Appl. Phys. Lett.* **86**, 212503 (2005)

# Chapter 5

## Quantitative MFM

### 5.1 Introduction

The *quantitative* interpretation of MFM data is still a hot topic in the community of scanning probe microscopists. In fact, it may only be achieved in special cases through phenomenological pictures of the tip-sample interaction [1]. The rigorous difficulties of a *quantitative MFM* are mainly based on the fact that the tip magnetic properties are a priori not known. MFM image simulations or micromagnetic modeling, based on the so-called point-probe approximation [2] of the MFM tips, can help to understand the mechanism of the image formation [3]-[6], idealizing the tip magnetization distribution by a single magnetic monopole and using the frequency shift signal to determine the magnetic charge as well as its position within the real tip. Kebe *et al.* were able to demonstrate that, albeit its simplicity, the point-probe model supports a reliable tip calibration, allowing MFM quantitative measurements [7]-[9].

In the past, a number of experimental investigations were focused on hard disk transitions [10]-[12], current strips [13]-[16], current rings [17], [18] and magnetotactic bacteria [19] in order to characterize the MFM tips by using samples with well known magnetization and useful geometrical variations on the scale of interest. In this chapter, the magnetic tip characterization will be carried out from MFM measurements on superconducting vortices, always supporting the quantized magnetic flux  $\Phi_0 = \frac{hc}{2e}$ , where  $h$  is the Plank constant and  $e$  is the electron charge.

In the framework of the point-charge model, in [20] the authors derived the magne-

tostatic interaction between the MFM tip and a superconducting diamagnetic background, resulting in:

$$F_{z,tip-dia} = \frac{q^2}{4\pi\mu_0} \int_0^\infty F(x)e^{-2xz} x dx \quad (5.1)$$

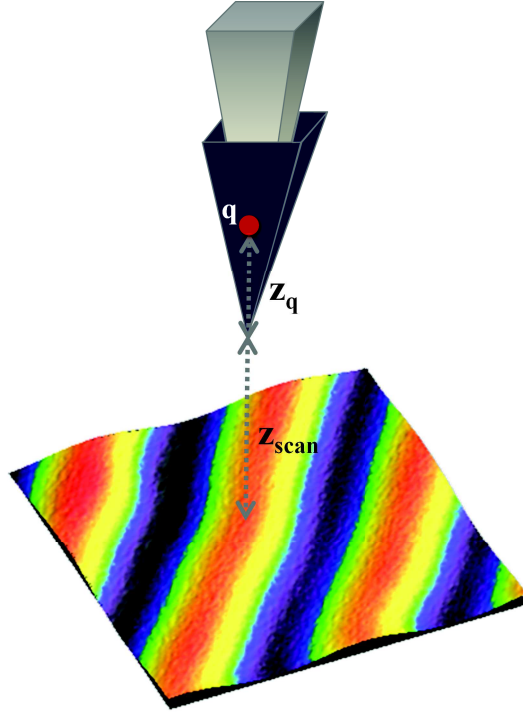


**Figure 5.1:** In the point-probe model the MFM tip is characterized by the magnetic charge  $q$  and its distance from the surface  $z = z_{scan} + z_q$ , where  $z_{scan}$  is the lift height used while scanning and  $z_q$  is the distance of the magnetic charge from the tip apex.

The tip properties  $q$  and  $z = z_{scan} + z_q$  are, respectively, the intensity of the magnetic charge and its distance from the sample surface (sum of the lift height of the measurement  $z_{scan}$  and the distance of the magnetic charge from the tip apex  $z_q$ ) (see fig.5.1). The function  $F(x) = \frac{\sqrt{\frac{1}{\lambda^2} + x^2} - x}{\sqrt{\frac{1}{\lambda^2} + x^2} + x}$ , contains the dependence from the London penetration depth  $\lambda$ .

On the other hand, in [21], the interaction between the magnetic tip and an Abrikosov vortex line  $\vec{\Phi}_0 = \Phi_0 \hat{z}$  was studied. In the case of a flux line surrounded by the vacuum,

i.e. in absence of a superconductor around the quantum flux, the tip-vortex force is:

$$F_{z,tip-vortex} = \frac{q}{2\mu_0} \int_0^\infty \Phi(x)e^{-xz} J_0(xr)xdx \quad (5.2)$$

here  $\Phi(x) = \frac{\Phi_0}{2\pi(1+(x\lambda)^2)}$  contains the dependence from the superconducting parameters, i.e.  $\lambda$  and the quantum flux  $\Phi_0$ ,  $J_0(xr)$  is the zero-order Bessel function and  $r$  is the lateral distance from the vortex core.

Instead, in bulk superconductors, a prefactor which takes into account the superconducting diamagnetism needs to be added to the expression 5.2. It has been calculated to be  $G(x) = \frac{2\sqrt{\frac{1}{\lambda^2}+x^2}}{x+\sqrt{\frac{1}{\lambda^2}+x^2}}$  [21]. The superconducting background introduces a magnetic offset (repulsive force) which shifts the zero of the tip-sample force to a finite, positive, value. Such a value makes the tip-vortex (tip-antivortex) force stronger (weaker), causing an unbalancing in the force profiles. The following expressions for tip-vortex (tip-antivortex) force:

$$F_{z,tip-vortex} = \frac{q}{\mu_0} \int_0^\infty G(x)\Phi(x)e^{-xz} J_0(xr)xdx \quad (5.3)$$

$$F_{z,tip-antivortex} = -\frac{q}{\mu_0} \int_0^\infty G(x)\Phi(x)e^{-xz} J_0(xr)xdx \quad (5.4)$$

have been plotted in fig. 5.2 (blue line), together with the force between the magnetic tip and a vortex (antivortex) surrounded by the vacuum (red line).

As expected, in presence of diamagnetism an asymmetry in tip-vortex/tip-antivortex force occurs as well as the force reaches a non-zero positive value in between V and AV. The plot has been carried out with a tip-vortex distance of  $10nm$  and by using a magnetic charge value  $q = 1.3^{-14}Wb$ , reported in literature [21].

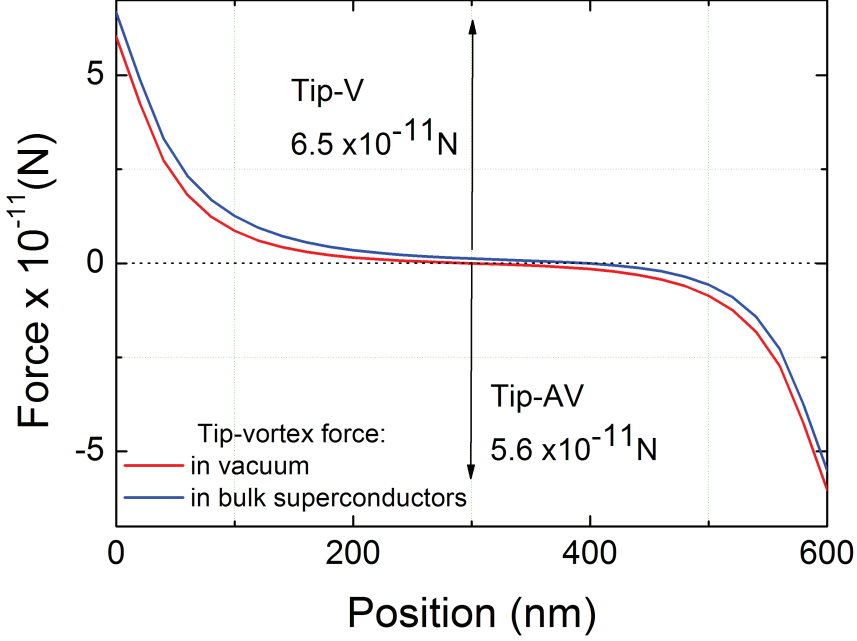


**Figure 5.2:** red line: force exerted by V and AV in vacuum on a magnetic tip. Blue line: force exerted by V and AV in a bulk superconductor on a magnetic tip. An unbalancing of  $0.9 \times 10^{-11} N$  between tip-vortex and tip-antivortex force is found, with respect to the diamagnetic background. Values of  $z = 10 nm$  and  $q = 1.30^{-14} Wb$  have been used.

In this chapter, the MFM experimental results on nucleation of V-AV pairs in 200nm-Nb single layer will be compared to the theoretical cantilever frequency shift  $df = \frac{f_0}{2k} \frac{dF_z}{dz} = \frac{f_0}{2k} \left( \frac{dF_{z,tip-antivortex}}{dz} + \frac{dF_{z,tip-vortex}}{dz} \right)$ , derived from the expressions 5.3 and 5.4. By fitting the experimental magnetic profiles, the parameters  $q$  and  $z_q$  of commercially available MFM tips (MESP-LM, from Bruker) will be extracted. Finally, as example of quantitative MFM, the results of the fitting procedure will be used to find quantitative information on the out-of-plane component of the magnetization of a Py ferromagnetic thin film, by performing an MFM experiment on Nb(360nm)/Py(1 $\mu$ m) heterostructure. The Py stray field, coming out from the surface, results in  $H_{Py} = 8M_0 \sum_{k=0}^{\infty} \frac{(2k+1)(\frac{\pi}{w}) \sin[(2k+1)(\frac{\pi}{w})x]}{(2k+1)^2(\frac{\pi}{w})} e^{-(2k+1)(\frac{\pi}{w})z}$  [22], where  $M_0$  is the small, alternating up-and-down, out-of-plane component of the Py canted magnetization and  $w$  is the width of the stripe-like magnetic domains. By measuring the frequency shift  $df =$

$\frac{f_0}{2k} q \left. \frac{dH_{Fy}}{dz} \right|_{z=z_{scan}+z_q}$  and the domain width  $w$  from the MFM maps, the local value of  $M_0$  will be quantified.

## 5.2 Tip Characterization

The coexistence of V-AV pairs in 200-nm Nb single layer was obtained by cooling down the sample, below  $T_s$ , with the magnetic probe, longitudinally magnetized, very close to the sample surface and in presence of an opposite magnetic field. In this way, a vortex nucleation just under the tip apex is expected due to the probe field, whereas the opposite external magnetic field ensures an homogeneous distribution of antivortices within the sample. Of course, the presence of intrinsic pinning center in Nb is required, in order to avoid the annihilation of the V-AV pair. The inset of fig. 5.3 shows an MFM maps acquired in presence of a V-AV pair in 200nm-Nb single layer, at  $T=6K$  and  $z_{scan} = 100nm$ . The flux lines were nucleated applying a magnetic field  $H = +2.70e$  and keeping a constant separation  $d_{tip-sample} \approx 10nm$  during the cooling process.

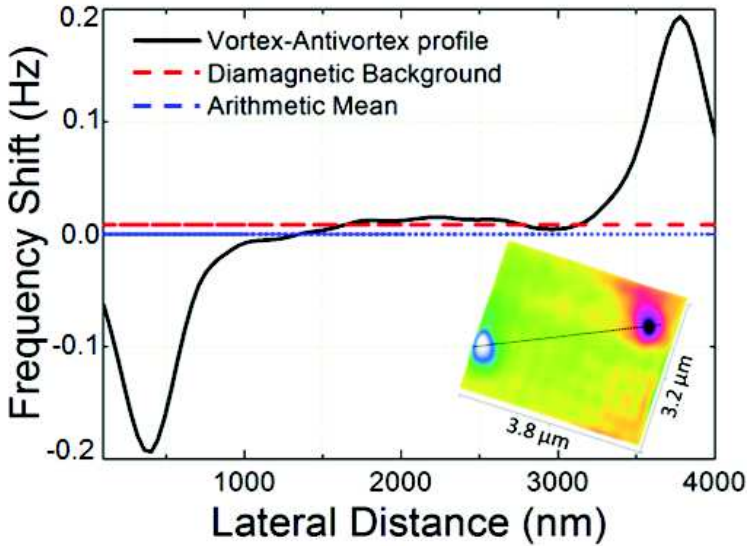


**Figure 5.3:** Main panel - magnetic profile of V-AV pair in 200nm-Nb single layer (black line); constant diamagnetic contribution (red line); mean value  $\frac{h_{vortex}+h_{antivortex}}{2}$  (blue line). Inset - MFM map of V-AV pair in 200nm-Nb single layer. The scan size is  $3.8\mu m \times 3.2\mu m$ ,  $T = 6K$  and  $z_{scan} = 100nm$

The profile of fig. 5.3 draws the magnetic outline of V and AV on the top of the Nb diamagnetic background. The diamagnetic constant contribution (red line in fig. 5.3) was found excluding the V-AV pairs from the MFM maps and measuring the magnetic signal coming out from the superconducting region. The blue line, corresponding to the mean value  $\frac{h_{vortex}+h_{antivortex}}{2}$ , allows to quantify the unbalancing of the V-AV heights, resulting in the difference between red and blue lines. With respect to our diamagnetic zero, the V results deeper than the AV.

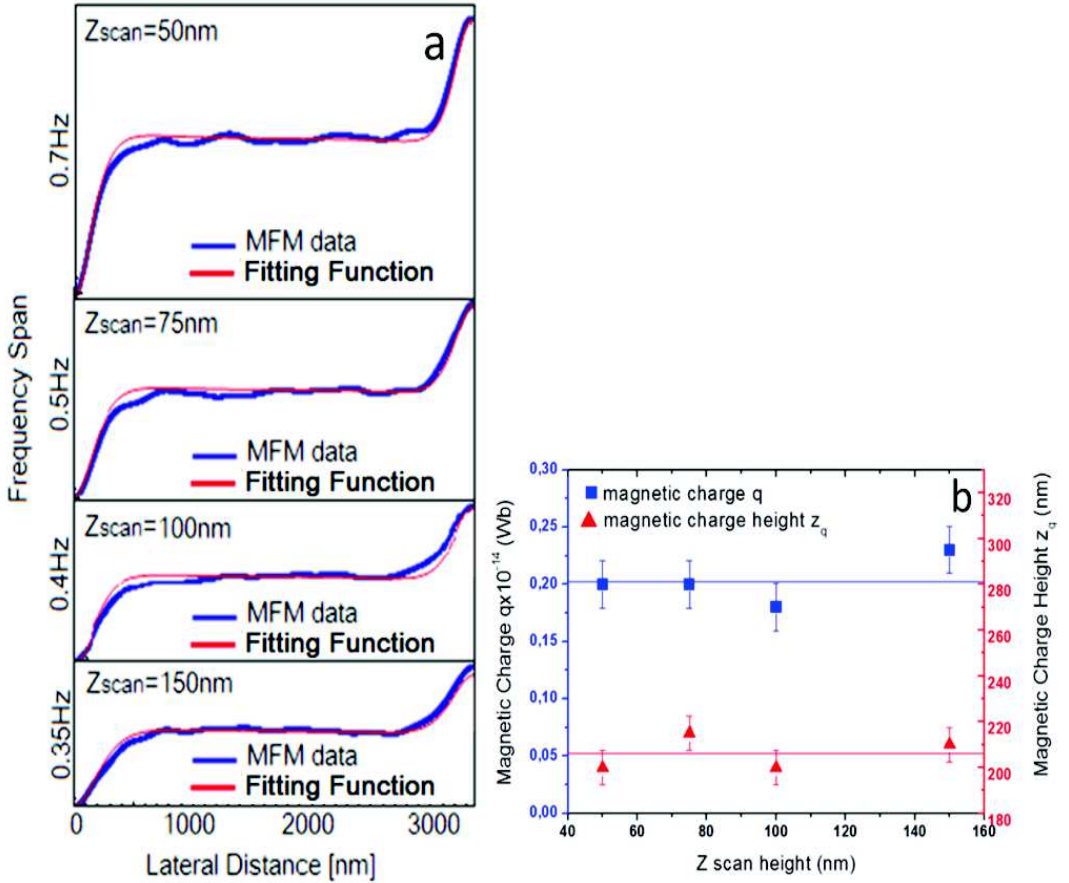


**Figure 5.4:** a) blue lines: MFM experimental V-AV profile at four different scan height:  $z_{scan} = 50\text{nm}$ ,  $75\text{nm}$ ,  $100\text{nm}$  and  $150\text{nm}$ . Red lines: fitting function  $df = \frac{f_0}{2k} \left( \frac{dF_{z,tip-antivortex}}{dz} + \frac{dF_{z,tip-vortex}}{dz} \right)$ . b) summary plot of  $q$  and  $z_q$  data, interpolated by a linear fit with zero slope.

The V-AV profiles at four different scan heights  $z_{scan} = 50\text{nm}$ ,  $75\text{nm}$ ,  $100\text{nm}$  and  $150\text{nm}$ , are presented in fig. 5.4a. As a consequence of the increase of  $z_{scan}$ , the fre-

quency span is reduced from  $0.7Hz$  to  $0.35Hz$ . In fig. 5.4a, the MFM data (blue lines) are fitted by the analytical expressions  $df = \frac{f_0}{2k} \left( \frac{dF_{z,tip-antivortex}}{dz} + \frac{dF_{z,tip-vortex}}{dz} \right)$  of the frequency shift (red lines), being  $q$  and  $z_q = z - z_{scan}$  the fitting parameters,  $\lambda(6K) = 68nm$  the penetration length at the measurement temperature  $T = 6K$ ,  $f_0 = 75kHz$  and  $k \approx 2.8 \frac{N}{m}$  the resonance frequency and the spring constant of the used cantilever. A very good matching between experimental data and fitting function is found when  $q$  and  $z_q$  take the values summarized in fig. 5.4b. The constant behavior of both magnetic charge  $q$  vs  $z_{scan}$  and magnetic charge height  $z_q$  vs  $z_{scan}$ , in the considered  $z_{scan}$  range, allows to characterize the used MESP-LM tip by deriving  $q = (0.20 \pm 0.01) \times 10^{-14}Wb$  and  $z_q = (206 \pm 4)nm$  from the linear fit of the data of fig. 5.4b.

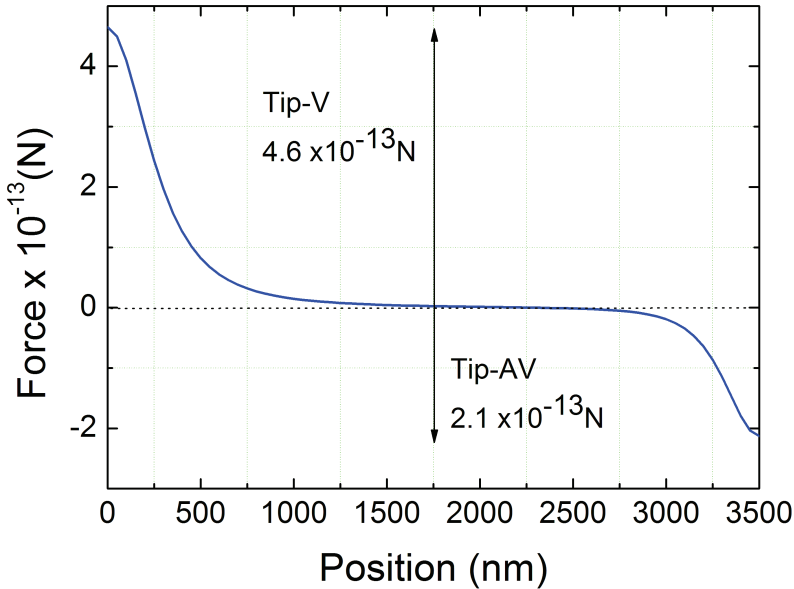


**Figure 5.5:** Force exerted on the MFM tip having  $q = 0.20 \times 10^{-14}Wb$  and  $z_q = 206nm$  by the V-AV pair in Nb-200nm single layer at  $z_{scan} = 50nm$

Figure 5.5 plots the force exerted on the used MFM tip by the V-AV pair in Nb-200nm single layer. At  $z_{scan} = 50nm$ , the unbalancing of the tip-vortex/tip-antivortex force results in  $2.5 \times 10^{-13}N$ .

### 5.3 Measure of $1\mu\text{m}$ Py out-of-plane magnetization

The tip calibration procedure, described in the previous section, has been successfully used in performing quantitative MFM experiment on Nb(360nm)/Py(1 $\mu\text{m}$ ).

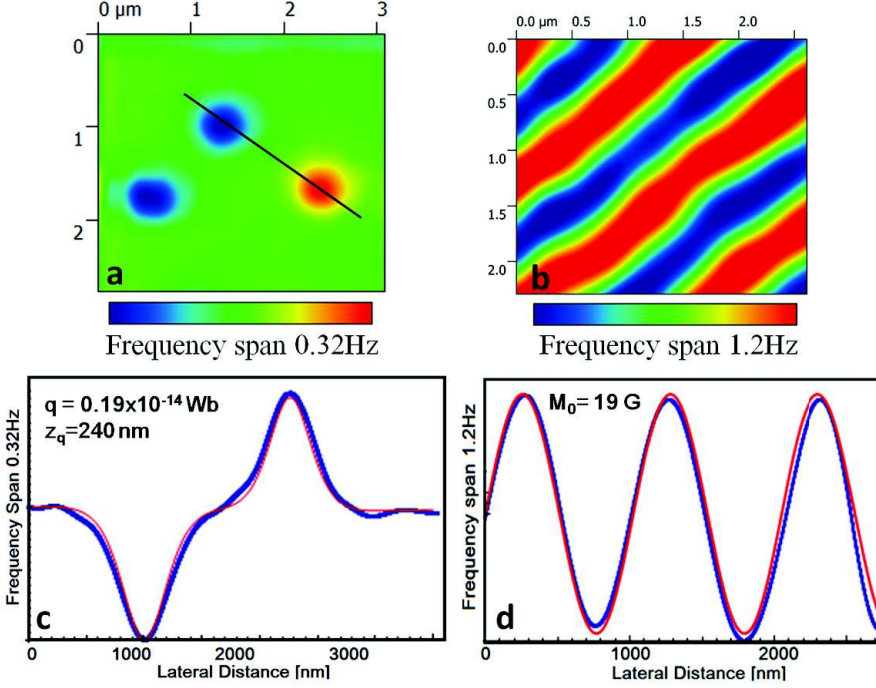


**Figure 5.6:** a)-b) MFM maps acquired at  $h = 110\text{nm}$  and  $T = 6\text{K}$  (a),  $T = 13\text{K}$  (b). c)-d) blue lines: MFM experimental profile. Red lines: fitting function

Fig. 5.6a-b show the MFM maps acquired with the same MESP-LM tip respectively below and above the Nb critical temperature. In fig. 5.6a, at  $T = 6\text{K}$  and  $z_{scan} = 110\text{nm}$ , a V-AV pair is clearly present on the top of the superconducting background, totally shielding the Py stray field. In fig. 5.6b, at  $T = 12\text{K}$  and  $z_{scan} = 60\text{nm}$ , the characteristic Py stripe-like magnetic domains, due to the alternating up-and-down, out-of-plane component  $M_0$  of the Py canted magnetization, are visible. As previously discussed, the V-AV pair profile (the blue line in fig. 5.6c) has been fitted by the function  $df = \frac{f_0}{2k} \left( \frac{dF_{z,tip-antivortex}}{dz} + \frac{dF_{z,tip-antivortex}}{dz} \right)$ . The best fit (red line in fig. 5.6c), resulting in  $q = 0.19 \times 10^{-14} \text{ Wb}$  and  $z_q = 240\text{nm}$ , shows again a very good agreement between experimental data and theoretical prediction. It is worth to notice that these values of  $q$  and  $z_q$  are very close to  $q = 0.2 \times 10^{-14} \text{ Wb}$  and  $z_q = 206\text{nm}$ , previously

found out for a different MESP-LM tip, giving high confidence in the robustness of the method. With a so characterized tip, the MFM profile of the Py stray field (blue line in fig. 5.6d) has been fitted by the function  $df = \frac{f_0}{2k} q \frac{dH_{Py}}{dz} \Big|_{z=z_{scan}^*+z_q}$ , paying attention to specify the right distance from the ferromagnetic film surface ( $z_{scan}^* = z_{scan} + z_{Nb}$ ). In this way we extracted the local value of  $M_0$ , resulting in  $M_0 = 19G$ , in agreement with previous prediction (see chapter 3) [23] and measurement [24], [25], [26].

## 5.4 Conclusions

In this chapter, a possible procedure to characterize an MFM tip has been presented as well as the result of a quantitative MFM experiment on Nb(360nm)/Py(1 $\mu$ m).

A commercially available MFM tip (MESP-LM, from Bruker) was used to perform cryogenic MFM experiments on 200-nm Nb single layer. The nucleation of a V-AV pair in the superconductor required to cool down the sample in external magnetic field, with the magnetic tip approached. In such a way, the superconductor experiences a strongly localized magnetic field due to the probe, which was previously magnetized along its longitudinal axis, simultaneously to an uniform external field, with opposite direction, applied by the magnet. The result is the nucleation of a vortex right under the tip apex, surrounded by an uniform distribution of antivortices inside the sample. However, the presence of intrinsic pinning site in Nb is necessary to avoid the annihilation of the flux pair.

By using the London equation for describing a superconductor in the mixed state, the force experienced by the magnetic tip due to a superconducting vortex can be easily derived whenever the tip is described as a point-charge  $q$ , located at  $z_q$  with respect to the tip apex (*point-probe approximation*) [21].

Once the expression of the force is known, the frequency shift of the resonating cantilever,  $df = \frac{f_0}{2k} \frac{dF_z}{dz}$ , can work as fitting function for the experimental measured magnetic profile, having  $q$  and  $z_q$  as fitting parameters.

However, the contribution of the diamagnetic background on the magnetic profile of V and AV has to be taken into account. Experimentally it results in having a vortex deeper than the paired antivortex. In fact, in between V and AV, the tip feels a repulsive interaction with the superconducting background, which causes a positive frequency shift. In such a way, an overestimation (underestimation) of vortex (antivortex) height occurs, with respect to the background (where the tip-sample force is

non-zero).

By fitting the V-AV profile at several  $z_{scan}$ ,  $q = (0.20 \pm 0.01) \times 10^{-14} Wb$  and  $z_q = (206 \pm 4) nm$  were found for the used tip and a tip-vortex force of the order of  $10^{-13} N$ , at  $z_{scan} = 50 nm$ , was estimated.

Once the fitting procedure was set up and known, a quantitative MFM experiment was performed on Nb(360nm)/Py(1 $\mu$ m). Again, the used MESP-LM tip was characterized on a V-AV pair nucleated in the S/F heterostructure. It is worth to notice that here the biggest source of *bulk* pinning comes from the stripe-like ferromagnetic structure underneath the superconductor, which is completely shielded at the sample surface due to the high Nb thickness, rather than from the intrinsic pinning in the superconducting layer. The results of the fitting procedure,  $q = 0.19 \times 10^{-14} Wb$  and  $z_q = 240 nm$ , are not so far from previous values of  $q$  and  $z_q$ , proving the robustness of the model. Moreover, once the tip is characterized, the MFM profile of Py stray field (above  $T_s$ ) was fitted by the function  $df = \frac{f_0}{2k} q \left. \frac{dH_{Py}}{dz} \right|_{z=z_{scan}^*+z_q}$ , where  $H_{Py} = 8M_0 \sum_{k=0}^{\infty} \frac{(2k+1)(\frac{\pi}{w}) \sin[(2k+1)(\frac{\pi}{w})x]}{(2k+1)^2(\frac{\pi}{w})} e^{-(2k+1)(\frac{\pi}{w})z}$ , keeping  $M_0$  as free parameter. By doing this, a local value of  $M_0 = 19G$  was found, which is in good agreement with previous predictions [23] and measurement [24], [25], [26].

# Bibliography

- [1] U. Hartmann, *Adv. Electron. Electron Phys.* **47**, 49 (1994)
- [2] U. Hartmann, *Phys. Lett. A* **137**, 475 (1989)
- [3] H.J. Hug, B. Stiefel, P.J.A. van Schendel, A. Moser, R. Hofer, S. Martin, H.-J. Gunterodt, S. Porthun, L. Abelmann, J.C. Lodder, G. Bochi, and R.C.O'Handley, *J. Appl. Phys.* **83**, 5609 (1998)
- [4] S.L. Tomlinson, and A.N. Farley, *J. Appl. Phys.* **81**, 5029 (1997)
- [5] S.L. Tomlinson, and E.W. Hill, *J. Magn. Magn. Mater.* **161**, 385 (1996)
- [6] A. Hubert, W. Rave, and S.L. Tomlinson, *Phys. Status Solidi B* **204**, 817 (1997)
- [7] Th. Kebe, and A. Carl, *J. Appl. Phys.* **95**, 775 (2004)
- [8] J. Lohau, S. Kirsch, A. Carl, G. Dumpich, and E.F. Wassermann, *J. Appl. Phys.* **86**, 3410 (1999)
- [9] A. Carl, and E.F. Wassermann, *Magnetic Nanostructures*, H.S. Nalwa, American Scientific Publisher (2002)
- [10] , R.B. Proksch, S. Foss, and E.D. Dahlberg, *IEEE Trans. Magn.* **30**, 4467 (1994)
- [11] D. Rugar, H.J. Mamin, P. Guethner, S.E. Lambert, J.E. Stern, I. Mc-Fadyen, and T. Yogi, *J. Appl. Phys.* **68**, 1169 (1990)
- [12] K. Babcock, M. Dugas, V. Elings, and S. Loper, *IEEE Trans. Magn.* **30**, 4503 (1994)
- [13] T. Goddenhenrich, H. Lemke, M. Muck, U. Hartmann, and C. Heiden, *Appl. Phys. Lett.* **57**, 2612 (1990)

- [14] K. Babcock, V.B. Elings, J. Shi, D.D. Awschalom, and M. Dugas, *Appl. Phys. Lett.* **69**, 705 (1996)
- [15] R. Yongsunthon, J. McCoy, and E.D. Williams, *J. Vac. Sci. technol. A* **19**, 1763 (2001)
- [16] C. Liu, K. Lin, R. Holmes, G.J. Mankey, H. Fujiwara, H. Jiang, and H.S. Cho, *J. Appl. Phys.* **91**, 8849 (2002)
- [17] L. Kong, and S.Y. Chou, *Appl. Phys. Lett.* **66**, 2582 (1995)
- [18] L. Kong, and S.Y. Chou, *Appl. Phys. Lett.* **81**, 5026 (1997)
- [19] R.B. Proksch, T.E. Schaffer, B.M. Moskowitz, E.D. Dahlberg, D.A. Bazylinski, and R.B. Frankel, *Appl. Phys. Lett.* **66**, 2582 (1995)
- [20] H.J. Hug, Th. Jung, H.-J. Gunterodt and H. Thomas, *Physica C* **175**, 357 (1991)
- [21] H.J. Reittu and R. Laiho, *Supercond. Sci. Technol.* **5**, 448 (1992)
- [22] R. Lahio, E. Lähderanta, E. B. Sonin, K.B. Traito, *Phys. Rev. B* **67**, 144522 (2003)
- [23] F. Bobba, C. Di Giorgio, A. Scarfato, M. Longobardi, M. Iavarone, S. A. Moore, G. Karapetrov, V. Novosad, V. Yefremenko, and A. M. Cucolo, *Phys. Rev. B* **89**, 214502 (2014)
- [24] M. Iavarone, A. Scarfato, F. Bobba, M. Longobardi, G. Karapetrov, V. Novosad, V. Yefremenko, F. Giubileo, and A. M. Cucolo, *Phys. Rev B* **84**, 024506 (2011)
- [25] A. Belkin, V. Novosad, M. Iavarone, J. Fedor, J.E. Pearson, A. Petrean-Troncilli, G. Karapetrov, *Appl. Phys. Lett.* **93**, 0725110 (2008)
- [26] A. Belkin, V. Novosad, M. Iavarone, R. Divan, J. Hiller, T. Proslie, J.E. Pearson, G. Karapetrov, *Appl. Phys. Lett.* **96**, 092513 (2010)

# Conclusions

A study of the vortex matter in magnetically coupled Superconductor/Ferromagnet heterostructures, made by Nb/Py and Pb/[CoPd]*multilayers*, was carried out by using low temperature Scanning Probe Microscopy techniques.

The investigation of vortex-antivortex nucleation in Nb/Py bilayers was performed by low temperature Magnetic Force Microscopy experiments on several samples with different superconducting and ferromagnetic thickness in order to tune the threshold conditions for spontaneous superconducting flux quantum nucleation. Such systems allowed the study of the vortex confinement due to the magnetic template as well as to the Bean-Livingston barrier. Even more effective than the stripe template itself for pinning superconducting vortices, the influence of defects of the magnetic structure, namely *bifurcations*, on vortex arrangement in Nb/Py as well as Pb/[CoPd]*multilayers*, was studied by combining Magnetic Force Microscopy and Scanning Tunneling Microscopy and Spectroscopy techniques. Finally, a new procedure for performing Quantitative Magnetic Force Microscopy experiments was developed and used to get a measure of the out-of-plane magnetization in  $1\mu\text{m}$ -Py.

Apart from the intriguing and exciting physics governing the vortex matter in S/F hybrids, which has been partially discussed in details in this dissertation and which will be matter of further investigation and experiments, the strong cooperation of two different, cryogenic and UHV, techniques has been one of the main point in reaching the scientific goal of this thesis. Being sensitive to magnetic and electronic properties respectively, Magnetic Force Microscopy and Scanning Tunneling Microscopy and Spectroscopy are definitely complementary in the investigation of S/F hybrids. However, the correct operation of these techniques as well as the success of the experiments requires a lot of efforts in preliminary maintaining a cryogenic system and avoiding any external contamination of the UHV parts, in preparing the surfaces of the samples

under investigation, in acquiring a lot of statistics, required to get general conclusions from the investigation of micrometric sized areas.

New experiments are planned for the next future, with the aim of improving our understanding of the physics of S/F hybrids. On one side we would like to perform additional in-field experiments on S/F hybrids only magnetically coupled, by means of Magnetic Force Microscopy, in order to get more insight into the rigidity of the spontaneous/field cooled vortex lattice. On the other hand, we started already the investigation of S/F heterostructures in exchange coupling, by means of Scanning Tunneling Microscopy and Spectroscopy. Even if not reported in this dissertation, in the last year several attempts have been made to follow up in this direction, starting from the in-situ deposition of the constituting materials to the electronic characterization of the superconducting DOS.

# Publications

F. Bobba, **C. Di Giorgio**, A. Scarfato, M. Longobardi, M. Iavarone, S. A. Moore, G. Karapetrov, V. Novosad, V. Yefremenko, and A. M. Cucolo, *Vortex-Antivortex co-existence in Nb based Superconductor/Ferromagnet heterostructures*, *Phys. Rev. B* **89**, 214505 (2014)

D. Mancusi, **C. Di Giorgio**, F. Bobba, A. Scarfato, A. M. Cucolo, M. Iavarone, S. A. Moore, G. Karapetrov, V. Novosad, V. Yefremenko, S. Pace, and M Polichetti, *Magnetic pinning in a superconducting film by a ferromagnetic layer with stripe domains*, *Supercond. Sci. Technol.* **27**, 125002 (2014)

S. A. Moore, J. L. Curtis, **C. Di Giorgio**, E. Lechner, M. Abdel-Hafiez, O. S. Volkova, A. N. Vasiliev, D. A. Chareev, G. Karapetrov, and M. Iavarone, *Evolution of the superconducting properties in  $FeSe_{1-x}S_x$* , *Phys. Rev. B* **92**, 235113 (2015)

A. Di Trollo, P. Alippi, E.M. Bauer, G. Ciatto, M.H. Chu, G. Varvaro, A. Polimeni, M. Capizzi, M. Valentini, F. Bobba, **C. Di Giorgio**, A. Amore Bonapasta, *Ferromagnetism and conductivity in hydrogen irradiated Co-doped ZnO thin films*, submitted to *APS Appl. Mater.*

**C. Di Giorgio**, F. Bobba, A. Scarfato, D. D'Agostino, A.M. Cucolo, G. Karapetrov, S. A. Moore, V. Novosad, V. Yefremenko, and M. Iavarone, *Observation of superconducting vortex clusters in S/F hybrids*, in preparation

J.L. Curtis, **C. Di Giorgio**, M. Iavarone, *et al.*, *Vortex lattice transition in FeSe single crystals*, in preparation

**C. Di Giorgio**, M. Iavarone, *et al.*, *Tunneling spectroscopy at the twin boundary: implication on the symmetry of the order parameter*, in preparation

# Acknowledgments

First and foremost I feel grateful to my advisor Professor Fabrizio Bobba.

I thank Professor Bobba for involving me in all the activities of the SPnM laboratory, which captured my attention almost five years ago, for teaching me the love and respect for the laboratory itself, for having always the right answer and explanation to my questions and my doubts, for teaching me not only Physics, but also the curiosity and the passion for the world around me.

I thank Fabrizio for respecting my space and my time, for being pushy when I needed somebody to push me, for being supportive when I needed a support and for being patient every time I was unpleasant. I thank him for being always present, even when thousands of km far, for helping me when necessary, and for opening my mind with a few of his words.

I would like to express my gratitude to Professor Anna Maria Cucolo, for keeping always open the doors of the SPnM lab and bringing me to join it, for constantly believing in me and for encouraging me and all her students to always give our best. I'm grateful for her continual support and precious advices as well as for the stimulating discussion about physics and anything else.

I feel extremely grateful to Professor Maria Iavarone. She allowed me to join her group in USA for 14 months and, in doing this, she offered me the biggest experience of science and life I could ever imagine. Not only I learned how things work outside of Salerno, outside of Italy and outside of Europe, but I also learned a lot about myself. I thank her for being confident in my capabilities, for letting me operate her STM and for opening my eyes and my mind. The passion and the care she puts in her job, as experimentalist for physics and as teacher for the students, is extremely exemplary and remarkable.

I thank all the people I met along my way in the past few years and all the people

that are part of my life since a very long time. I thank Nunzia that grew up with me, for being always a strong reference point in my life, for always supporting me with her point of view, the most of the time different from mine, for all the fight we had to overcome together, for letting me feel Luca as a younger brother! I thank Chiara and Cristina for sharing with me this long path in physics, for being the most important part of all the fun and craziness necessary for me to get to this point, for being always on my side, for being protective when bad experiences occurred. I thank Ivana and Mara, for the fun time we shared in the lab. We lived together the experience of getting the Master Science Degree and this established the basis for a strong and beautiful friendship. I'm grateful to Matilde for all the time we spent together in the lab, for all the fun she made of me and of my aversion to "her bacteria", for all the support she gave me especially in the last few months. I thank Domenico for being a perfect friend to work with, careful, patient and supportive. His presence in our lab made it easier and enjoyable to be around. A special thank goes to Nicola, who always respected my freedom and supported my choices, helping me in all the difficulties I encountered in the past few years and never leaving me alone.

I cannot forget to thank my american friends for all the patience, support and fun. I thank Dan for having always two questions and often forgetting the second one; Steve, for the crazy nights in Maxie's and Dirty Frank's and Cassie for falling asleep at the bar; Eric for all the candies he shared with me; Aleksey for teaching us the russian way of doing things; James for his optimistic and nice attitude. I feel extremely lucky for meeting all these guys, because their help and friendship during my time in USA were unbelievable.

I cannot neglect that all of this would never be possible without the constant support and love of all my family. They had to accept many choices I made, sometime source of profound concern. However, they always respected my decisions believing those were the best for myself and my future. Their confidence in me pushed me to give my best! Finally, I would like to express my sincere gratitude to Prof. M. Iavarone and Prof. G. Karapetrov for proposing the research project, to Dr. V. Novosad, Dr. V. Yefremenko and Dr. S.A. Moore for fabricating the samples, and to all the coauthors of my papers for their contribution, suggestions and useful discussions. I acknowledge the support of the U.S. Department of Energy, Office of Basic Energy Sciences, Division of Materials Sciences and Engineering under Award DE-SC0004556 for the work carried out in *Temple University* and the support of the MIUR (Italian Ministry for Higher Education

and Research) under the project "Rientro dei cervelli", for the work performed in *Università degli Studi di Salerno*.

